Thin-Film Silicon Photovoltaics: Characterization of Thin-Film Deposition and Analysis of Enhanced Light Trapping from Scattering Nanoparticle Arrays

Thesis by
Krista S. Langeland

In Partial Fulfillment of the Requirements
for the Degree of
Doctor of Philosophy

1891

California Institute of Technology
Pasadena, California
2012

(Defended February 9, 2012)

0.1 Acknowledgments

The past several years have brought unexpected challenges accompanied by wonderful surprises, none more wonderful than discovering an outstanding group of generous people offering their support in innumerable capacities. First and foremost, I am extrememly grateful to my husband, Kirstin Bement, who tolerated my graduate school experience with an unconscionable level of patience, provided constant encouragement and insight, and washed more than his fair share of dishes. All of these pages are dedicated to you.

I have had the great fortune of working in a research group that represents a wide variety of background and interests, and the insight gained from discussions and collaborations within the Atwater Group has been an invaluable resource in propelling my thesis research forward. For this reason I owe a large debt of gratitude to the entire group for their inquisitive spirit and consistent willingness to offer assistance, and in particular to Harry Atwater for providing this opportunity, for offering encouragement, advice, and ideas, and for allowing me to follow a non-linear path through my thesis studies. I would like to thank my candidacy committee: Sossina Haile, Bill Johnson, and Brent Fultz, as well as my thesis defense commitee: Sossina Haile, Julia Greer, and Austin Minnich, for their comments and insight as I conclude my studies. I came to Caltech with very little practical lab experience, and I am grateful beyond words to Brendan Kayes, Morgan Putnam, Michael Kelzenberg, and Michael Filler for their aid and manual labor in trouble-shooting and repairing equipment. I inherited the thin-film silicon study from Christine Esber-Richardson, and her orientation to the project and willingness to guide me through the initial stages was critical and very much appreciated. As my thesis project morphed from materials characterization to optics, Vivian Ferry not only led me through her pioneering research in this area, but also assisted in coordinating sample fabrication with Philips Research, provided simulation code and trouble-shooting insights, and regularly offered invaluable guidance and support. Discussions with Luke Sweatlock, Jennifer Dionne, Jonathan Grandidier, Dennis Callahan, Emily Kosten, and Ragip Pala have not only helped to guide the direction of this research but have also provided a unique perspective on the vast potential for optical devices. Imogen Pryce and I struggled together with a very tedious template fabrication process that brought me to appreciate her amazing problem-solving prowess, and many subsequent discussions on device physics, fabrication, and putting together presentations have been indispensable. This thesis research has explored many possible device structures, and I will forever be amazed by and grateful to Brendan Kayes for providing intelligent insight into device design. Morgan Putnam has been a constant source of information and encouragement throughout my time at Caltech, and I have benefited greatly from his assistance with diffusion doping, equipment operation, and everything in between. Successful device measurements would not have been possible without the help of Michael Kelzenberg, who not only designed and built the equipment used for these measurements, but somehow also had the time and patience to guide me through the details of their operation. Raman spectroscopy is used widely for silicon film characterization in this study, and I thank Liz Muira for her willingness to conduct these measurements. I am also extremely grateful for the TEM training and assistance with image analysis provided by Channing Ahn and Carol Garland, and to Melissa Archer for her aid in sample preparation. In addition, I am thankful for the aid of Michael Deceglie in coordinating the installation of the PECVD chamber and for his skill and insight in reorganizing gas lines and power supplies. I am also indebted to Ryan Briggs and Koray Aydin for their generous assistance with e-beam lithography. I have had the great fortune of interacting with researchers across the globe at numberous conferences, and I would like to especially thank Hideki Matsumura for taking the time to lead me on a tour through his lab and the surrounding town when visiting Japan, and Harv Mahan for much valuable correspondence and shared ideas on materials characterization. The occupants of 248 Watson, both past and present, have been an amazing source of information and insight and have consistently made our office the most ecclectic place on campus, and I am privileged to have shared space and ideas with Jen Dionne, Brendan Kayes, Gerald Miller, Emily Warmann, Dan Turner-Evans, Carissa Eisler, and Ana Brown. The Atwater Group is a large and complex structure, and I am also grateful to Tiffany Kimoto and Jennifer Blankenship for having all the answers and for accommodating all of our odd requests and schedules with finesse. I would also like to acknowledge their predecessor, April Neidholdt, who has always been ready with a laugh and a snarky word; during her years as an administrative assistant for the Atwater Group she managed to keep everything running smoothly without letting us take ourselves too seriously, and her patience and friendship is truly appreciated. And of course this research has been possible only with generous funding sources, and I would like to also acknowledge BP Solar and the U.S. Department of Energy for their financial support of this research, as well as the Kavli Nanoscience Institute research facilities and staff for enabling a large portion of the fabrication conducted in this thesis.

My appreciation for the support structure provided by my outstanding friends and family cannot be overstated. My mom and dad have followed my schizophrenic academic career with what I can only assume is bemused bewilderment, but their support has been steadfast. They have offered their inspiration, comfort, and confidence from many miles away, yet they have been a close and integral part of my decision to follow through with graduate school. Mohrghaine Gaia and Gary Gable have enriched my life immensely with their curiosity and appreciation of all things new and fantastic, and I am particularly grateful for their deeply inspiring words, their unique and wonderful perspective, and for teaching me how to shuck oysters. I have made it to this point due in large part to the encouragement and advice of friends; in particular, Brendan Kayes has always been ready with an honest opinion and an appropriate playlist. Vivian Ferry and Imogen Pryce have been amazing sources of advice and encouragement, but I am additionally and wholeheartedly grateful for having the opportunity to explore new restaurants and wine lists with them. I got to know Ken Diest and Glenn Garrett under the inauspicious circumstances of quantum mechanics problem sets, but they have since been some of my favorite wine-tasting companions and culinary cohorts. I am grateful to Morgan Putnam for his optimism, encouragement, and friendship over all these years and for bringing the turkey on thanksgiving. I am thankful also to Rachel Watson; together we have enjoyed beach skates, margaritas, baking cookies, and a Vegas wedding, and her companionship and and advice have been extremely valuable. I have also enjoyed the camaraderie and support of the greatest roller derby team of all time, and I would like to thank the Sirens for providing uniquely ridiculous challenges, immeasurable fun, and innumerable bruises. Lastly, I would like to express gratitude to Tom Waits for always providing the appropriate song for the occasion.

0.2 Related Publications and Presentations

Enhanced Light Absorption in Thin-film Silicon with Subwavelength Surface Texturization. **Krista Langeland**, Vivian E. Ferry, Koray Aydin and Harry A. Atwater; Materials Reseach Society Symposium A: Amorphous and Polycrystalline Thin-Film Silicon Science and Technology; San Francisco, CA; 2011.

Measurement and Simulation of AAO Templated Nanoparticle Arrays on Silicon Thin Films. **Krista Langeland**, Imogen Pryce, Vivian Ferry, and Harry A. Atwater; Gordon Research Conference on Plasmonics; Waterville, ME; 2010.

Enhanced Photoconductivity from Plasmonic Nanoparticle Arrays on Thin Film Photovoltaic Silicon Absorber Layers. **Krista Langeland**, Imogen Pryce, Vivian Ferry and Harry A. Atwater; Materials Reseach Society Symposium T: Photovoltaics and Optoelectronics from Nanoparticles; San Francisco, CA; 2010.

Electronic properties of low temperature epitaxial silicon thin film photovoltaic devices grown by HWCVD. Christine E. Richardson, **Krista Langeland**, and Harry A. Atwater; Thin Solid Films, Vol. 516; 2008.

Microstructure and Passivation Effects on Open Circuit Voltage in Low Temperature Deposited Silicon Thin Films. **Krista Langeland**, Christine E. Richardson, Maribeth S. Mason, and Harry A. Atwater; Proceedings of the 4^{th} Internation Conference on HWCVD Process; Takayama, Japan; 2006.

0.3 Abstract

Thin-film solar cells have the potential to significantly decrease the cost of a finished device by cutting materials cost, and the characteristics of carrier transport through a thin film can concurrently increase the device performance over that of a wafer-based cell while tolerating a higher defect density in the absorbing material. However, while silicon is an attractive material for use in solar cells due to its nearly ideal band gap for single-junction cells and its relative abundance, its inefficient absorption of infrared light necessitates the development of light-trapping techniques to avoid losses in current generation. This thesis research has focused on two important goals: the development of a scalable thin-film silicon deposition method that produces high-quality material at minimal cost, and the evaluation of light-trapping mechanisms that will increase photon absorption in these films. Hot-wire chemical vapor deposition is used to fabricate silicon thin films with high crystalline fractions even on inexpensive substrates, and films grown with appropriate growth conditions exhibit initial open-circuit voltages above 450 mV, and while challenges in passivation still exist, this research illustrates the potential of this highly scalable and inexpensive deposition technique. Silver and silicon subwavelength structures were then both fabricated and simulated on ultra-thin silicon films on SiO_2 to evaluate their potential for increasing light absorption through plasmonic and physical scattering mechanisms, and spectral response measurements demonstrate over a ten-fold increase in carrier generation with a metal nanoparticle surface array. Periodic dielectric structures exhibit Bloch modes in both measurement and simulation, with an increase in overall quantum efficiency of over 11% from both a flat silicon layer and one that is randomly textured. These results highlight the significant role of scattering particle distribution in determining the light trapping characteristics in these devices. Design guidelines have been explored for exploiting resonant modes in these structures, and this thesis demonstrates the potential for both metal and dielectric

surface arrays to dramatically increase light absorption in silicon thin films.

Contents

List of Figures

Chapter 1

Thin-Film Silicon Solar Cells: Background and Device Challenges

1.1 The case for solar cell technology

As a growing world population and expanding modernization efforts place increasingly larger demands on energy supplies, the need for reliable sources of energy becomes ever more apparent. The decline of fossil fuel availability and the detrimental effect of its usage on the environment requires a clean and sustainable method of accommodating this need. Rapidly increasing global consumption of fossil fuel is accompanied by rising levels of atmospheric carbon dioxide; between 2004 and 2008, a population increase of 5% was accompanied by a 10% increase in energy production and a concurrent 10% increase in CO_2 emissions [1]. The total worldwide electricity demand has increased in the past ten years from 15,400 terawatt-hours in 2000 to over 21,330 terawatt-hours in 2010, a rise of almost 40% and a clear indication of the substantial need for a sustainable means of meeting this rapidly increasing demand [44].

While the U.S. Energy Information Administration reports that renewable energy resources accounted for only 7% of total energy production in 2008 (Figure 1.1), the increasing demand for clean and sustainable sources of energy has propelled the recent growth of solar manufacturing capacity from less than 2 GW in 2006 to over 12 GW annual production in 2010 (Figure 1.2 [72]). The past decade alone has seen a 40% increase in photovoltaic installed capacity [51]. This growth is projected to continue over the next 25 years and beyond; in the United States alone, solar power installations are expected to increase from 0.9 GW in 2010 to an expected total of

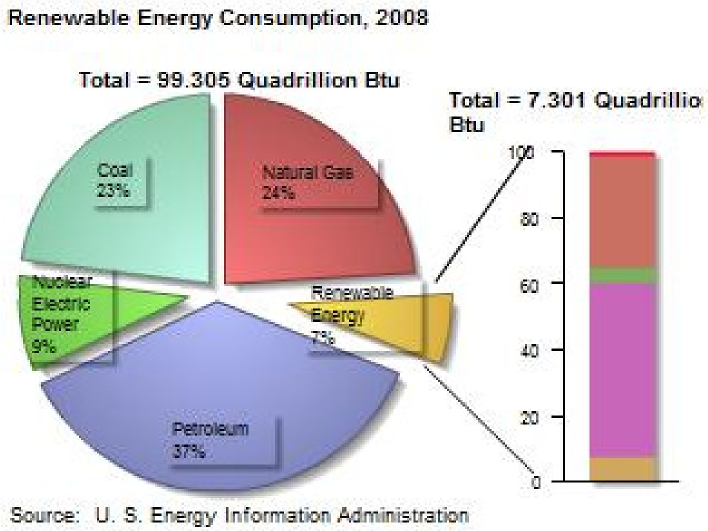

Source: U. S. Energy Information Administration

Figure 1.1. Distribution of energy consumption in United States in 2008 showing the total from renewable sources at 7% [72].

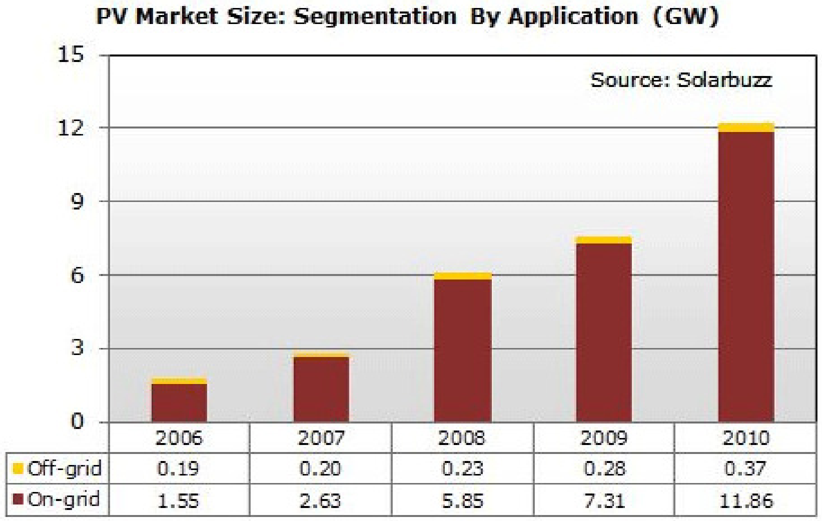

	2006	2007	2008	2009	2010
🟨 Off-grid	0.19	0.20	0.23	0.28	0.37
🟥 On-grid	1.55	2.63	5.85	7.31	11.86

Figure 1.2. Growth of PV market in installed GW from 2006 to 2010 [51].

2.4 GW in 2011, with an additional growth of 30% anticipated for 2012 (Figure 1.3) [52]. This growth is supported by incentives, subsidies, and increasing consumer awareness, fueled further by the decreasing cost of energy harvesting components and their installation due to advances in solar technology and manufacturing economies of scale. Increases in leading markets have been fueled by feed-in tariff programs

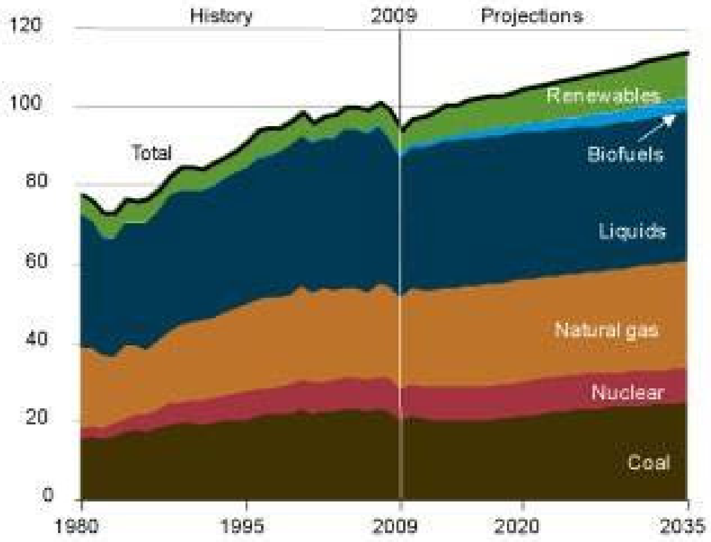

Figure 1.3. Primary energy resource distribution by fuel, as projected through 2035 [52].

that assign a higher value to solar-generated electricity than conventional sources, and an increase in component production results in a significant decrease in cost [83]. Historically, a cost reduction of approximately 22% can be expected for each doubling of installed capacity [51]. Even as subsidies are currently being reduced in leading solar markets like Germany, Italy, and France, the price of installation was predicted to decline close to 10% in 2011 [52]. This decline is accompanied by the climbing cost of conventionally generated electricity attributed to resource scarcity and growing demand; the price of electricity has consistently increased over the past decade, with prices in the European Union experiencing cost increases exceeding 15% from 2005 to 2007 [78].

The expansion of clean energy technology to a prominent position in the global market depends heavily on its cost-competitiveness. New solar technology must at least meet the current cost of grid-provided electricity, and current estimates anticipate this intersection will occur over the next 2-3 years for many industrialized economies [78]. However, further cost reductions will accelerate the adoption of photovoltaic technology and compensate for concurrent reductions in federal and state subsidies. The cost of a solar module represents 50% to 60% of the total installed cost of the system, and thus offers a key target for potential cost reduction. The materials used in cell fabrication account for a significant portion of the total module cost, with the polysilicon used to make wafer-based silicon solar cells accounting for about 40% of the total cell cost [8]. Several factors, however, play a role in determining the economic viability of photovoltaic technology, including materials costs, economies of scale, and device efficiency. A technology that seeks to decrease materials costs using scalable fabrication methods will succeed only if these developments are concurrent with satisfactory device efficiencies. For this reason this thesis research has focused on methods to reduce the cost of device production while maintaining or increasing efficiency of energy capture.

1.2 Solar cell physics

Electromagnetic radiation from the sun covers the spectral range from 0.2 μm to 3 μm and reaches the Earth with an intensity of $\tilde{1}000$ W/m^2, dependent upon the angle of incidence and atmospheric scattering. The conversion of this electromagnetic radiation into electricity takes place in a solar cell device and is referred to as the photovoltaic effect. The basic operation of a solar cell uses the energy of the absorbed light to generate electrons and holes, which are separated at a p-n junction. These charge carriers then diffuse to be collected at the contacts, thus generating electrical current. A p-n junction is formed by doping a semiconductor with impurities that create an excess of positive charge carriers on one side (p-type) and an excess of negative charge carriers on the other (n-type). At the interface between these two regions, the excess charge carriers will equilibrate by conducting electrons from the n-type region to the p-type region until a sufficient charge across the junction is produced to reach a steady-state with a built-in potential across the junction.

Current is generated from a solar cell by exciting electrons from the valence band of a semiconductor to the conduction band. This is accomplished through the absorption of incoming photons with energy greater than that of the band gap of the semiconductor (Figure 1.4). This process creates an electron-hole pair that is sepa-

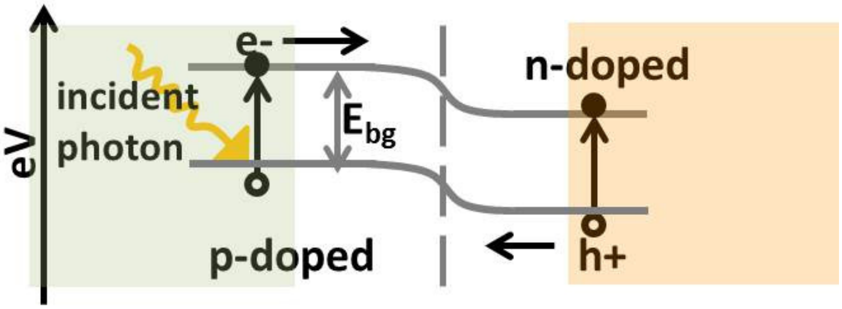

Figure 1.4. Energy band diagram at a pn junction.

rated by the built-in electric field generated by the p-n junction and generates current as these carriers are collected by the device contacts. Figure 1.5 demonstrates the basic operation of a solar cell via an idealized equivalent circuit. Represented here

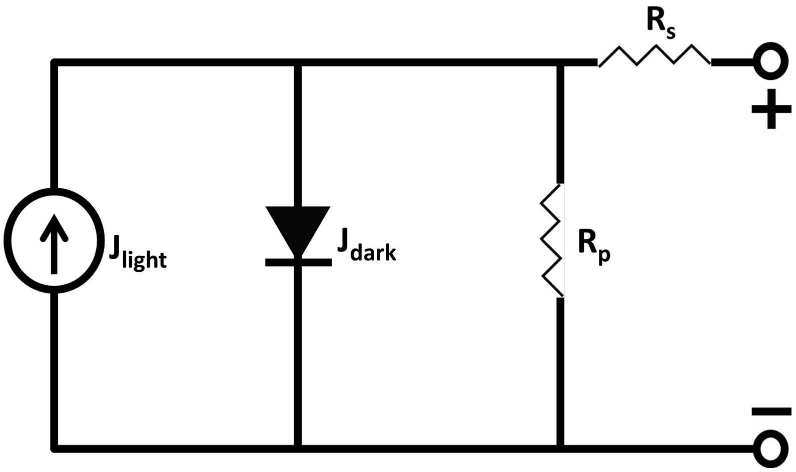

Figure 1.5. Solar cell equivalent circuit.

is an ideal diode in parallel with the current generated by the conversion of incident photons to charge carriers. Here J$_{dark}$ is the current density produced by the p-n junction as carriers diffuse across the depletion region; this is referred to as the reverse saturation current. J$_{light}$ is the photo-generated current density from carriers generated in the semiconductor and collected at the contacts of the device. R$_s$ is the series resistance inherent in a realistic solar cell device, and R$_p$ is the parallel resistance caused by shunting between contact terminals. Figure 1.6 plots the relationship between current density and voltage in the dark and under illumination for an ideal diode. The overall current-voltage relationship of the device can then be approximated as a superposition of the performance in both the dark and under illumination, J(V)=J$_{sc}$-J$_{dark}$. The total dark current of the solar cell is determined by:

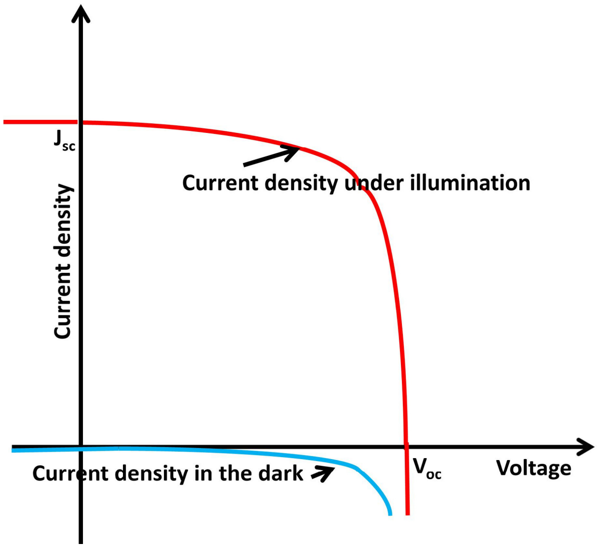

Figure 1.6. IV curve for ideal diode in the dark and under illumination.

$$J_{dark}(V) = J_0(e^{\frac{qV}{k_BT}} - 1) \tag{1.1}$$

J$_0$ is the dark saturation current and V is the built-in voltage across the p-n junction. The dark current is a reverse current that opposes and therefore reduces the generated photocurrent, and a large dark current is indicative of a high rate of carrier recombination in the device. The net current density generated by a solar cell is then represented by the idealized diode equation:

$$J(V) = J_{sc} - J_0(e^{\frac{qV}{k_B T}} - 1) \tag{1.2}$$

J$_{sc}$ is the photocurrent generated in a short-circuited device and is an important parameter in determining solar cell performance. This J$_{sc}$ is determined by the both the incident photon flux and the quantum efficiency (QE) of the device; the QE of a solar cell is the probability that an incident photon will generate a carrier that is subsequently collected at the device contacts, and this measure depends both on the absorption coefficient of the cell material and the collection efficiency of generated carriers. The relationship between J$_{sc}$ and these factors is given by:

$$J_{sc} = \int \Phi_s(E) QE(E) dE \tag{1.3}$$

Here Θ_s(E) is the incident spectral photon flux density and the limits of the integral are dictated by the applicable range of the incident spectrum. The J$_{sc}$ of a solar cell is therefore an indication of carrier recombination and absorption efficiency and is an important parameter in determining the performance of a solar cell device. Another significant indicator of device performance is the open-circuit voltage (V$_{oc}$) that occurs at J(V)=0, where J$_{dark}$ = J$_{sc}$, resulting in the following equation:

$$V_{oc} = \frac{k_B T}{q} ln(\frac{J_{sc}}{J_0} + 1) \tag{1.4}$$

The V$_{oc}$ increases logarithmically with light intensity while decreasing with dark saturation current (J$_0$). The J$_{sc}$ and V$_{oc}$ indicate the maximum possible current and voltage output, respectively, from the solar cell device. The net efficiency of a solar cell device is maximized when the power output density P=JV is maximized; the maximum power point is used to determine the fill factor of the solar cell. The fill factor (FF) of a solar cell is defined as the ratio of the maximum power output to the product of V$_{oc}$ and J$_{sc}$:

$$FF = \frac{J_{max} V_{max}}{J_{sc} V_{oc}} \tag{1.5}$$

This represented graphically by the squareness of the I-V curve in Figure 1.7, where

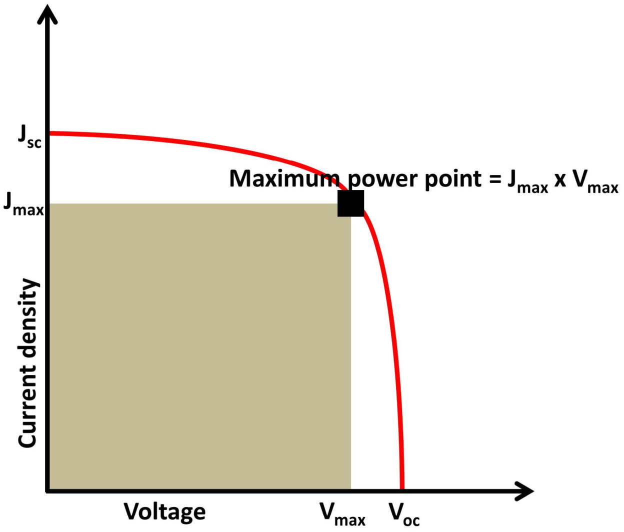

Figure 1.7. IV curve for illuminated solar cell device showing maximum power generation and fill factor.

the shaded area of this plot represents the maximum power output of the device. Mathematically, the efficiency of a solar cell device is related to the fill factor by:

$$\eta = \frac{J_{sc}V_{oc}FF}{P_s}, \tag{1.6}$$

where P_s is the spectral power density of the incident light. From these equations we can identify several factors that affect the resulting efficiency of solar devices. The dark saturation current, dictated by recombination of charge carriers before they can be collected, decreases the V_{oc}, and consequently the device efficiency. The equation for V_{oc} also indicates that this factor is proportional to the J_{sc}, determined by the number of generated carriers, which in turn is determined by the quantity of light absorbed. Both of these efficiency determinants are represented in the equation for V_{oc}, and for this reason this measurement is often used as the primary figure of merit when determining the potential performance of solar cell devices. This direct relationship between device efficiency and V_{oc} identifies carrier recombination and short-circuit current density as two significant parameters dictating overall solar cell device performance. To maximize cell efficiency, a device design that minimizes bulk and surface recombination while simultaneously maximizing the amount of incident light absorbed is required.

1.3 Overview of thin-film technology

The first solar cell was manufactured by Bell Laboratories in 1954, producing a 6% efficient module using crystalline silicon as the absorbing material[10]. Technological advances since then have enabled efficiencies up to 25% (as reported by University of New South Wales) for c-Si cells, close to the calculated theoretical limit a single junction solar cell of this material[25]. Since the birth of the photovoltaic market in the 1950s silicon has been the semiconductor of choice for solar cell devices, and today wafer-based silicon cells account for 80% the photovoltaic market [73]. Several factors have placed silicon as the dominant material for photovoltaics. Silicon is nontoxic and relatively abundant in the earths crust, accounting for 27.7% by mass, and therefore avoids any scarcity issues associated with the acquisition of raw material [58]. In addition, silicon processing is already a well-established industry, and solar cell fabrication can thus capitalize on the wide availability of processing knowledge. While silicon, as an indirect bandgap semiconductor, harbors challenges in light absorption, the bandgap is nearly ideal for maximizing the largest fraction of the solar spectrum in a single-junction solar cell device [89]. Even as crystalline silicon wafer-based cells dominate the market now, any cost reduction in this technology is limited by inherent materials expense.

A typical silicon-based solar cells has a thickness of approximately 100-300μm, and this silicon material accounts for about 40% of the total module cost [46]. For this reason, we seek an alternative technology that can decrease production and materials costs while maintaining marketable efficiencies; thin film silicon solar cells have the potential to satisfy both of these requirements. Recently, alternative materials such as amorphous silicon (a-Si), CdTe, CIGS, and GaAs have been the subject of recent research for the advantages they offer, such as decreased materials cost (a-Si) and increased theoretical efficiency limits (III-V materials). These alternative materials represent a shift from wafer-based solar cells to thin films that can be supported by inexpensive substrates, thus offering significant reductions in materials cost.

In addition to the lower material requirements and higher throughput that thin-film solar cell fabrication offers, this cell geometry also has the potential to increase the device efficiency. Having an active layer that is thinner than the carrier diffusion length will reduce recombination losses in the active layer, consequently increasing the open-circuit voltage of the device by decreasing the dark current and increasing carrier collection efficiency at the contacts. However, the absorption length of silicon is significantly larger than the diffusion length of the generated carriers. The absorption depth, the thickness of silicon necessary to absorb at least 67% of incident light (with $1/e$ fraction of light lost to transmission through film), increases with increasing wavelength (Figure 1.8). As a result, a large portion of the incoming infrared light is not absorbed by the silicon active layer. Figure 1.9 exhibits the absorption of light for varying silicon thicknesses as a fraction of the incident AM 1.5 solar spectrum, demonstrating significant losses as the thickness decreases from 10um to 220nm in the entire wavelength range λ=600nm to 1000nm, resulting in large power generation

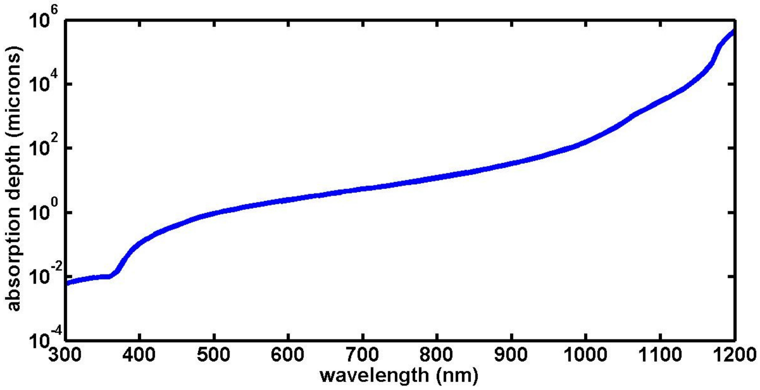

Figure 1.8. Silicon absorption depth with wavelength; thicker layers are necessary for sufficient absorption at long wavelengths.

losses. Since the optical power absorbed decreases with decreasing thickness, thin

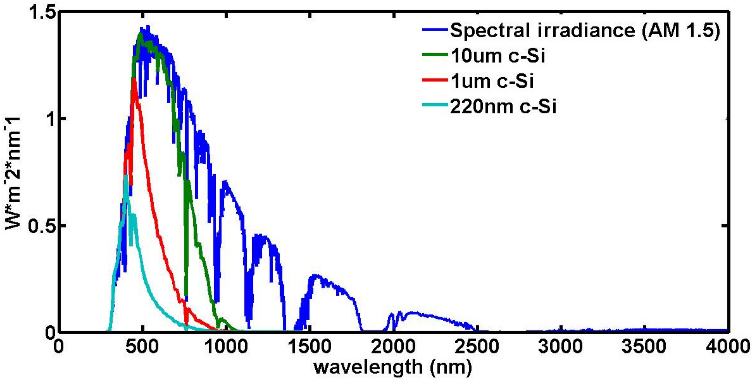

Figure 1.9. Fraction of AM 1.5 solar spectrum absorbed by varying silicon thickness, showing large losses in the infrared portion of the spectrum with decreasing thickness.

films will suffer a significant decrease in carrier generation and J_{sc} and cannot achieve the performance of bulk cells unless this loss in absorption is prevented. To overcome this hurdle, light trapping mechanisms can be employed to effectively increase the path length of the incoming light through the absorbing thin film layer by directing it laterally through the device. This can be accomplished via scattering, waveguiding, or plasmonic field enhancement, and an increase in the effective path length of light in the thin film results in an exponential increase in absorption.

1.4 Thin-film solar cell materials selection

As the market share of photovoltaics continues to grow, the manufacturability, availability of raw materials, and scalability of any developing technology must be considered. Currently there are several approaches to thin-film solar cells vying for a prominent position in the solar market. Several semiconducting materials have been investigated and used in thin film solar cells, and such factors as the availability of the active materials used and the environmental impact of the processing of this material must be considered alongside the potential economic viability of each type of photovoltaic device. Considerable research and product development has been dedicated to such materials as Copper-Indium-Gallium-Selenide (CIGS), Cadmium Telluride (CdTe), Gallium Arsenide (GaAs), and Amorphous Silicon (a-Si) [34, 35, 47, 56, 84, 87]. CIGS has a direct band gap accompanied by a high absorption coefficient, and for this reason is a promising active material for thin film devices. CIGS is naturally a p-type material and as such is used in heterojunction structures, most often with n-type cadmium sulfide (CdS) [89]. By controlling the stoichiometry of this material, the band gap can be adjusted to maximize performance, but CIGS cell fabrication is inherently complex, and at present the development of this technology is inhibited by challenges in the fabrication process. The current record CIGS cell reports an efficiency of 19.5%[25], and there is significant potential for increasing this efficiency, but the expansion of production levels is limited by the availability of indium[89]. Devices fabricated with CdTe have demonstrated relatively high efficiencies; the record for a single junction CdTe solar cell has recently been set by First Solar at 17.3%[77]. The band gap of CdTe is nearly ideal for a single junction cell, 1.45eV, however, the toxicity of cadmium is a concern, and important markets such as the European Union and China have restrictions on the usage of this material or its compounds[31]. GaAs is an attractive material for thin film solar cells due to its high electron mobility and direct band gap but is currently very expensive. The potential of this material, however, has been recently demonstrated by a record cell efficiency of 28.2% from Alta Devices for a device based on GaAs[9, 15, 25]. In contrast to the economic and environmental limitations currently placed on these materials, silicon is readily available, non-toxic, and its production is easily scalable using well-established manufacturing infrastructure.

Several technologies are currently employed and being developed to fabricate thin-film silicon solar cells. Perhaps the most established technology is amorphous silicon (a-Si), deposited via plasma-enhanced chemical vapor deposition (PECVD). Recently a stabilized efficiency upwards of 10% has been reported by Oerlikon Solar Lab for a thin amorphous silicon active layer deposited on soda lime glass[66]. This material has an inherent disadvantage in its metastability and disorder, but remains a viable technology due to its higher bandgap and inexpensive processing. Microcrystalline Si and nanocrystalline Si (μc-Si and nc-Si) are materials with crystallites in the nanometer to micron range in an amorphous matrix, and which contains less defects than amorphous silicon. Its lower band gap makes it particularly appropriate as active material for the bottom cell in tandem and triple junction devices. The combination of an amorphous silicon top cell and a microcrystalline bottom cell has yielded promising results, and a cell efficiency >12% has been reported by Oerlikon, but much work is needed to implement it over large areas and to limit light-induced degradation. Finally, thin-film polysilicon solar cells, with grain size in the micrometer range, have recently emerged as an alternative photovoltaic technology. The layers have a grain size ranging from 1m to several tens of microns, and are formed at a temperature ranging from 600 °C to more than 1000 °C. In general, polycrystalline thin-film silicon can be deposited on a wide variety of substrates, depending on the fabrication specifications and device parameters. For these films to be viable as solar cell materials, they must demonstrate adequate doping, minimum surface recombination, and stability over time. This thesis examines deposited silicon films using Hot-wire chemical vapor deposition (HWCVD) and characterizes the electronic and mechanical properties of these films to assess their potential for use in solar cell devices.

1.5 Challenges to thin-film solar cell technology

In order to be a viable alternative to bulk-based silicon solar cells, thin film silicon cells must offer a competitive efficiency. One of the main limitations to thin-film silicon solar cells is their inability to capture a large portion of the incident solar flux due to the indirect band gap and low absorption coefficient of this material. For this reason much research has been dedicated to the development of light-trapping methods for these devices. This thesis examines the potential for several different approaches to light scattering: physical scattering of the incident light at either/both the front and back of the cell, plasmonic near-field enhancement using metal nanoparticles, and physical scattering into resonant modes of the scattering structures. The goal of this thesis is to explore the potential for achieving a high efficiency cell utilizing a low-cost material by appropriately designed cell architecture.

Chapter 2

Hot-Wire Chemical Vapor Deposition for Silicon Thin-Film Growth

2.1 Scalable methods for uniform and high-quality film deposition

Methods for thin-film growth must produce high quality films at sufficiently high growth rates while providing uniform deposition over a large area for feasible application to solar cell device manufacturing. Several deposition techniques have been researched and utilized extensively for depositing silicon films, including plasma-enhanced chemical vapor deposition (PECVD), molecular beam epitaxy (MBE), and hot-wire chemical vapor deposition (HWCVD). PECVD is a commonly used thin film deposition method that has been shown to produce device-quality silicon films. However, this method is expensive, has a relatively slow growth rate, and introduces ion damage to the growth surface [39]. The MBE technique involves the evaporation of a silicon source with subsequent deposition onto a substrate under ultra-high vacuum conditions, and this method has also been shown to produce high-quality films; however, this method is expensive and has low through-put and therefore not practical on an industrial manufacturing scale. The economic feasibility of a deposition technique relies on a high growth rate and scalable production, and to this end HWCVD has been explored for high-quality growth of crystalline and amorphous silicon. HWCVD film growth is an attractive method for deposition of thin-film silicon for use in the manufacturing of photovoltaic devices due to efficient use of precursors, fast deposition rates, and passivation of defects due to hydrogen inclusion, while at the same time offering scalability, low cost, and a low-temperature deposition process that permits the use of low cost substrates. HWCVD silicon thin film solar cells deposited on inexpensive soda lime glass have the potential to match the efficiency of wafer-based silicon solar cells at the low cost of a-Si thin film-based cells [17]. For this reason the growth of silicon thin films via this method has been investigated, with optimal deposition conditions evaluated for high-quality thin film growth. As will be discussed in detail in the course of this chapter, an examination of films deposited on crystalline silicon substrates reveals epitaxial growth, while silicon films grown on glass substrates demonstrates significant crystalline fractions despite the absence of a seed layer. This result demonstrates the potential for the fabrication of device-quality silicon layers on inexpensive substrates. However, these films are not fully crystalline and can have varying physical structures depending on the deposition conditions that affect the material and electrical characteristics. While thin-film devices can tolerate a higher density of defects due to the decrease in necessary path length for efficient carrier collection, the increased surface-to-bulk ratio increases the significance of surface geometry and defects, while a finite grain size increases the likelihood of bulk recombination at trap sites between the grains. Efficient carrier collection requires sufficient passivation at grain boundaries to increase the probability of minority carriers diffusing to the junction rather than combining at these boundaries; the degree of defect passivation determines in large part the optimal electrical performance achievable by photovoltaic devices fabricated from these films. This study therefore focuses on the correlation between both bulk and surface passivation with the electrical properties of the films, with the goal of maximizing the stabilized performance of HWCVD films for use in thin-film silicon solar cells.

2.2 HWCVD background

This method of using heated wires to decompose source gases as a mechanism for thin film growth was first reported in 1979 by Weismann, et al., who demonstrated

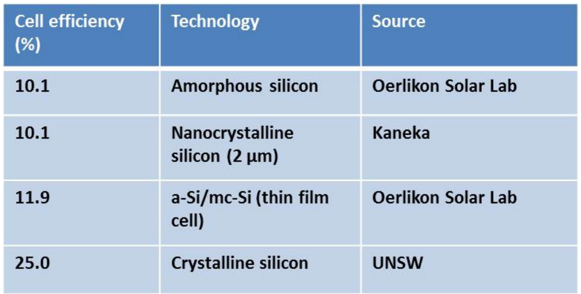

Cell efficiency (%)	Technology	Source
10.1	Amorphous silicon	Oerlikon Solar Lab
10.1	Nanocrystalline silicon (2 µm)	Kaneka
11.9	a-Si/mc-Si (thin film cell)	Oerlikon Solar Lab
25.0	Crystalline silicon	UNSW

Figure 2.1. Record efficiencies for thin film silicon solar cells are significantly lower than those of wafer-based silicon cells. [25]

the thermal decomposition of silane by heated graphite and tungsten sheets to yield amorphous hydrogenated silicon (a-Si:H) [64]. This method was further developed by Matsumura, et al., as an attractive alternative to PECVD, beginning in 1985, and by optimizing the deposition conditions they were able to demonstrate growth of device-quality amorphous Si [49]. The potential for producing films at a high growth rate ($100\mathring{A}$/s) and of a device quality superior to those grown via widely used PECVD was demonstrated by Mahan, et al., in 1991, indicating the potential for HWCVD films to be used as active layers in solar cell devices on a manufacturing scale [16]. Alberi, et al., fabricated an all-HWCVD solar cell with an efficiency greater than 5% with a heterojunction of 2μm of n-type epitaxially grown silicon with a-Si top layer on a Si-wafer template at process temperatures compatible with the use of soda lime glass substrates, here demonstrating the potential to further decrease the costs of devices made with these films by allowing low-cost substrates instead of c-Si [23]. Current thin-film silicon solar cell technologies and their record efficiencies are reported in Figure 2.1 and exhibit a large disparity between the performance of the these cells and wafer-based silicon cell efficiencies, which have reached 25%. [25] This again highlights the necessity for increased performance from thin-film silicon absorbing layers, and this chapter address methods for maximizing the V_{oc} through appropriate film deposition parameters.

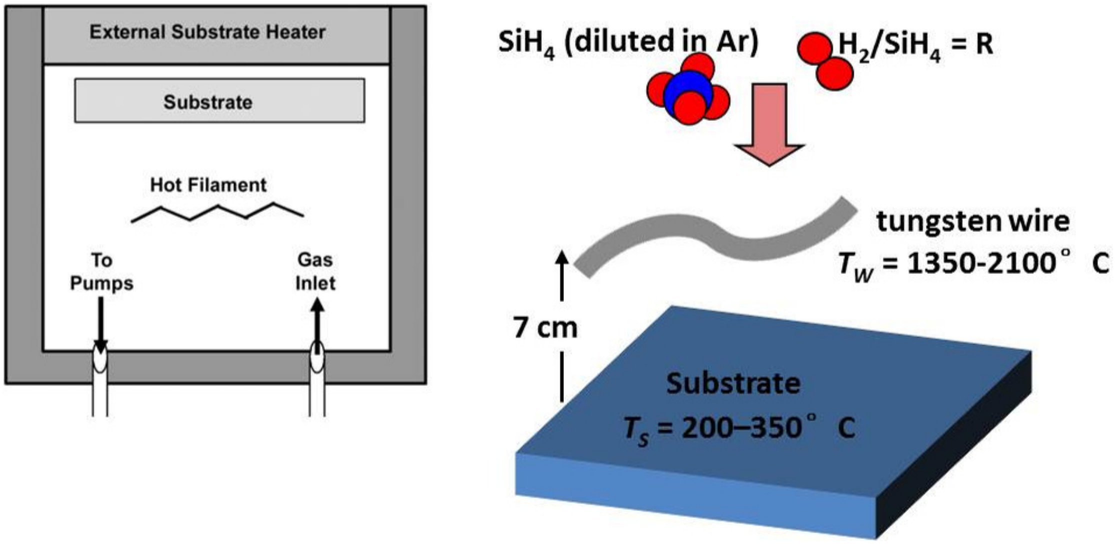

Figure 2.2. Schematic of vaccum chamber setup for HWCVD film growth.

2.3 HWCVD experimental setup

The deposition of thin films via HWCVD is accomplished by introducing gaseous precursors into a vacuum chamber in which the gases then thermally and catalytically decompose at a resistively heated wire filament. Using silane and hydrogen as precursors, the silicon will break down to subspecies (H, Si, SiH$_{0-3}$) and deposit onto the substrate. This process is accompanied by hydrogen etching of the surface as well as H-deposition at dangling bonds, resulting in removal and redeposition of species at the surface and bulk passivation where hydrogen is incorporated. The role of hydrogen and its incorporation in the film is determined by the temperature of the substrate and the ratio of SiH$_4$/H$_2$, hereafter referred to as 'R'. The setup includes a cluster tool with a centralized vacuum chamber through which a robotic arm moves a substrate holder to the designated deposition chamber (Figure 2.2). The deposition chamber contains a substrate holder distanced from a wire assemby by 7cm. The wire assembly is connected to power via two electrical leads passed into the chamber and isolated with ceramic spacers; the wire is resistively heated to temperatures ranging from 1400 °C to 1700 °C as determined by an optical pyrometer. For the HWCVD films grown in this study, 5% silane in argon, diluted to the appropriate R-value by varying the hydrogen flow was used, with a total chamber pressure varying from 4mTorr to 120mTorr and with the partial pressure of SiH_4 maintained at a constant value. For doped films, 1% trimethylboron (TMB) diluted in argon was used for p-type and 1% phosphine (PH_3) diluted in argon was used for n-type. Films were deposited on both soda lime glass and Czochralski-grown silicon(100) wafers doped with phosphorous to a concentration of $1x10^{19}cm^{-3}$, and the samples were prepared with a heated RCA2 clean followed by a 30s buffered HF dip to remove, respectively, organic contaminants and the native oxide layer. The samples were then immediately placed on the substrate holder and put under vacuum in the load lock of the cluster tool.

2.4 Mechanisms for thin film growth

One of the primary variables that determine the physical and electrical properties of a HWCVD silicon film is the quantity of hydrogen available to interact with the decomposed SiH_4 during film growth. In order to understand the role of hydrogen in film morphology during film growth, several studies have been conducted to determine an appropriate growth model for films grown with HWCVD. For sufficiently heated wires, the SiH_4 and H_2 precursors are completely decomposed into atomic H and Si at the wire [18]. Under low pressure deposition conditions, the Si and H resulting from this decomposition at the heated filament can have subsequent reactions with other gaseous species present in the chamber before depositing on the substrate [41]. These subsequent reactions produce SiH_3, Si_2H_2, and Si_2H_4, along with atomic hydrogen and H_2, each of which in turn act as the primary deposition species at the substrate in proportions that are highly dependent upon deposition conditions such as substrate temperature and gas partial pressure [26]. Tao, et al. proposed a model for epitaxial growth based on the free energy change as silane species form bonds with the Si on the substrate surface [85]. The incoming Si species will form Si-Si and H-Si bonds with the surface. Due to the presence of excess H, any dangling bonds present will be saturated, and the net free energy change under formation of these bonds is negative, resulting in a stable configuration. The crystallinity of the deposited silicon film is determined by this hydrogen incorporation at dangling bonds and desorption during deposition as well as diffusion of surface species [43]. Mason, et al., proposed that this inclusion of hydrogen in the growth species prevents contaminant incorporation in the film while allowing silicon deposition [61]. Studies conducted by Holt, et al., have further indicated that incoming hydrogen will preferentially etch amorphous silicon deposited on the substrate, resulting in an enhancement of crystalline growth [22]. The properties of the resulting film are therefore highly dependent upon temperature of the wire and the substrate temperature; an increase in substrate temperature will result in an increase in diffusion of surface species into a crystalline structure with a lower free energy, while the initial deposition species are determined by the temperature of decomposition at the filament.

2.5 Hydrogen and film properties

For HWCVD films to be useful in a solar cell device, they must demonstrate sufficient and stable electronic properties. The initial measurement and the stability of V_{oc} of these films is an indication of the extent of the bulk and surface passivation and is determined in large part by the incorporation of hydrogen in these films. The presence of hydrogen during HWCVD film growth greatly affects both the material and electrical properties of the silicon film, influencing the growth rate, density, and bulk and surface passivation. Due to this incorporation of hydrogen in HWCVD silicon thin films, different hydrogen dilution ratios (H_2/SiH_4) result in films with varying characteristics. Since an amorphous morphology inherently contains many structural and bonding defects, this often results in a large density of dangling bonds, and for this reason a high crystalline fraction is expected to yield a higher and more stable V_{oc}. The surface morphology and growth evolution of silicon films grown

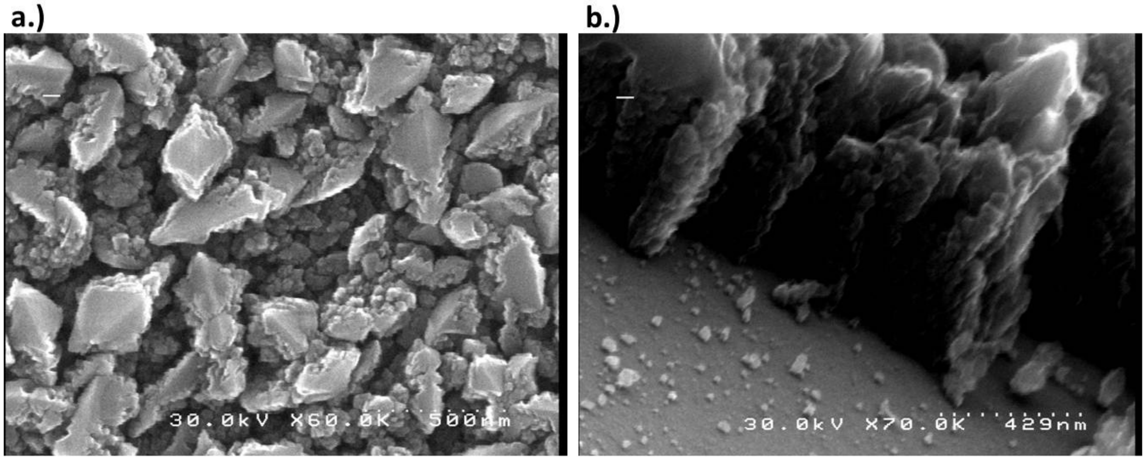

Figure 2.3. SEM micrograph of HWCVD silicon film surface in a.) plan-view and b.) at a 75° angle.

under various levels of hydrogen dilution is therefore examined in this study, and the resulting variety of film structures provides insight into the subsequently measured electrical properties of these films.

2.5.1 Material properties with hydrogen dilution

The influence of hydrogen content in these films on the resulting physical characteristics was explored by systematically varying the hydrogen flow during film growth. The physical properties and structural evolution of these films with varying growth parameters was examined through cross-sectional transmission electron microscopy (XTEM) and Raman spectroscopy. Previous studies have demonstrated an increase in porosity with increasing hydrogen dilution during film growth due to the incorporation of hydrogen in these films [74]. A typical film is shown in Figure 2.3 and shows a granular surface texture with pores permeating to the substrate interface.

Cross sectional transmission electron microscopy (XTEM) was employed to deter-

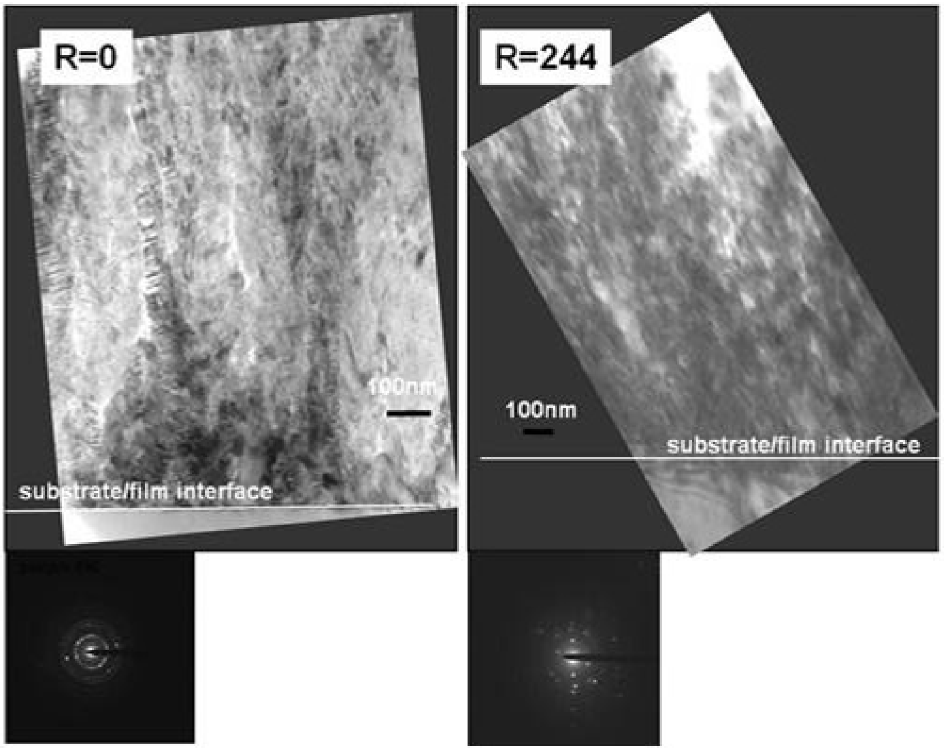

Figure 2.4. XTEM images show evolution of thin-film silicon cross-section with hydrogen dilution, exhibiting increasing porosity with increasing hydrogen incorporation. SAD patterns demonstrate a higher degree of crystallinity for films grown with higher values of R.

mine the extent of this network of pores, and the crystalline structure of the film was obtained through the use of a selected area diffraction pattern (SAD). This analysis technique uses the regular arrangement of atoms in a crystalline structure to create a pattern of spots resulting from the regular diffraction of incoming light. By using a small (selected area) aperture in the TEM focused on the region of interest, the crystalline nature of the film can be determined. In contrast, an amorphous film will exhibit no regular pattern; the SAD images therefore yield insight into the overall crystalline nature of the silicon film. The resulting images illustrate the physical cross section of the film as well as the atomic structure, and these observations demonstrate the effect of hydrogen on the evolution of the film during growth (Figure 2.4), and distinct regimes are observed with the variation of hydrogen. Films grown with no additional hydrogen (R=0) are dense and a mixture of amorphous and polycrystalline, as indicated by the accompanying selected area diffraction (SAD) pattern. A high density of stacking faults is observed, and some disordered porosity is detected throughout the film. When hydrogen is mixed with the incoming silane (R=244) during deposition, the film is much more pore-permeated and far less dense than films grown with no additional hydrogen. The accompanying SAD pattern shows that these films are twinned polycrystalline.

Previous studies have determined an increase in the crystalline fraction and crystalline grain size of the film with increasing hydrogen dilution during growth [21, 74]. This phenomenon was verified in these films by using Raman spectroscopy to correlate the crystalline fraction with hydrogen content and porosity. Raman spectroscopy is a materials characterization method that measures the inelastic scattering of an incident light source; this technique works by measuring the shift in the energy of the light as it interacts with phonons in the sample, with the shift being characteristic of the type of bond being probed by the incoming light. Various types of bonds have different vibrational modes that cause a unique shift in the energy shift of the light, and the observation of these signature shifts gives us insight into the composition of the material studied. For the purposes of these measurements, the relative heights of peaks corresponding to crystalline and amorphous silicon are examined; a peak at 521cm^{-1} is indicative of crystalline silicon (2nd-order TO mode), while a peak at 480cm^{-1} indicates amorphous silicon. These Raman spectroscopy measurements show that all of the films grown with additional hydrogen ($R< 0$) are fully crystalline, indicated by the silicon peaks at 521cm^{-1}, while the film grown with no additional hydrogen (R=0) appears to have an amorphous fraction, with a shoulder emerging towards the amorphous 480cm^{-1} peak (Figure 2.5). This demonstrates that additional hydrogen results in fully crystalline films, but an increase in H-dilution does not necessarily cause a concurrent increase in crystalline fraction.

Identical films were then grown on both Si(100) and soda lime glass to compare the effects of hydrogen dilution on the growth morphology of films on a non-crystalline template with those grown on c-Si(100). The objective was to determine if sufficient

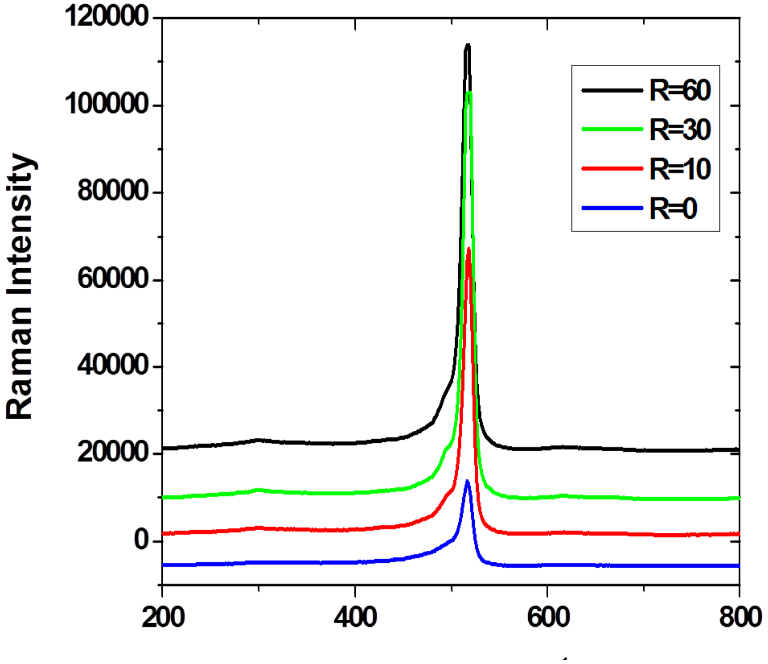

Figure 2.5. Raman spectroscopy measurements with changing hydrogen dilution show high crystalline fraction for all values of R>0; the y-axis is an arbitrary scale with measurement results shifted to highlight peak location.

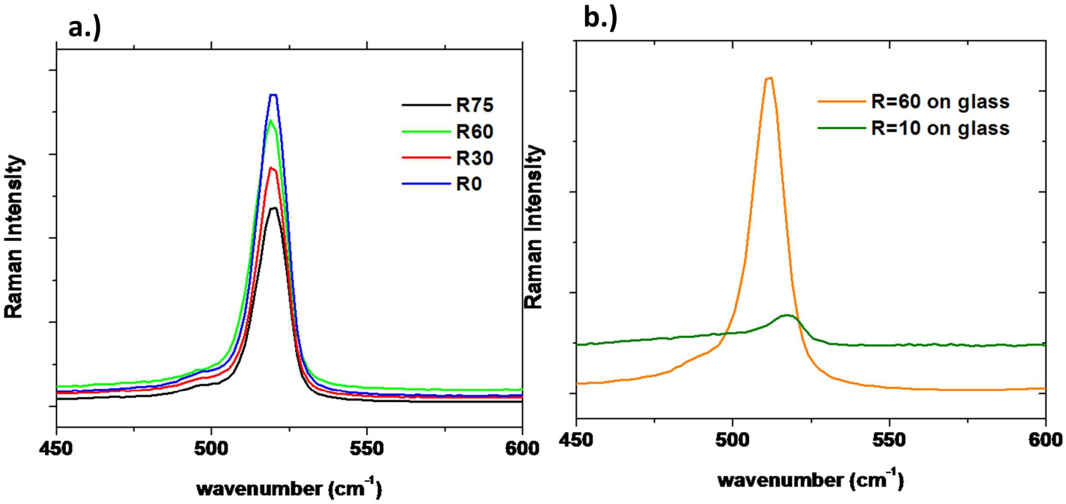

Figure 2.6. Raman spectroscopy measurements for a.) crystalline silicon(100) substrate and b.) soda lime glass demonstrate that a high crystalline fraction is achievable even on an amorphous substrate.

hydrogen dilution during growth is able to cause growth of a crystalline film, even without the template of a crystalline wafer. Here the results show that while films grown with the same hydrogen dilution have a sharper crystalline peak for films grown on a crystalline substrate than for those on glass, indicating, as expected, that the use of a crystalline substrate provides a template for epitaxial growth that allows for a higher crystalline fraction in the resulting film. (Figure 2.6). The film for R=10 on glass shows a significant shoulder towards the amorphous peak at 480 cm^{-1}, while a clearer crystalline peak is seen for the film grown with R=60 on glass. The shift down of this location of this peak may indicate a smaller crystallite size or a higher amorphous fraction [57]. Thus the addition of hydrogen is seen to promote crystallinity for films grown on amorphous glass substrates, but more hydrogen may be necessary to achieve the same level of crystallinity when growing films without a crystalline template. H-dilution greater than 0 does not result in fully crystalline films as it does for films grown on c-Si(100). Most significantly, this shows that hydrogen dilution assists crystalline growth even in the absence of a crystalline template, indicating that a highly crystalline film is achievable even in the absence of a crystalline template.

The results of these measurements indicate that diluting the precursor gas with hydrogen not only promotes crystallinity but also results in a columnar, pore-permeated structure. Hydrogen content is therefore observed to strongly influence the density of the silicon film as well as the crystalline fraction. Pore-permeated growth with hydrogen dilution could be detrimental, despite its role in promoting crystallinity and passivation, in that oxygen may be allowed to penetrate deeply into the films and cause high lateral resistivity. For this reason the electrical properties of these films are examined to determine the potential for carrier collection in porous films with high-hydrogen incorporation.

2.5.2 Electrical characteristics of HWCVD films

To correlate the film morphology with the electrical characteristics of these films, the open-circuit voltage (V_{oc}) was measured and compared for each, since the V_{oc} can provide insight into such film characteristics as surface and bulk passivation. Recombination in the film will increase the dark current, resulting in a lower V_{oc}.

$$V_{oc} = \frac{kT}{q}(ln\frac{I_{light}}{I_{dark}}) \tag{2.1}$$

Here I_{dark} is the sum over all defects and impurities of the product of the recombination rate and the defect density. V_{oc} is therefore an indication of the level of passivation in the film and a valid predictor of the ultimate performance of the finished solar cell. The inherent surface passivation of these films via native oxide or hydrogen contained in the film can therefore be inferred from the shift in V_{oc} over time. To acquire the V_{oc}, a Sinton Consulting Suns-V_{oc} measurement system was employed. This method illuminates the sample with a slowly varying light source while simultaneously measuring the output current and voltage from the device. The variation in incident light intensity is measured by using a calibrated test cell with a known photogeneration rate. The principle behind this technique is that it measures the light intensity with V$_{oc}$, rather than the standard method of measuring the variaiton in short-circuit current with V$_{oc}$ [76]. This has the important advantage of allowing measurements at any point after junction formation, eliminating the need for metallization and requiring instead a minimal probe. This method can be used to study the junction and film quality of our device without the added complexity of added variables necessarily introduced with contact formation.

Since Raman spectroscopy demonstrated fully crystalline silicon films for all values of R, the increase in V$_{oc}$ is therefore not likely due to an increase in crystalline fraction with hydrogen dilution. The added hydrogen content during growth is likely playing a different role in enhancing V$_{oc}$ than merely increasing the crystalline fraction of the film. To investigate this, the V$_{oc}$ of p-type boron-doped films grown via HWCVD on n-type 1x10^{15} cm^{-3} phosphorous-doped Si(100) substrates was measured. The V$_{oc}$ of films grown under conditions of varying hydrogen dilution has been measured both immediately following growth and after 1 week in ambient air (Figure 2.7).

The increase in V$_{oc}$ for films grown under lower hydrogen dilutions demonstrates that these films are limited by surface passivation, and thus sufficiently hydrogen-passivated in the bulk. Sufficient bulk passivation can be assumed in films that demonstrate an increase in V$_{oc}$ with the formation of native oxide to passivate the surface; if the device performance was limited by bulk passivation, the increase in V$_{oc}$ from surface passivation would not be observed. For films grown with higher H-dilution, a decrease in V$_{oc}$ is observed over time in ambient air. Referring to the XTEM images (Figure 2.4), higher H-dilution results in a pore-permeated growth structure. This greater surface area and porous network for films from this higher H-dilution regime will make them more difficult to passivate at the surface and in the bulk, limiting the ability of native oxide to have the same effect as on denser, lower H-dilution films. In addition, the higher porosity may allow a more rapid rate of hydrogen desorption from the film, decreasing the level of bulk passivation over time. In a subsequent series of film growths, the initial V$_{oc}$ was measured after 2 weeks in ambient air, and then after an HF dip removing the native oxide (Figure 2.8).

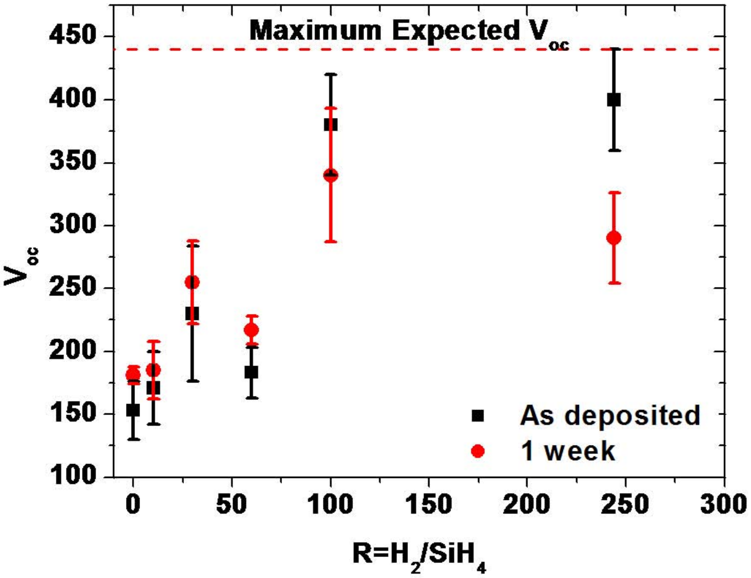

Figure 2.7. Change in open-circuit voltage over one week in ambient air for varying hydrogen dilutions exhibits higher instability for greater values of R.

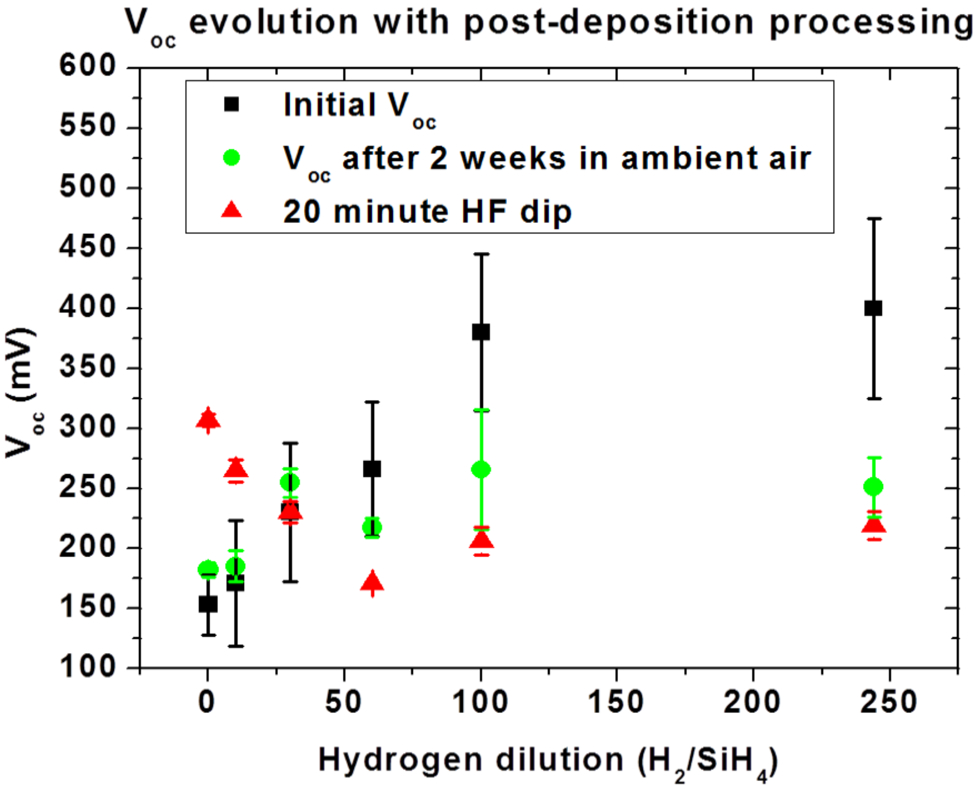

Figure 2.8. Results of post-deposition treatments on open-circuit voltage of films for varying hydrogen dilution.

Again a decrease in V$_{oc}$ is observed after this extended period in ambient air for those films grown with high H-dilution. The HF dip is shown to increase the V$_{oc}$ for low H-dilution films, but decrease for films with high H-dilution. As seen in the previous measurements, if the films are sufficiently passivated by H-termination of defects in the bulk, then an increase in Voc with native oxide formation is expected. A subsequent HF dip would then be expected to decrease the V$_{oc}$ as this oxide is removed and the surface is exposed. For films with low H-incorporation, the bulk may not be sufficiently passivated, so little increase in V$_{oc}$ over time is expected. Hydrogen from the HF dip, however, may penetrate these pores and passivate defects within, resulting in the observed increase in V$_{oc}$ with HF post-deposition treatment.

2.6 HWCVD-grown p-n junctions

The quality and characteristics of junction at the interface between a crystalline silicon substrate and a grown film differ significantly from those of a junction at an interface between two grown films. To determine the quality of these grown junctions, n-type silicon films with p-type emitter layers were deposited in succession on a n+ Si(100) substrate. The XTEM image shows such a junction deposited on a crystalline substrate (Figure 2.9). The cross section indicates that different dopant types affect the material structure of the resulting film in different ways. Both layers are grown with no additional hydrogen dilution, and both have a high amorphous fraction, as demonstrated by the accompanying SAD patterns. The n-type film also shows a disordered pore-permeated growth, while the p-type layer shows the emergence of a more regular columnar growth. The following XTEM image exhibited in Figure 2.10 shows a film with an identical layering structure as the previous image, but grown with a hydrogen dilution ratio of R=20. Referring to the SAD patterns, both the n- and p-type layers display a more crystalline structure than those grown with no additional hydrogen. This result is again attributed to the influence of H-dilution in promoting crystalline morphology during growth. The same pore-permeated structure in the n-type is observed, again giving way to a columnar structure in the p-type. The

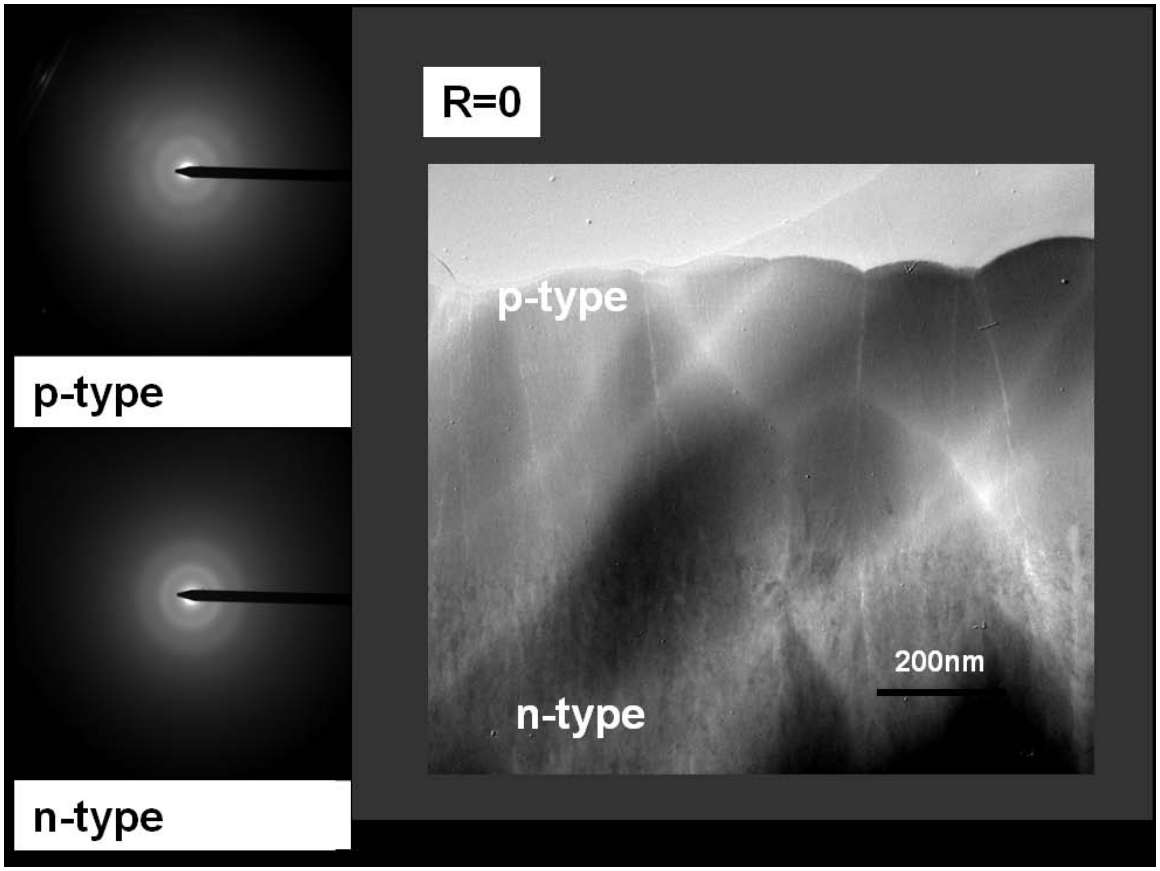

Figure 2.9. TEM cross-section of grown p-n junction on silicon(100) substrate for R=0.

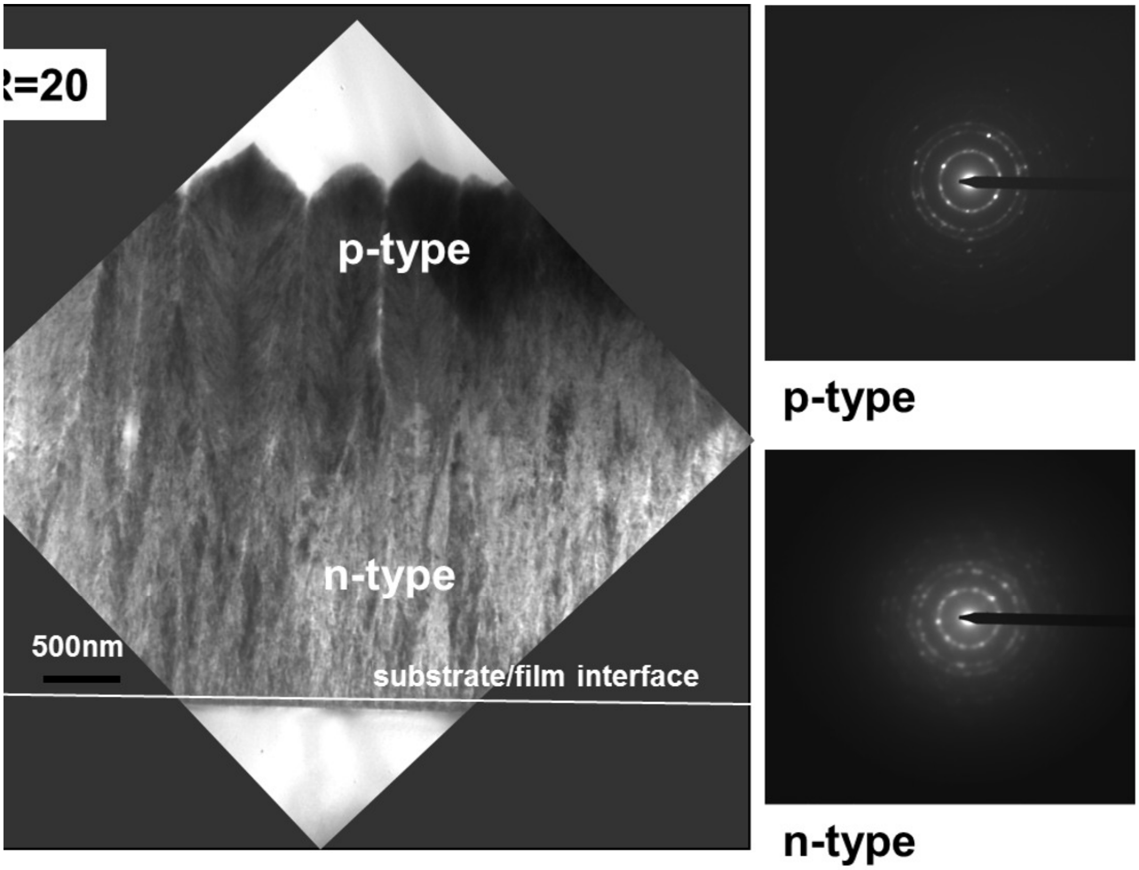

Figure 2.10. TEM cross-section of grown p-n junction on silicon(100) substrate for R=20.

SAD also indicates a higher amorphous fraction in the n-type film, indicating that dopant incorporation effects the resulting structure of the film. Raman spectroscopy compares the crystallinity of these past two films seen in crossection. Subsequent Raman spectroscopy measurements reveal a highly crystalline peak for the structure grown with R=20, but a signature amorphous peak for the structure grown with no additional hydrogen. While an initial examination could lead to the conclusion that this is further evidence of the role of hydrogen in promoting crystallinity in these films, a further study of the Raman measurement technique requires an alternate perspective of this plot. The laser used for Raman measurements has a wavelength of λ=514nm, which has a penetration depth in crystalline silicon of approximately 762nm. For the junction structure with R=0, the penetration depth coincides with n-type layer, while for the R=20 structure this depth coincides with the p-type structure due to differences in thickness that result from varying growth rates with H-dilution. The results of the Raman measurements therefore affirm not the role of H-dilution with crystalline structure, but reveal instead the influence of doping type in determining film morphology and demonstrate that boron incorporation may increase the crystalline fraction of the silicon film (Figure 2.11). The growth morphology and crystalline fraction of HWCVD silicon thin films is thus determined by both hydrogen content and doping incorporation; to realize a well-passivated crystalline n-type film grown will require additional hydrogen flow during growth, while for a p-type structure additional hydrogen may not be necessary.

2.7 Dopant incorporation

The incorporation of impurities in HWCVD silicon films not only plays an important role in determining film structure, but also determines in large part the resulting electrical characteristics of the device. Optimal dopant incorporation is vital to device performance and has historically been a formidable challenge in HWCVD films. A highly doped emitter, in this study the p-type silicon layer, is necessary to increase the quality of contacts to the device; however, increased recombination results from

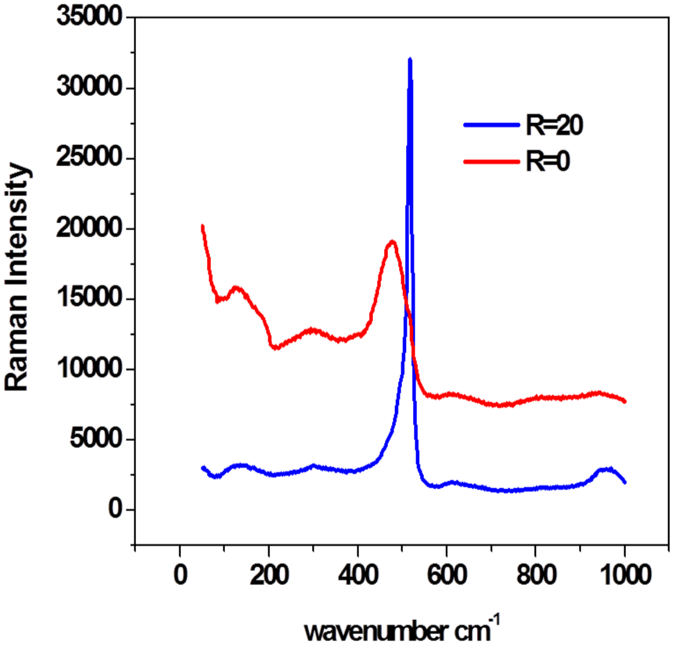

Figure 2.11. Raman spectroscopy of grown junctions for R=0 and R=20 illustrate the effect of dopant incorporation on crystalline fraction.

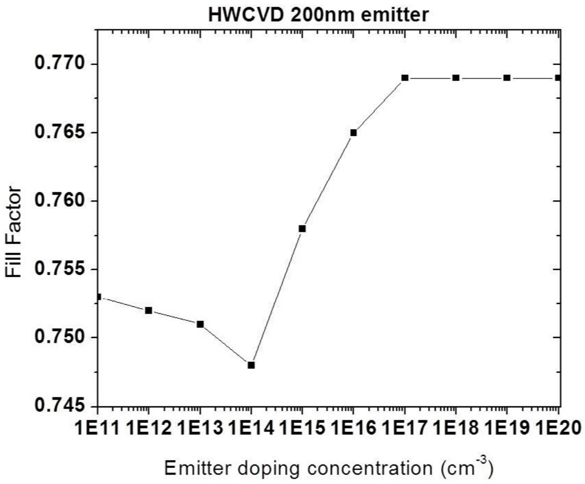

Figure 2.12. PC-1D optimization of emitter doping for 2μm device thickness, 200nm emitter thickness, 1 ohm contact resistance, 100 cm/s SRV, 7μm diffusion length, and 10^{15}cm^{-3} base layer doping .

the increased doping level, and maximizing the potential device efficiency requires optimization of the emitter doping considering these factors. An optimal doping concentration has been calculated for this device structure through the use of PC-1D simulation software. PC-1D is a program developed by the University of New South Wales that solves the electron and hole transport equations for one-dimensional travel through a semiconductor structure and allows input parameters such as device thickness, contact resistance, surface recombination velocity, and diffusion length. The output of this program can provide insight into device design optimization, and simulations for structures representative of HWCVD devices illustrate emitter doping above 1x10^{17}cm^{-1} results in maximum fill factor of close to 77% for the device (Figure 2.12).

Previous studies of HWCVD silicon films have revealed higher incorporation of phosphorous atoms than boron atoms with the same concentration of doping gas during deposition, a result attributed to the variation in dissociation probabilities for doping gas elements [28, 55]. Spreading resistance analysis of HWCVD silicon films grown in our own facilities demonstrate moderate doping for TMB-doped films but

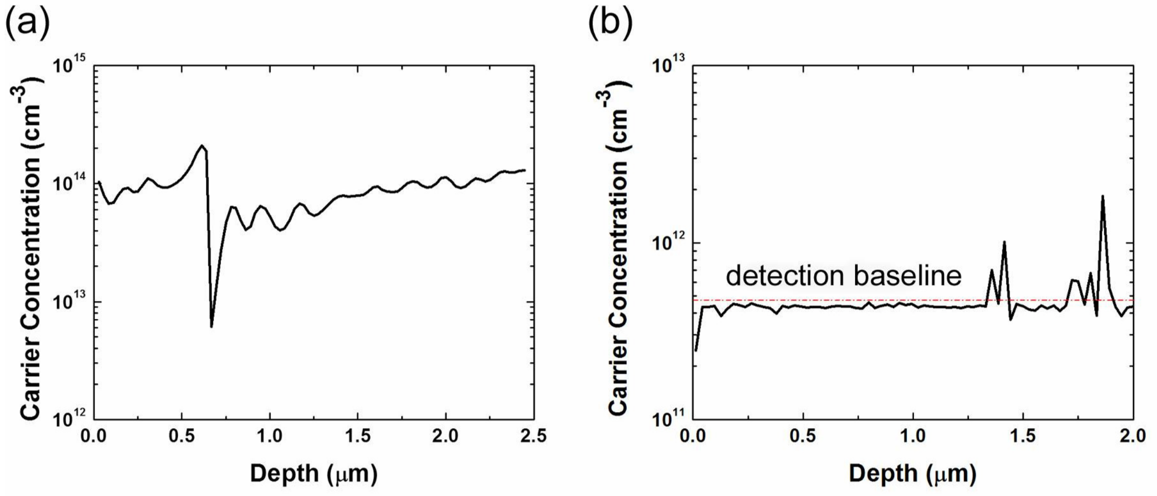

Figure 2.13. Spreading resistance analysis of HWCVD films show a.) doping levels of 10^14cm^{-1} for films grown with TMB as doping gas, but b.) undetectable levels for films grown with PH_3 [74].

extremely low dopant levels for those grown with PH_3 as the dopant gas (Figure 2.13) [74]. The incorporation of dopants depends on the thermal dissociaton of the doping elements by the heated filament in HWCVD deposiiton; if the PH_3 is not efficiently separated into its constituent elements, subsequent phosphorous incorporation in the silicon lattice is less likely. In addition, if boron-incorporation is indeed promoting a more highly crystalline growth morphology, boron can reside at substitutional sites in the silicon lattice, resulting in a more highly stable structure than a more amorphous structure with phosphorous inclusions. Previous studies present evidence for this phenomenon by using Raman spectroscopy to illustrate a suppression of crystallinity in HWCVD silicon films with increasing PH_3 dilution during growth[32]. For this reason alternative methods of depositing n-type silicon films may be necessary to achieve the doping concentration necessary for optimal device performance; the use of PECVD for n-type film deposition in conjunction with HWCVD for p-type silicon films may be an attractive option for optimizing device performance while maintaining the advantages of a high growth rate and scalability inherent in HWCVD fabrication.

2.8 Open-circuit voltage for grown junctions

A high crystalline fraction again is not a guarantee of desirable electrical behavior from a device fabricated from this film, and the inadequate doping of the emitter layer of the grown-junction structure will severely limit the resulting V_{oc}. To examine the relationship between film morphology and device performance, the V_{oc} of these grown-junction structures was measured immediately following film deposition, after 60 days in ambient air, and after a 10 minute dip in hydrofluoric acid (Figure 2.14). The initial V_{oc} measurement reflects the influence of hydrogen incorporation during growth, while the measurement after 60 days exhibits the electrical performance of these films after some hydrogen desorption takes place. A subsequent HF dip serves to not only remove the native oxide that has formed on these films during ambient air exposure, but also to potentially allow hydrogen to be re-incorporated in the film. The results for junctions grown on Si(100) wafers show a trend in V_{oc} with hydrogen dilution contrary to that observed for a film-wafer stack (Figure 2.14).

The initial V_{oc} is seen to decrease with increasing hydrogen dilution, not increase. Exposure to ambient air is seen to result in a significant decrease in V_{oc} at all hydrogen dilutions, while a removal of the native oxide with an HF dip results in a notable increase. From the XTEM images previously shown, the p-type layer at the surface of these films is shown to be columnar and pore-permeated, likely allowing for significant oxygen penetration into the bulk of the film. The benefits of hydrogen passivation therefore may be outweighed by the detrimental effect of oxygen penetration in these films, and the use of grown junctions for solar cell devices therefore requires a means for denser growth with alternative means of passivation.

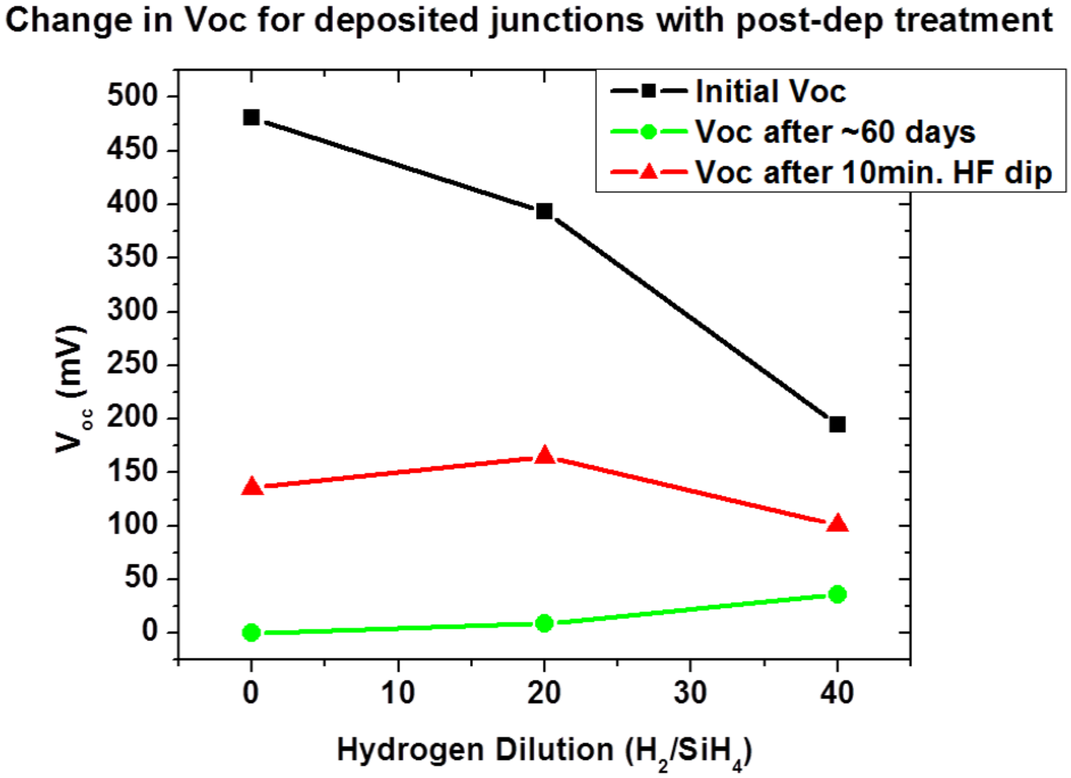

Figure 2.14. Change in open-circuit voltage with hydrogen dilution for grown p-n junctions.

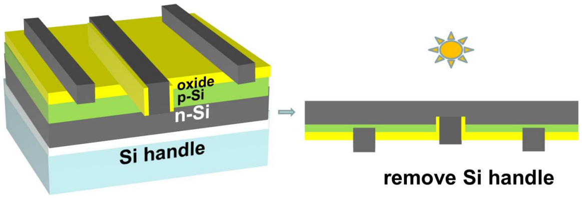

Figure 2.15. SOI thin-film device design with interdigitated back contacts.

2.9 Fabricated thin film devices on SOI with HWCVD emitter

To fully test the performance of HWCVD thin films for use in solar cell devices, thin film silicon test cells were fabricated using a 2μm c-Si device layer on oxide (SOI) structure as the base. The device design was based on the eventual use of a transparent glass superstrate and interdigitated back contacts for maximal carrier collection with minimal front shadowing as illustrated in Figure 2.15, with the ultimate goal of employing HWCVD and PECVD silicon films deposited on glass as the active layers in the device.

The purpose of this study was to build and measure a control cell to compare to subsequent thin film cell grown with HWCVD. By using a crystalline absorber layer and fabricating a suitably doped emitter, this control device can predict the highest expected performance from HWCVD cells grown with the same geometry. This design eliminates the need for a large minority carrier diffusion length through the use of closely-spaced interdigitated back contacts and utilizes oxide passivation layers fabricated via chemical deposition or thermal oxidation. The fabrication steps are outlined in Figure 2.16, and as an intial step toward realizing this device structure, cells with interdigitated fron contacts were first constructed on crystalline silicon substrates. SOI wafers with a 2μm device layer thickness of silicon doped with phosphorus to 10^{15}cm^{-3} were diffusion-doped with boron nitride wafers in a tube furnace under nitrogen flow

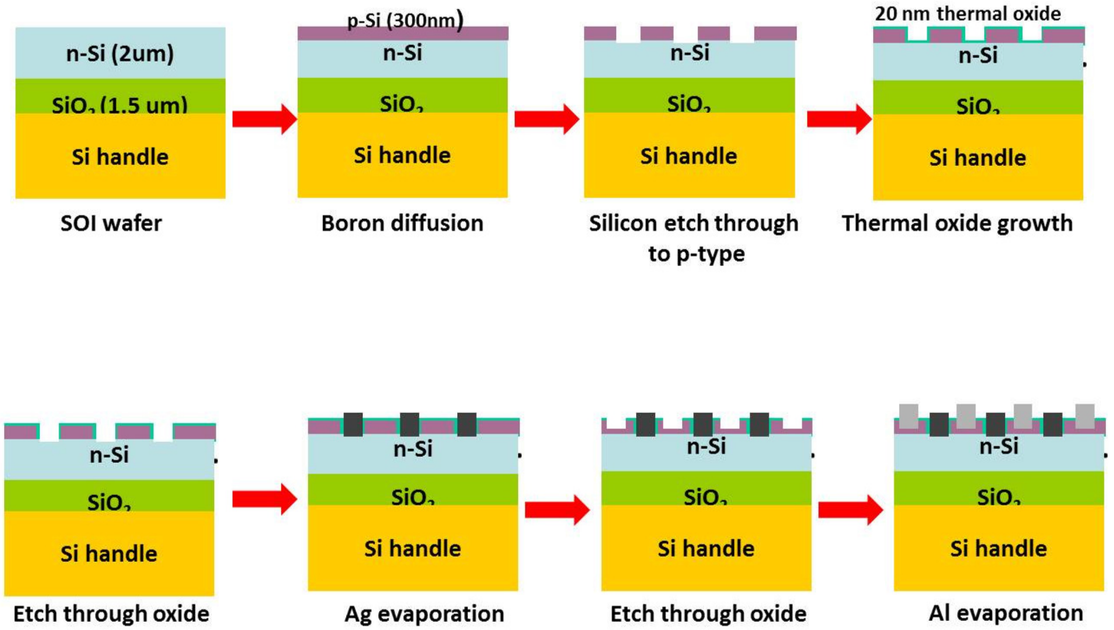

Figure 2.16. Fabrication steps for SOI thin-film device.

to form a p-type emitter layer with a thickness of 300nm; this method produces a suitable abrupt junction and sufficiently high doping levels, as confirmed by spreading resistance analysis performed by Solecon Laboratories (Figure 2.17). Interdigitated contacts were then fabricated by using several photolithography steps, metallization via thermal evaporation, and alignment processes, resulting in aluminum contacts to the p-type emitter and Ag contacts to the n-type base layer (Figure 2.18). The device was then characterized by measuring the current response through a two-point probe applied at each of the contacts under AM 1.5 illumination at 100W/m^2 and varying the voltage between -0.5V and 0.5V; the resulting current-voltage plot is presented in Figure 2.19.

This device demonstrates a J$_{sc}$ of approximately 0.1 mA/cm^2 and a V$_{oc}$ of 64mV, and the shape of the curve is characterized by an ideality factor much greater than 1. A large ideality factor is indicative of a high rate of carrier recombination in the space charge region of the device, and additional passivation measures are therefore necessary at the diffused junction. In addition, the slope of this curve and its deviation

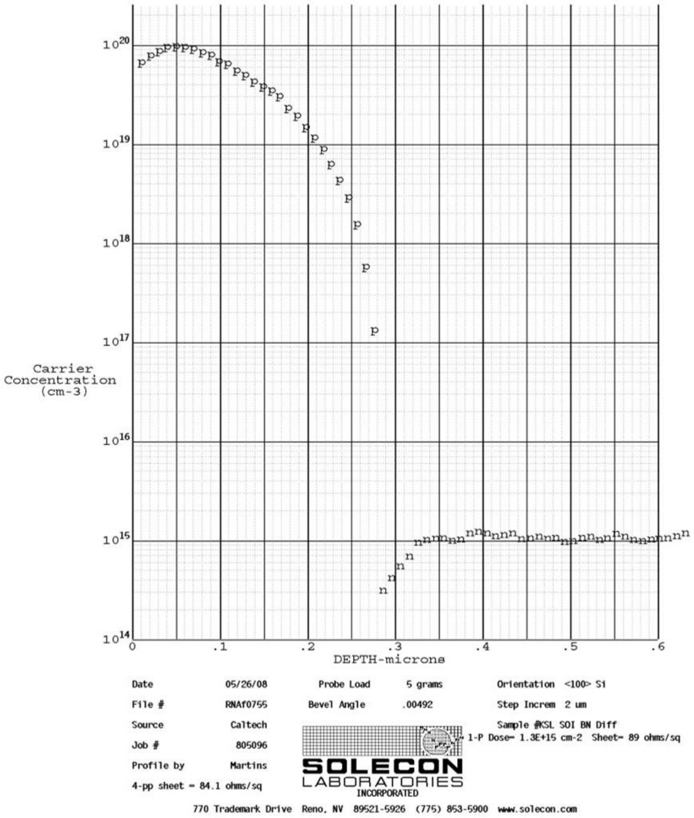

Date	05/26/08	Probe Load	5 grams	Orientation	<100> Si
File #	RNAf0755	Bevel Angle	.00492	Step Increm	2 um
Source	Caltech			Sample	#KSL SOI BN Diff
Job #	805096				1-P Dose= 1.3E+15 cm-2 Sheet= 89 ohms/sq
Profile by	Martins				

4-pp sheet = 84.1 ohms/sq

SOLECON
LABORATORIES
INCORPORATED
770 Trademark Drive Reno, NV 89521-5926 (775) 853-5900 www.solecon.com

Figure 2.17. Spreading resistance doping profile for diffusion doping of n-type device layer of SOI structure.

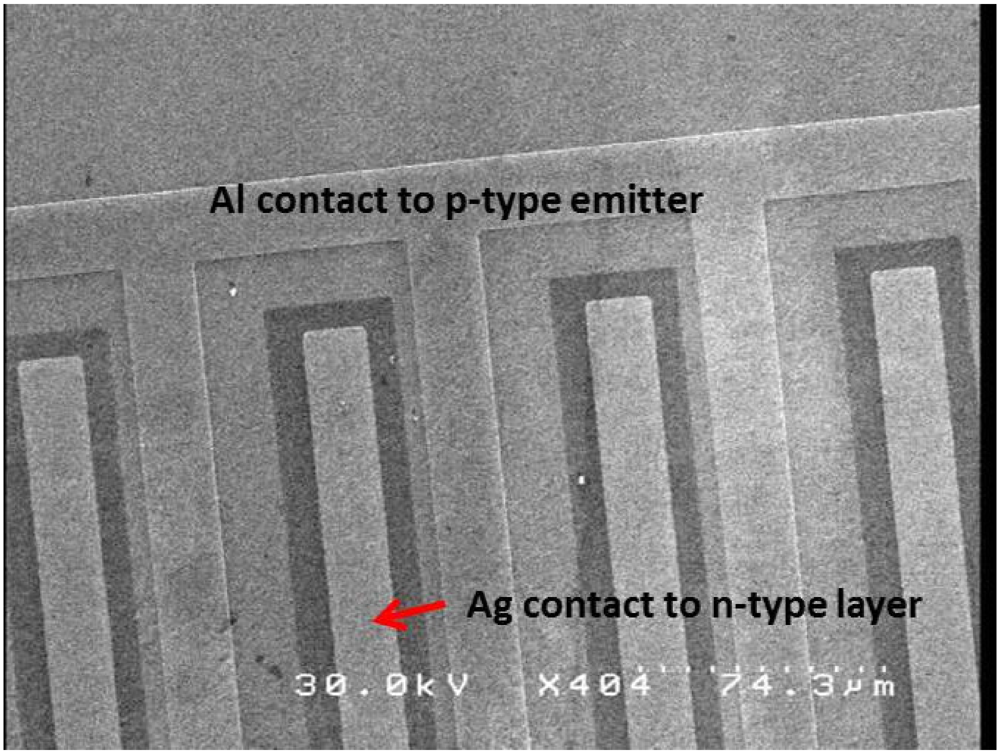

Figure 2.18. Fabricated structure with interdigitated front contacts.

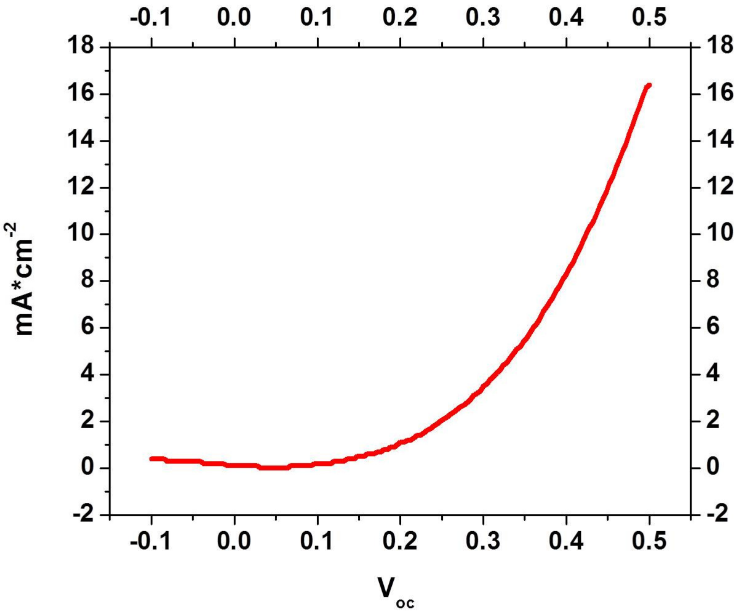

Figure 2.19. Measured I-V for fabricated structure on SOI.

from the square shape of an ideal cell is indicative of large series resistance at the metal contacts, despite the inclusion of annealing steps in contact fabrication. The low J_{sc} can be attributed both to high shading losses from the front contact structure (about 38%) and inefficient carrier collection at the contacts. The low V_{oc} could also be attributed to poor contact formation. The photolithography and subsequent etching steps require accurate alignment and etching processes, and non-uniformity in the etch or alignment across the sample will result in shunting between the device layers. While this device does exhibit diode characteristics and thus validates the general geometry of this device structure, the challenges with contact formation point to the use of a simpler structure for subsequent evaluation of electrical characteristics of these films. These complications with contact formation guided the direction of subsequent projects, and the remainder of this thesis focuses on optical characterization of silicon thin films to gain insight into potential methods for light trapping and enhanced absorption without the added complexity of contact characterization.

2.10 Prospects for HWCVD silicon films in photovoltaic devices

Due to the high growth rate and low cost of HWCVD, this method is highly attractive for use in thin film silicon solar cell fabrication. The results of this study indicate that crystalline growth can be achieved with hydrogen incorporation during growth, but the porous nature of these films may limit carrier mobility and inhibit passivation. In addition, adequate doping levels have not yet been achieved for a suitable emitter layer in a solar cell device using this deposition technique. To fully capitalize on the advantages of HWCVD, a stable means of bulk and surface passivation must be developed, accompanied by alternative means of producing a highly-doped emitter layer. The potential for large-scale utilization of this technology may lie in combining HWCVD base layers with PECVD-grown emitter layers in a vacuum cluster tool that permits subsequent layer deposition without breaking vacuum. PECVD can also be utilized to grow a-Si and SiN_x layers that can potentially act as both antireflection and passivation layers. For this reason, a PECVD chamber was added to the cluster tool, and subsequent research in this research group has been conducted to optimize deposition parameters and characterization of these materials. While the remainder of the research for this thesis did not focus on PECVD thin films, research results presented in the upcoming chapters can potentially be implemented on these thin film structures.

Chapter 3

Metal Nanoparticle Arrays for Enhanced Light-trapping

3.1 Scattering properties of metal nanoparticles

Due to the unique properties of light interaction with metal nanoparticles, much recent research has examined the effect of incorporating these nanoparticles in thin film structures to determine their effect on light scattering and capturing in thin film devices. These particles can exhibit large optical field enhancements, resulting in large enhancements in the absorption or scattering of the incoming light. The interaction of light with a metal nanoparticle causes the conducting electrons in the metal to oscillate; the collective oscillation of these electrons is defined as a plasmon and results in large optical field enhancements [54]. This phenomenon can result in either the conversion of the energy of the incident light into thermal energy via absorption or the acceleration of these electrons and subsequent radiation as scattering. Thin film solar cells can potentially benefit greatly from increased near-field enhancement associated with metal nanoparticles, and increased scattering can result in a greatly enhanced path length through the thin film by laterally redirecting incident light and increasing the fraction of light trapped in the film by total internal reflection. When the particles are placed at an interface between two materials, the light will be preferentially scattered into the materials with the higher optical density, so placing metal scattering particles on silicon will direct the scattered light into this underlying substrate due to the higher density of optical states available in the higher index material [2, 69, 79]. If the particles are small relative to the wavelength of light they can be described as point dipoles, and the interaction of these metal dipoles with incident light can be characterized by their relative scattering and absorption cross sections. The absorption cross section describes light absorbed by the particle and converted to thermal energy, while the scattering cross section accounts for the fraction of light scattered, with the total extinction cross section equal to the sum of these quantities, $C_{scat}+C_{abs}$. The mathematical expression for these cross sections was developed by Gustav Mie using Maxwell's equations to describe the behavior of electromagnetic wave radiation with a sphere [65]:

$$C_{scat} = (\frac{1}{6\pi})(\frac{2\pi}{})^4 abs(\alpha^2), \tag{3.1a}$$

$$C_{abs} = (\frac{2\pi}{\lambda})Im[\alpha], \tag{3.1b}$$

$$\alpha = 3V[(\frac{(\varepsilon_p/\varepsilon_m)-1}{(\varepsilon_p/\varepsilon_m)+2}]. \tag{3.1c}$$

[5].

To increase the light interaction with the absorbing material of a solar cell device and minimize parasitic losses to metal absorption, the scattering cross section is maximized. Since the scattering cross section increases as the square of the particle volume, we expect larger particles to be more effective scatterers, up to the limit of the diameter approaching the wavelength of light, at which point the scattering efficiency can no longer be described by using a dipole approximation. Additionally, at the surface plasmon resonance, when $E_p = 2E_m$, the scattering cross section becomes significantly larger than the physical scattering cross section of the metal particle, and large enhancements in the absorption of light at these resonant wavelengths are expected [7]. The features of this scattering and field enhancement due to surface plasmons can be tuned by varying the geometry of the nanoparticles and the array. In addition to the dependence of scattering cross section on particle diameter, variations in particle shape, distribution, and material composition have shown to effect the behavior of light interaction with a dielectric substrate, and for this reason much research has explored the development of precise and scalable fabrication of metal nanoparticle arrays[20, 87].

3.2 Metal nanoparticle array fabrication methods

Various methods for the synthesis of Ag arrays have been developed and utilized. One method is to evaporate and subsequently anneal a thin film of Ag on the substrate [68]. The annealing causes an agglomeration of Ag clusters with moderately uniform distribution, but non-uniform shape and size (Figure 3.1). Using this fabrication technique, Stuart and Hall demonstrated the use of Ag metal islands to couple into waveguide modes of a 165nm-thick silicon photodetector, with photocurrent enhancements of over 18 observed at the resonant wavelength and an overall enhancement over a large portion of the spectrum[80]. Pillai, et al., reported a 19 % enhancement

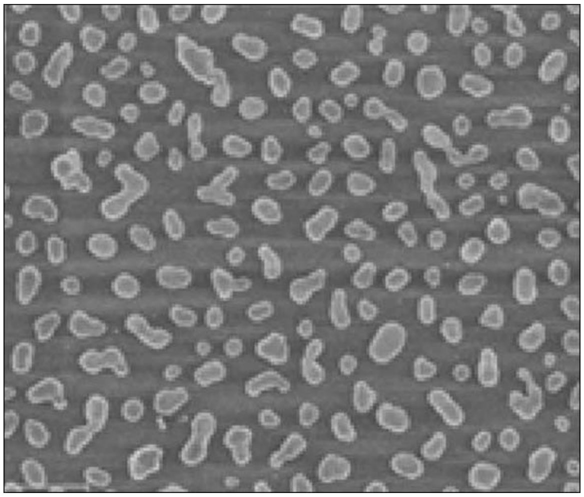

Figure 3.1. Distribution of Ag clusters after thermal annealing [68].

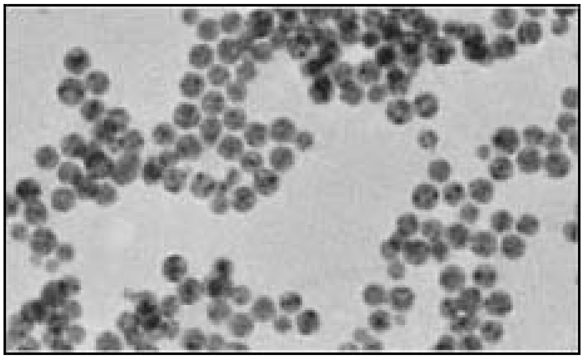

Figure 3.2. Distribution of colloidal suspension of Ag particles [48].

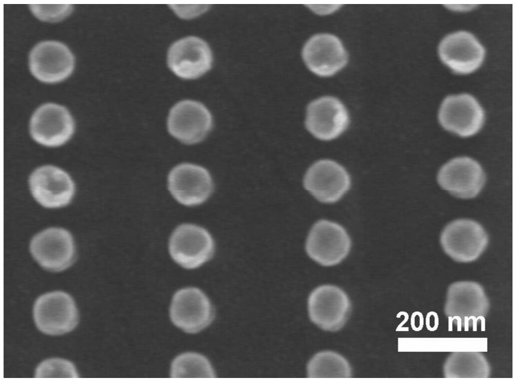

Figure 3.3. Array of metal nanoparticles fabricated with e-beam lithography [92].

in photocurrent with the addition of Ag metal islands on a wafer-based silicon device and a 33% enhancement for a 1.25um-thick SOI structure [33]. A second method for metal nanoparticle array fabrication is the deposition of a colloidal suspension of Ag nanoparticles in a monolayer on the substrate, resulting in an array with uniform diameters but non-uniform pitch (Figure 3.2)[48].

While both of these methods are easily scalable, annealing does not allow precise control over particle diameter, while the dispersion of a colloidal suspension does not permit accurate manipulation of interparticel spacing; to realize the full potential of light trapping with metal nanoparticles, precise control of array geometry is necessary. To simultaneously control both the size of the particles and pitch of the array, e-beam lithography has been employed to fabricate regular nanoparticles arrays of various metals (Figure 3.3)[92]. This method permits a large degree control, but is impractical to use over large areas; to address these challenges in array fabrication, a templating method has been developed that achieves both uniform diameter and pitch over large areas; these parameters can be controllably varied over a large parameter space for optimization of array geometry to maximize light scattering and trapping.

3.3 Anodic aluminum oxide templates for metal nanoparticle fabrication

Anodizing aluminum in an acidic solution results in the formation of a regular array of pores separated from the aluminum substrate by a thin oxide membrane at the bottom of these pores. This regular hexagonal array forms as a result of repulsive forces between neighboring pores as the aluminum is oxidized, and the resulting structure can be used as a template for fabricating regular arrays of nanoscale structure [13, 62, 63, 82]. The parameters of these arrays can be controlled by the pH of the solution and the voltage used during anodization, and templates with controllably varied pitch and diameter have been fabricated with this technique [45, 84]. A through-hole membrane can be fabricated by anodizing and subsequent etching steps, and these membranes can then be utilized as a template through which metal can evaporated to produce regular arrays of nanoparticles. This anodization process has a long history in industry. The porous nature of anodic oxide coatings and their formation was first discussed in the 1940s, and the anodization of aluminum has been practiced on an industrial scale as both an aesthetic enhancement and a corrosion preventative since 1923 [12, 75]. The self-regulating nature of the array of pores observed was explained by a model in 1970 based on the electric field variation in the pores, introducing the concept that pores initially form due to irregularities in the substrate [67]. The electric field increases in the thinner regions, and pores reshape themselves until equilibrium is reached. The pores change in number and diameter to form a steady state between the increased oxide growth that accompanies the increased e-field and the increased dissolution rate that occurs with thicker oxides. Su, et al., propose a mechanism for the subsequent growth of the pores into a regular, close-packed array using a steady-state model. The rate of dissolution of the Al_2O_3 is balanced by an increased rate of oxide growth: a thick oxide will be reduced rapidly by this reaction until it is thin enough that the increased electric field across the thin oxide membrane causes an increase in the oxide growth rate. In this manner a constant oxide thickness is achieved through this equilibrium [81]. The equilibration of the oxide layer thickness applies also to the oxide between the pores, and they consequently impinge on each other to a constant interpore distance, which is accommodated by a close-packed, hexagonal array. This steady state oxide thickness, as well as the pore diameter, is observed to be in direct correlation to the anodization voltage, presenting a method for control of the array geometry through anodization conditions. Keller, Hunter, and Robinson demonstrated the parallel nature of these pores in 1953 in a close-packed hexagonal structure [50]. Masuda, et al., first used these self-organized templates to fabricate a through-hole membrane through which metal could be evaporated to form ordered arrays [62]. By using this technique, large arrays ($>10\mu$m) of Ag nanoparticles were fabricated with varying pitch, allowing the optimization of array distribution for maximum light capturing in a thin film silicon substrate.

3.4 Experimental procedure for AAO template fabrication

By varying the voltage and anodizing solution, previous work in this research group has demonstrated successful fabrication of membranes and corresponding metal nanoparticle arrays with interpore distances of 50nm to 200nm. An example of these varying array distributions is presented in Figure 3.4. Using this procedure as a guide, through-hole membranes were fabricated for Ag nanoparticle array fabrication on SOI structures for electrical and optical characterization in the method outlined in Figure **??**.

Following the procedure detailed by Nakayama, et al., 99.9999% grade aluminum sheets were first degreased in acetone in an ultrasonic bath for 5 minutes [84]. The sheets were then electropolished to flatten the surface in a solution of H_2O (80mL), H_3PO_4 (330mL), H_2SO_4 (75mL), and ethylene glycol (15mL). Using the Al sheet as the anode and a glassy carbon sheet for a cathode, the solution was heated to 70 $\circ$C and 20V-30V was applied to maintain a constant current density of 250mA/cm^2 for

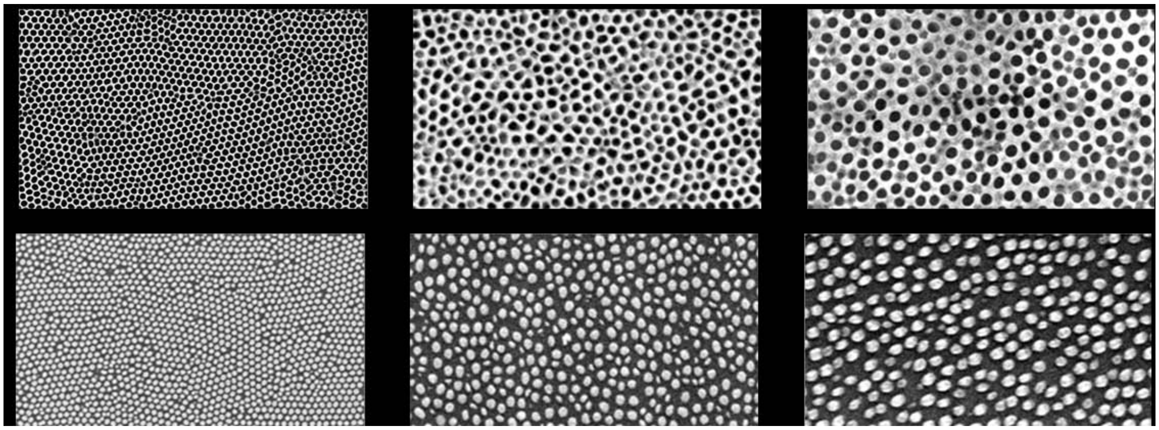

Figure 3.4. SEM micrograph of variation of AAO membrane pitch with resulting metal nanoparticle arrays [84].

5 minutes. The sheets were then rinsed in H_2O and acetone. To prevent bubbles from forming on the Al and causing surface roughness, it is important to refrain from stirring during this electropolishing step and to periodically lightly tap the Al sheet to remove any bubbles forming on the surface. In order to make templates with the highest order patterning, two separate anodization steps are necessary. The first anodization step initializes the pores and dictates the pore-spacing of the resulting template, but may be disordered due to surface irregularities. After the first anodization step, this disorder can be removed via etching, and the subsequent anodization step results in a regular, ordered array. The anodization solution can determine array features, depending on the pH of the electrolyte and the voltage applied during anodization. A mixture of 0.3M/L oxalic and malonic acids was used with an applied voltage of 60V-100V, and the anodization was performed in an ice bath, keeping the temperature below 15 °C under constant voltage. The length of anodization time varies depending on the voltage used, but does not give evidence of being a highly critical parameter. This anodization step was performed for 1-2 hours. Next, the oxide layer formed during this anodization step was selectively etched using a solution of chromic and phosphoric acid (6g CrO_3, 20g H_3PO_4, 300gH_2O) heated to 50 °C and immersing the aluminum sample for several (>4) hours. The resulting structure is that of regularly ordered pits on the surface of the aluminum. The second anodization step is more critical, as the length of time of this step will determine the resulting

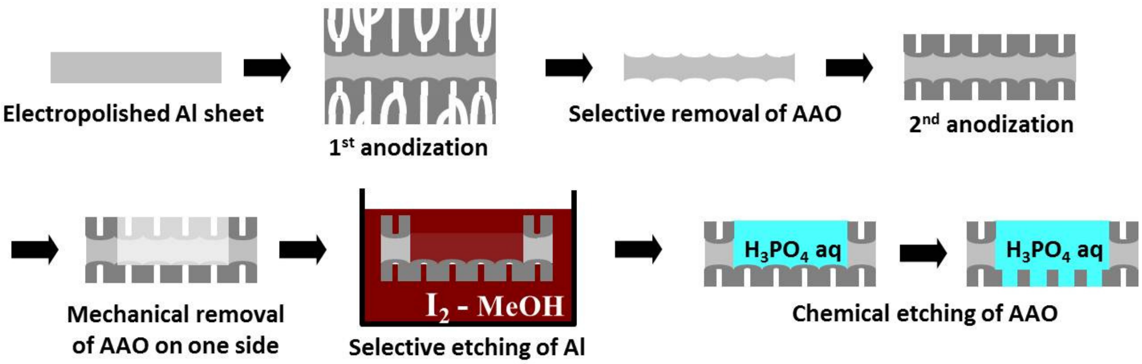

Figure 3.5. Fabrication steps for AAO template fabrication [84].

thickness of the template. Using the same solution used for the first anodization, and using a voltage of 80V, the second anodization was conducted for a total of 4 minutes, which resulted in approximately 500nm-thick AAO membranes. After this step the bottom of the pores was accessed to obtain a through-hole membrane. This was accomplished by mechanically removing the back side of the AAO sheet; clear nailpolish was applied to the front side for protection during this step, and a box cutter blade was used to remove the layer of oxide on the back. Left with bare Al on the back of the sheet, the remaining material can be chemically etched to the bottom of the pores using a solution of iodine and methanol (15g iodine, 15g methanol) for approximately one hour. Since this etching reaction is exothermic, the solution will bubble and heat up as the aluminum is removed. When the solution begins to return to room temperature, this indicates that the etching is complete. Acetone is then used to remove the nailpolish protective layer. The pores in the resulting membrane are still closed at the bottom at this point, as illustrated in Figure 3.6. To remove this layer, the back side of the membrane is coated with nailpolish, which results in

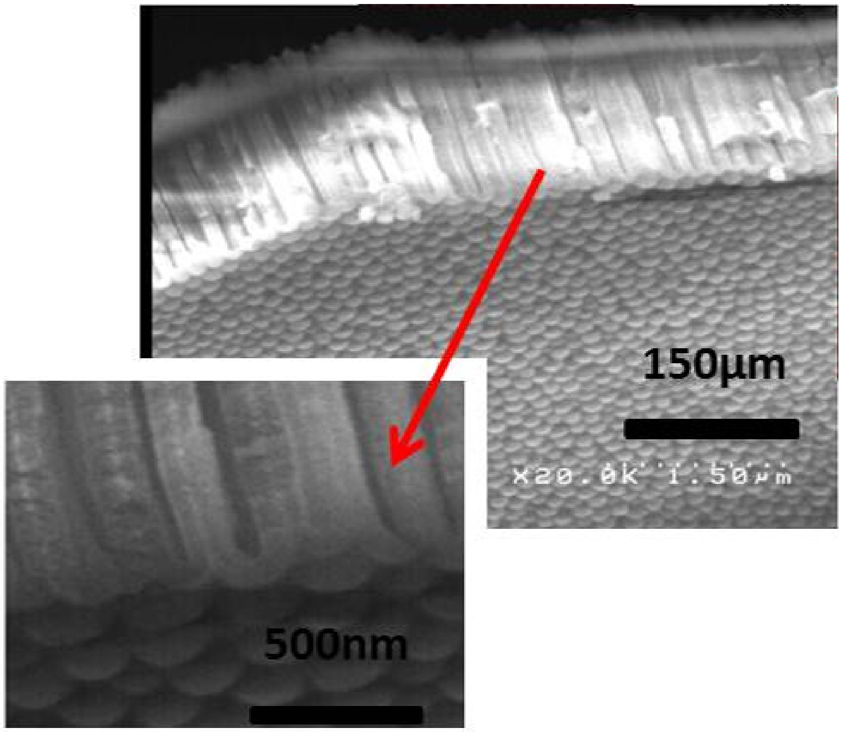

Figure 3.6. Porous membrane resulting from AAO process prior to through-hole etch.

.

a hydrophobic surface. Using a 30 °C water bath, the membrane is placed on a flat surface in this heated environment, and a 1/20 H_3PO_4-aq mixture is deposited with a dropper onto the top side of the membrane. Since this step will not only etch through the bottom of the pores but will also widen these pores, the etch time is critical. The minimum time for complete removal of the pore bottoms is 70 minutes for templates used in this study. Adhesion between the membrane and substrate was accomplished by floating the porous membrane onto the substrate with water, then wicking the water away until contact is made between the membrane and the SOI. The result is a completely porous template through which nanoparticle material can be thermally evaporated (Figure 3.7), and in this study 150nm of Ag was evaporated at a rate of approximately 10$\AA$/s.

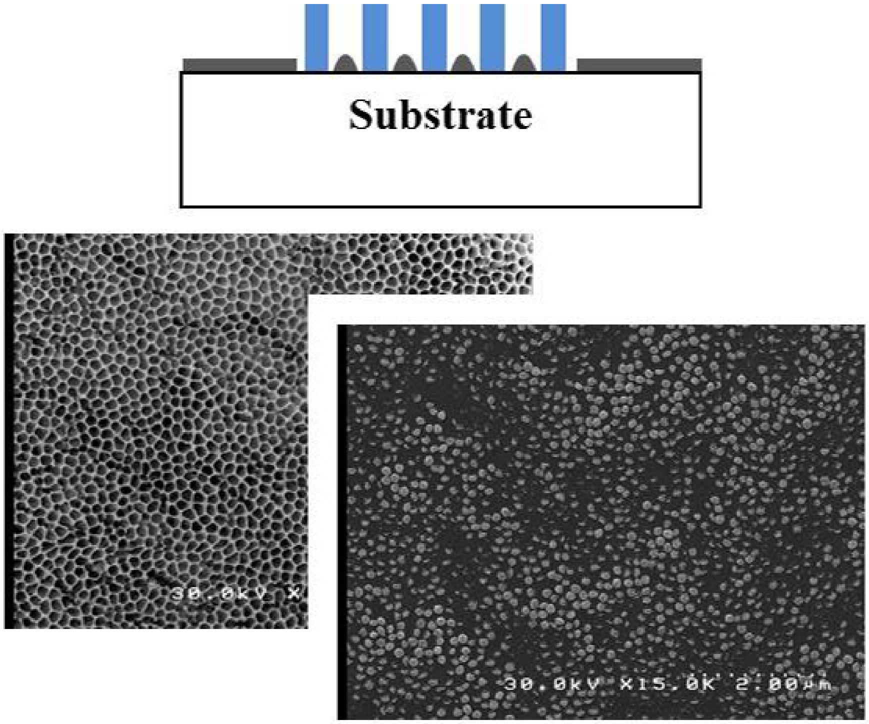

Figure 3.7. Schematic of porous AAO template as evaporation mask, with SEM micrographs of membrane and resulting nanoparticle array.

The thickness of the material evaporated will determine the height of the nanoparticle array and is limited by the thickness of the membrane used. An important consideration when conducting the evaporation step is the directional dependence of the evaporation species. If the substrate is not placed directly above the source, shadowing of the pores will take place and deposition may not reach the substrate at the bottom of the pores.

3.5 Control of array parameters

The geometry of these metal nanoparticle arrays can be controllably varied by modifying appropriate fabrication steps. The pitch is predominantly determined by the anodization voltage used. Nakayama observed a pitch range of 63nm to 300nm for a voltage range of 25V to 120V [84]. This linear increase in pore spacing with forming voltage has also been observed in previous studies, and permits a systematic variation of the pitch of the nanoparticle array[50]. Keeping the anodization voltage constant but varying the through-hole phosphoric acid etch time allows for changing the diameter of the nanoparticles keeping a constant pitch. Additionally, the aspect ratio can be increased by increasing the metal evaporation thickness through the AAO membrane. Armed with a close control of pitch, diameter, and aspect ratio, any metal nanoparticle array can be optimized to match the performance requirements of our device. In the case of this study the goal is to maximize photocurrent in 220nm-thick Si layers. To assist in determining the optimal array properties, electromagnetic simulations were conducted to guide subsequent fabrication.

3.6 FDTD simulations

To optimize the metal nanoparticle array geometry, full-field electromagnetic simulations of SOI structures decorated by metal nanoparticle arrays were employed to predict and optimize the field enhancement and light trapping attributable to the Ag nanoparticle arrays on the surface of 220nm-thick Si. Using commercially available Lumerical software, a finite-difference time domain (FDTD) algorithm was utilized to determine the electromagnetic field characteristics resulting from light interaction with these arrays on thin film structures. This method uses Maxwells equations, specifically the derivative expressions, to solve for the EM field at discrete space and time intervals to determine the field profile in the simulated structure. These derivative equations are known as Amperes Law and Faradays Law and are expressed, respectively, as:

$$\nabla x B = \frac{J}{\varepsilon c^2} + \frac{1}{c^2}\frac{\delta E}{\delta t}, \tag{3.2a}$$

$$\nabla x E = \frac{-\mu \delta B}{\delta t}. \tag{3.2b}$$

J is the electric current density, B and E are the magnetic and electric field intensities, and μ and ε are the permeability and permittivity of the medium through which the light is travelling. These equations yield the following expressions:

$$-\mu\frac{\delta H}{\delta t} = -\hat{a}_y\frac{\delta E_z}{\delta x}, \tag{3.3a}$$

$$\varepsilon\frac{\delta E}{\delta t} = \hat{a}_z\frac{\delta H_y}{\delta x}. \tag{3.3b}$$

These finite difference expressions describe the time variance of the B-field in terms of the space derivative of the E-field and the time variance of the E-field in terms of the space derivative of the B-field. The FDTD algorithm approximates these differential equations by solving at finite increments. The spatial derivative of a function, for example, can be approximated by equation (3.4):

$$\left.\frac{df(x)}{dx}\right|_{x=x_0} \approx \frac{f(x_0+\frac{\delta}{2}) - f(x_0+\frac{\delta}{2})}{\delta} \tag{3.4}$$

This approximation is then applied to a simulation environment that has been both spatially and temporally discretized. The FDTD algorithm alternately solves each of these equations at discrete time steps and uses the resulting solution as input for the other equation, thus proceeding through the requisite number of time steps in a leap frog fashion. The advantage of this simulation method is that it is a numerical algorithm that can be applied to a wide variety of geometries and can be used to describe

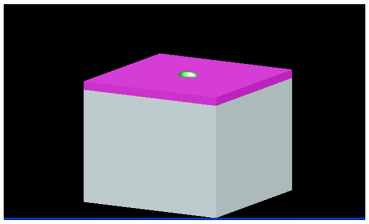

Figure 3.8. Device structure used in FDTD simulations.

behavior of non-linear and dispersive materials, while the primary limitations include numerical dispersion and instability resulting from the finite nature of the calculated solutions to Maxwells equations. In addition, simulations of larger structures using a reasonable mesh size require a large amount of computing resources and time to achieve sufficient accuracy. The basic simulation structure used for this study is a SOI wafer with a 220nm-thick silicon device layer on 3μm silicon dioxide. Periodic arrays of silver nanostructures on the surface structure were simulated by defining a unit cell and applying periodic boundary conditions in the x and y directions, with perfectly-matched-layer (PML) conditions applied in the z-direction. Previously measured n and k data acquired via ellipsometry were used to define the metal and dielectric materials in this structure. A monitor of power flux was placed above the surface to record reflectivity data, and an additional power monitor was placed below the film to determine the net absorption in the 220nm of silicon. By subtracting the reflected light and the light lost through the rear interface of the 220nm device layer, a maximum achievable external quantum efficiency (EQE) was calculated for this device structure. This calculated EQE is the probability that an incident photon will be absorbed; the internal electrical effects, such as recombination, and contact features, are not taken into account in this model, so this calculation represents a maximum possible EQE for each type of structure. This number assumes that each photon absorbed generates one carrier and that all carriers are collected as photocurrent, which is a reasonable assumption since the minority carrier diffusion length in the crystalline silicon film exceeds its thickness. An optical generation rate was also calculated using this same assumption by integrating over the dielectric absorber layer at discrete wavelengths:

$$G_{opt} = \frac{1}{2\hbar\omega}\mathbf{re}(\tilde{\nabla}\cdot\tilde{\mathbf{P}}) = \frac{\varepsilon''|\mathbf{E^2}|}{\mathbf{2\hbar}}\mathbf{cm^{-3}s^{-1}}. \tag{3.5}$$

The optical generation rate and the EQE calculations were then used as a guide to determine the optimal structure for light trapping.

3.7 Simulation model

The fabrication method for these arrays allows a high degree of control over the pitch, aspect ratio, and particle diameter. To explore this large parameter space, periodic arrays were modeled with varying pitch and diameter to acquire insight into the scattering behavior of individual and interacting particles. A hemispherical structure was chosen both to most accurately represent the fabricated structure, but also to reflect the particle geometry that is expected to be most effective based on previous studies that have demonstrated an increase in scattering to the underlying substrate with decreasing integrated distance between the scattering feature and the substrate [7]. To economize simulation time, a regular square array was built by defining periodic boundary conditions in the x-y plane.

3.8 Simulation results: 200nm pitch, varying diameter

Simulations with a constant 200nm pitch and a changing diameter reveal the influence of particle proximity on the location of field enhancement in the silicon film. For particles separated by a distance greater than 10s of nanometers, the influence they have on each other will be dictated by the interference of the scattered waves from each particle. However, for particles impinging on one another, the near-field enhancement of each particle resulting from the plasmon excitation will interact with the near-field of the adjacent particle [14, 60, 88]. As the particle diameter is increased while maintaining a constant pitch, the distance between the circumference of the hemispheres decreases and near-field effects are expected. A mapping of the optical generation rate from these simulations reveals enhancement peaks centered at wavelengths of 505nm, 590nm, and 690nm (Figure 3.9). The location of these peaks is constant across the simulated spectrum and can therefore be attributed to the periodic modes of a 200nm pitch array. The intensity and width of these peaks varies across the spectrum, however. The peaks are broad with lower amplitudes for smaller diameters, but gain in intensity and narrow in bandwidth as the diameter increases. The spectral location of the enhancement remains constant with sharply increasing amplitude due to this near-field interaction between the particles. An increase in diameter with constant pitch corresponds to increased proximity between metal particles; this increased proximity increases the interaction between the Ag hemispheres

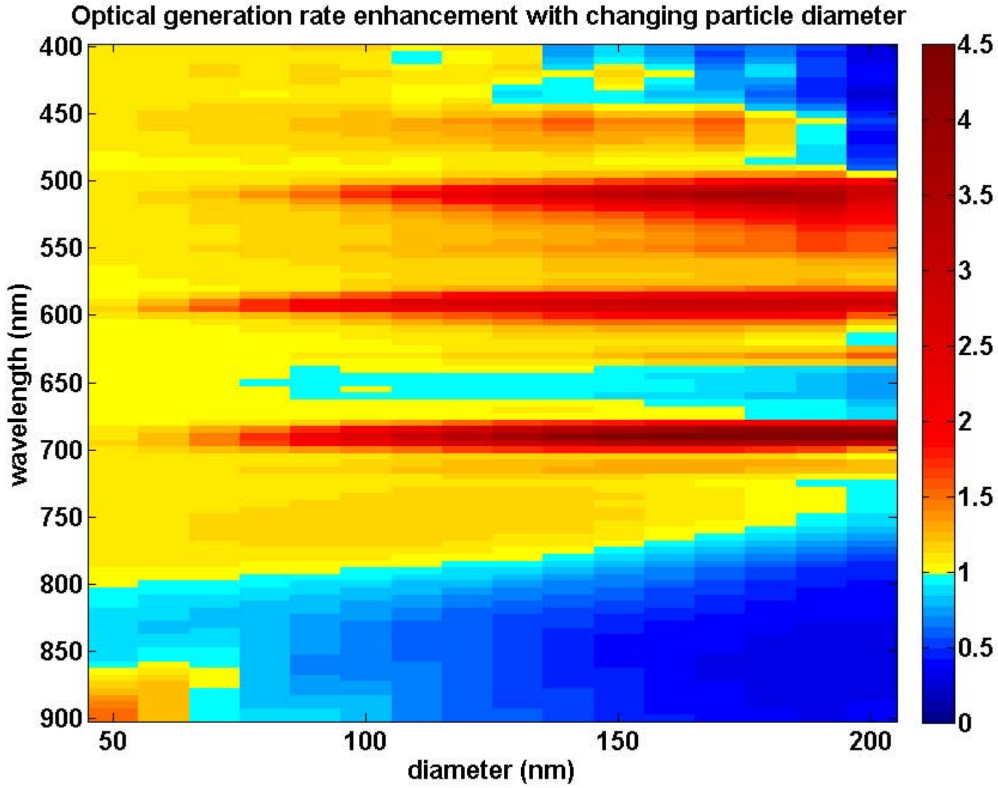

Figure 3.9. Simulated optical generation rate enhancement with changing particle diameter.

and intensifies the effect of the resonance from the periodic Bloch modes. In addition, the increased diameter corresponds to a larger effective scattering cross section with less parasitic absorption in the metal. Figure 3.10 illustrates the light trapping behavior at one of these peak wavelengths, λ=690nm, by mapping a cross section of the light intensity in the simulated device. This plot compares the pattern of light trapping for a 50nm diameter particle with that of a 200nm diameter particle. The light is localized in the same pattern for both diameters, but, as evidenced by the scale bar, the enhancement is significantly higher for the larger diameter. This substantial increase in light absorption occurs in spite of almost full metal coverage of the surface, illustrating the significant influence of increased effective scattering cross section in preferentially redirecting incident light into silicon substrates.

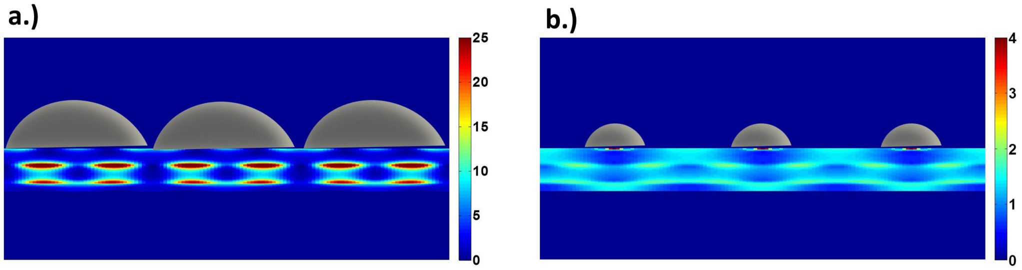

Figure 3.10. Cross sectional view of light trapping patterns in arrays of a.) 50nm diameter and b.) 200nm diameter Ag hemispheres.

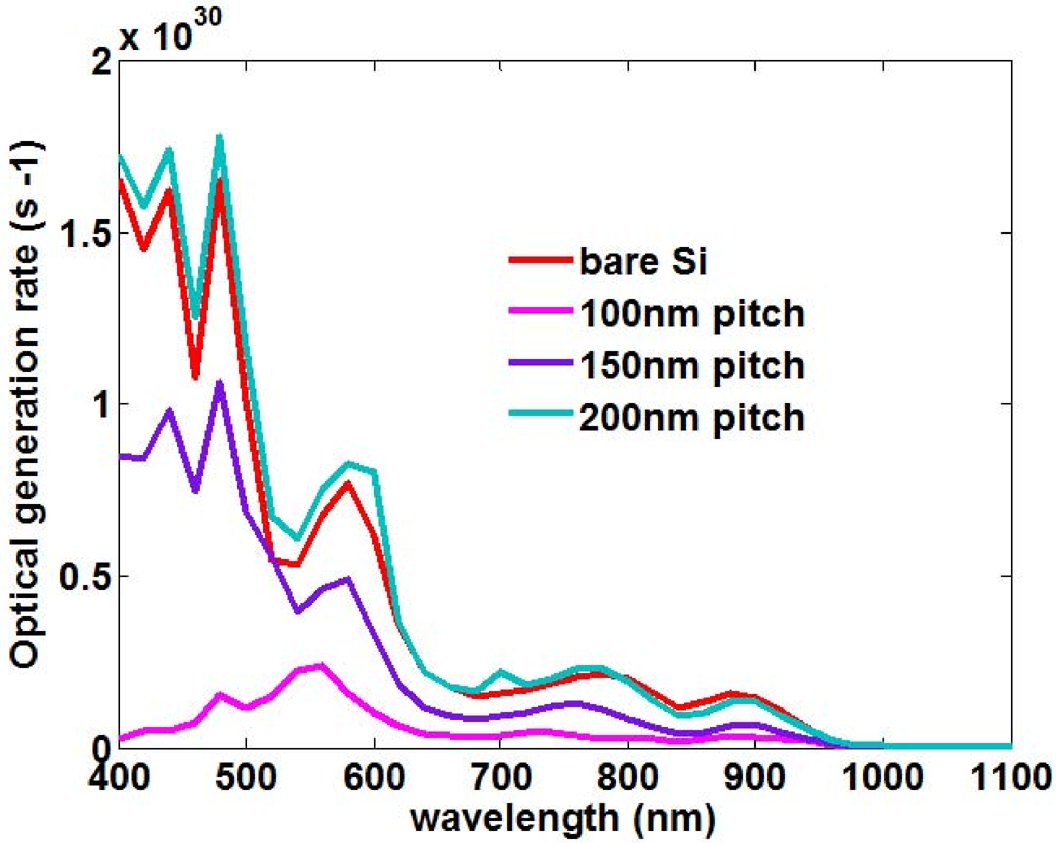

Figure 3.11. Simulated optical generation rate with metal nanoparticle array pitch. A pitch less than 200nm yields less light absorption than flat silicon

3.9 Pitch variation with periodic Ag arrays

Further enhancements may be possible by varying other array parameters, and for solar cell devices the spectral location of the enhancement must also be considered. An ideal enhancement peak will be located in a high-power portion of the solar spectrum to efficiently utilize the enhancement effect. Since the wavelength-dependence of this light absorption enhancement depends greatly on pitch, this parameter was varied in FDTD simulations to optimize to overall integrated optical generation rate enhancement. The calculation results for the optical generation rate of an array with varying pitch and particles with 100nm diameter are plotted in Figure 3.11 for comparison with a flat 220nm silicon layer and exhibit a significant enhancement in optical generation rate for sparser arrays with pitch 200nm. While a 200nm pitch Ag array shows an optical generation rate greater than that of a flat silicon layer over almost the entire spectrum of interest, an array with a smaller pitch shows progressively less absorption, an effect that is more pronounced at short wavelengths. This effect can be attributed to the increase in metal coverage as the pitch is decreased, resulting in an increase in reflectivity. These results prompted a more detailed investigation of the influence of pitch, and further simulations examined a wider pitch range from 200nm to 400nm. Figure 3.12 plots the results of EQE calculations at each simulated wavelength and pitch. The interaction of scattered fields from a regular array of nanoparticles produces an interference pattern that is dependent on the spacing between the particles. The resulting linearly shifting peak enhancement with pitch is attributed to the constructive interference from this interaction, referred to as Bloch modes due to their periodic nature. The existence of these periodic modes permits tuning of the location of the peak enhancements to optimize light harvesting in a thin film structure by changing the pitch of the array. The emergence of these modes is

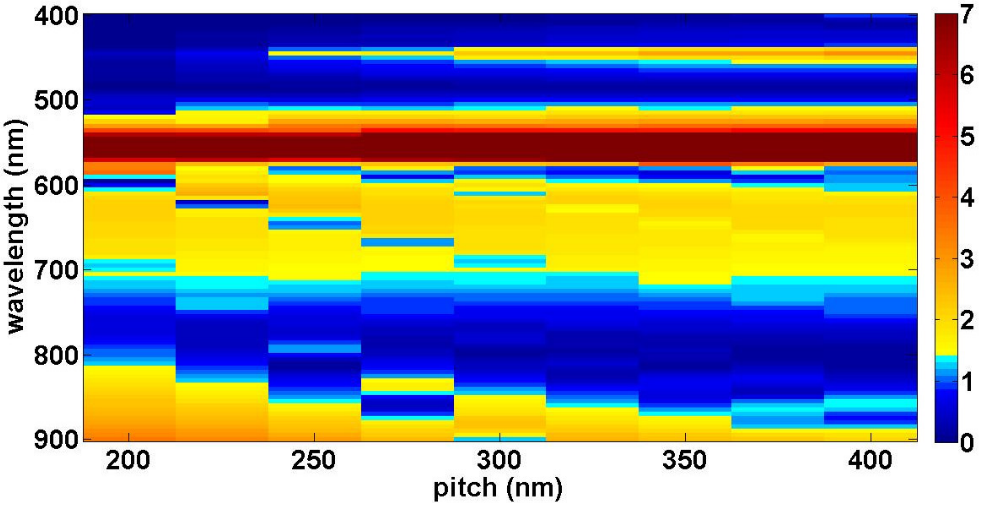

Figure 3.12. Simulated optical generation rate enhancement with changing pitch of Ag nanoparticle array.

exhibited as the pitch exceeds 200nm, indicating the shift from the near-field coupling to far-field scattering interference. Additional simulations have exhibited these same periodic modes to be present for all diameters, though the effect is most significant at diameters of 150nm due to the large effective cross section at this diameter.

3.10 Aspect ratio variation

The aspect ratio of these structures was also varied to determine the effect of this parameter on light scattering. Previous studies have concluded that increased overall proximity of the metal nanoparticle to the substrate will result in a decrease in effective cross section due to the interference between the incident and scattered waves [7]. However, increased coupling can also be expected with increased proximity to the substrate. For this reason a lower aspect ratio is expected to show increased scattering into a silicon thin film, but the presence of a wavelength-dependent modulation is also anticipated due to the change in effective cross section due to the interference near the interface. FDTD simulations of these structures confirm this expectation by showing a shift of our generation rate peaks to longer wavelengths and oscillatory behaviour of these peaks.

3.11 Summary of simulation results

These optical generation rate calculations show that smaller particles with smaller pitch demonstrate a decrease in performance over much of the spectrum range, but remarkably the largest enhancement is exhibited by dense arrays where the Ag particles are impinging on each other, despite the large fraction of metal coverage with this array geometry. At longer wavelengths, greater enhancement is exhibited with smaller diameters, with only 50nm diameter particles exceeding the performance of bare silicon; at these longer wavelengths there is little coupling into metal, and consequently less scattering. In this wavelength range the increase in reflection from the metal coverage dominates and decreases absorption for increased particle size.

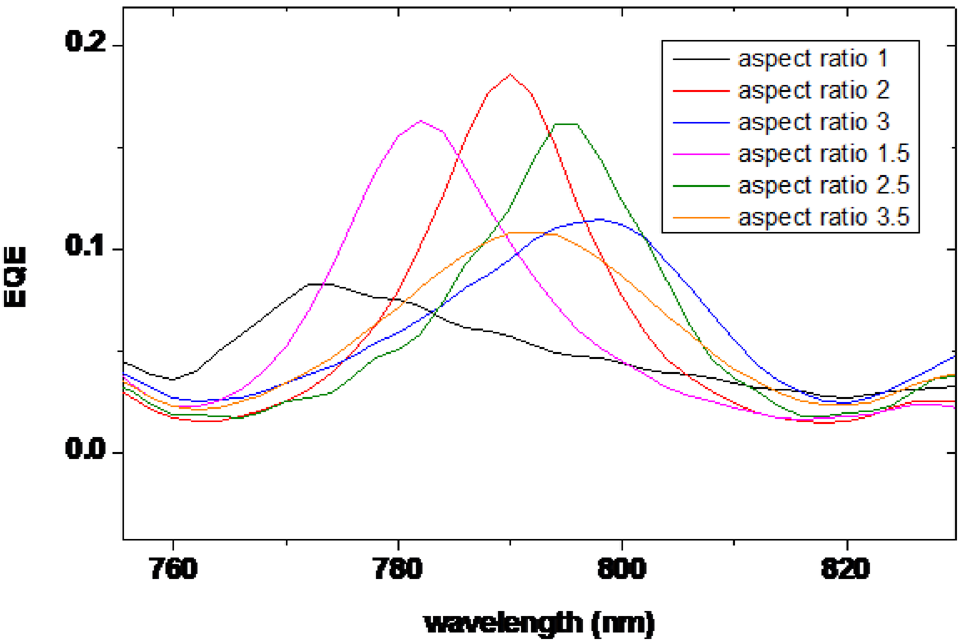

Figure 3.13. Simulated optical generation rate with changing aspect ratio of Ag hemispheres.

3.12 Photoconductivity measurements

Two-point dark and light I-V measurements were performed both before and after nanoparticle deposition to determine any change in the photoconductivity resulting from the influence of a nanoparticle array. To prepare devices for electrical measurements, aluminum pads were thermally evaporated with a separation of 1 cm on the SOI structures and contacted with fine-tip probes. Contact formation was performed before nanoparticle deposition. These measurements revealed an increase in overall photoconductivity with Ag nanoparticle arrays, and the change in conductivity corresponds to over a ten-fold increase in photogenerated carriers (Figure 3.15).

In order to examine the portion of the spectrum causing this increase in photoconductivity, the wavelength-resolved spectral response of these devices was measured. A xenon lamp was used as a white light source and sent through a monochromator, and an optical chopper wheel and a lock-in amplifier were used in tandem to improve the signal-to-noise ratio. The resulting single-wavelength light then illuminates the

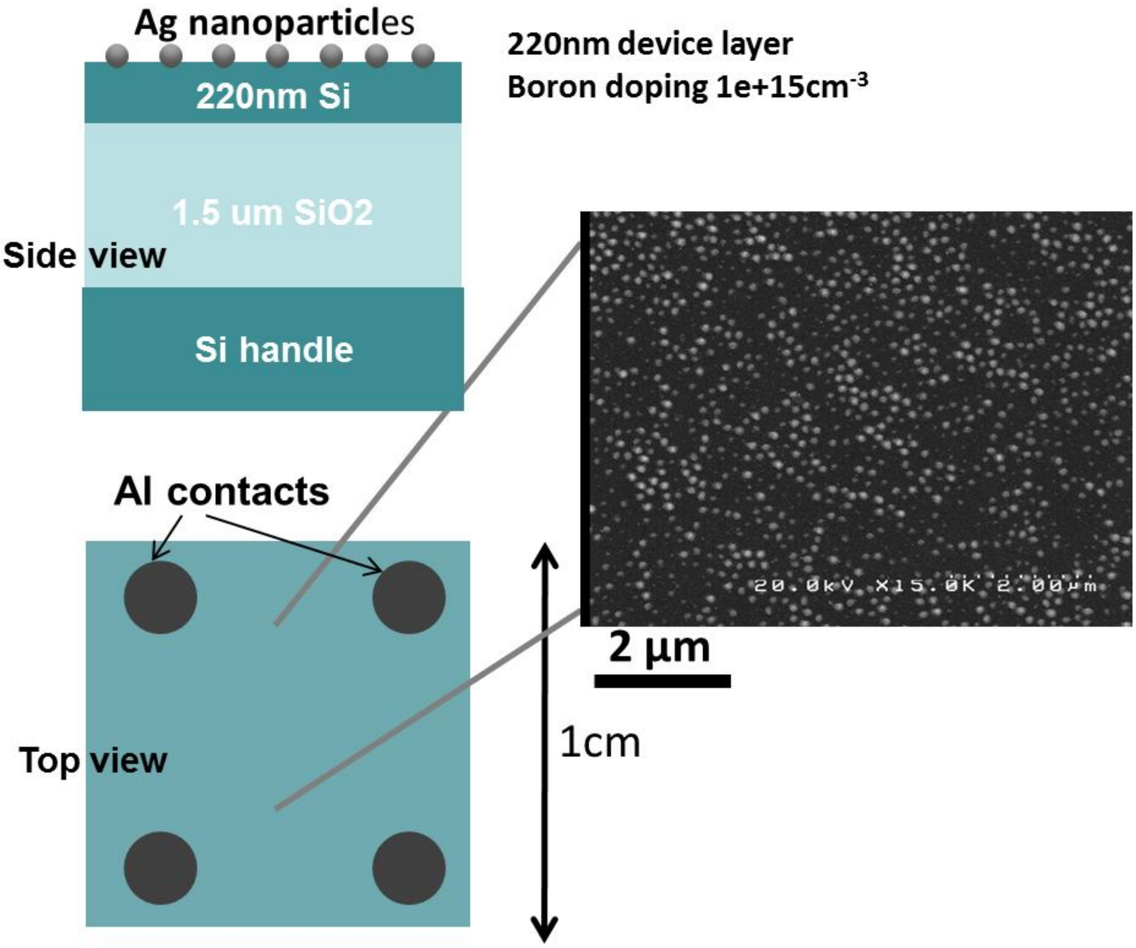

Figure 3.14. Fabricated structure with schematic showing contact layout.

sample. To allow carrier collection, a 0.5 volt bias was applied across the contacts and the device current was measured at each discrete wavelength, normalizing by the power output at each wavelength.

3.13 Measurement results

Wavelength-resolved spectral response measurements reveal an increase in performance with an array of Ag nanoparticles with a 300nm pitch, corresponding to 120V anodization, but a decrease in photogenerated carriers is observed for smaller diameter and pitch (Figure 2.13). This correlates well with initial predictions based on the

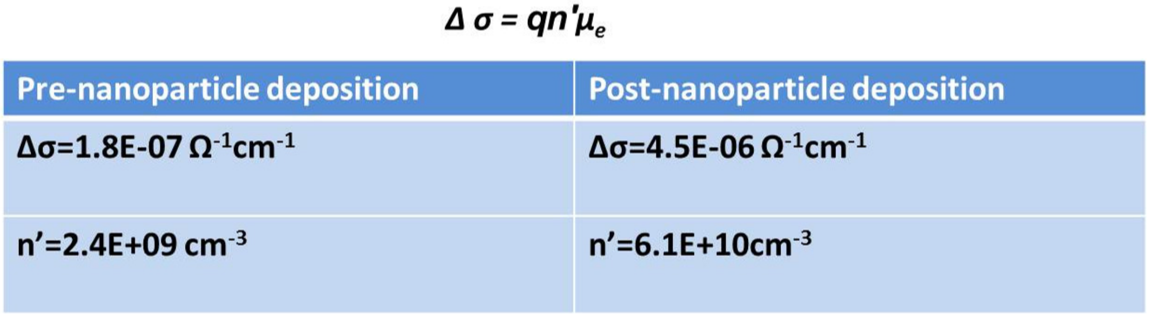

$$\Delta\,\sigma = qn'\mu_e$$

Pre-nanoparticle deposition	Post-nanoparticle deposition
$\Delta\sigma$=1.8E-07 Ω^{-1}cm^{-1}	$\Delta\sigma$=4.5E-06 Ω^{-1}cm^{-1}
n'=2.4E+09 cm^{-3}	n'=6.1E+10cm^{-3}

Figure 3.15. Measured photoconductivity comparison with and without Ag nanoparticle arrays; Ag arrays result in a > 10-fold increase in photogenerated carriers.

Mie approximation presented at the beginning of this chapter, as well as with simulation results showing optimal light trapping with larger diameter and pitch. Peaks in spectral response enhancement are observed around wavelengths of λ=620nm, 780nm, 820nm, and 880nm, with little enhancement observed at shorter wavelengths due to increased reflectivity at these wavelengths, as observed in simulation results. Figure 3.17 compares these peaks to full-field simulation results, and good agreement exists between measurement and calculation of the spectral location of these enhancement peaks. However, additional peaks are observed in these simulation results that are not present in the spectral response measurements. The additional peaks observed at $\lambda\sim$680nm and 780nm in the simulation may be a consequence of additional periodic modes that, due to the decreased uniformity and presence of irregularities in the actual fabricated sample, may not be represented fully in the measured spectral response of our sample.

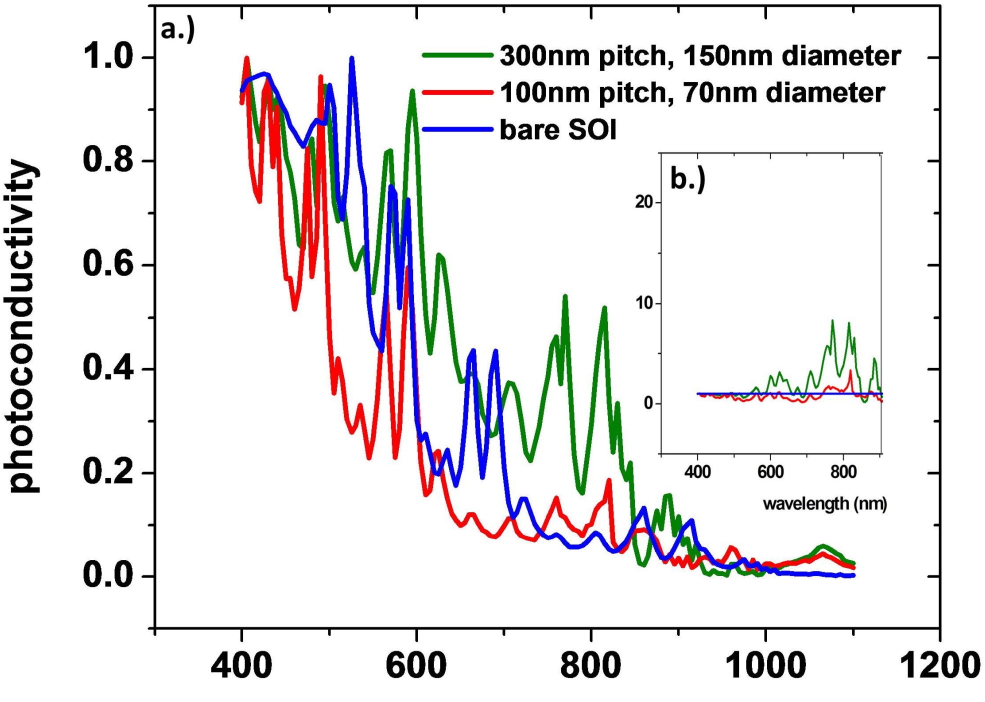

Figure 3.16. a.) Spectral response measurement comparison with and without Ag nanoparticle arrays. b.) Spectral response enhancement over flat SOI.

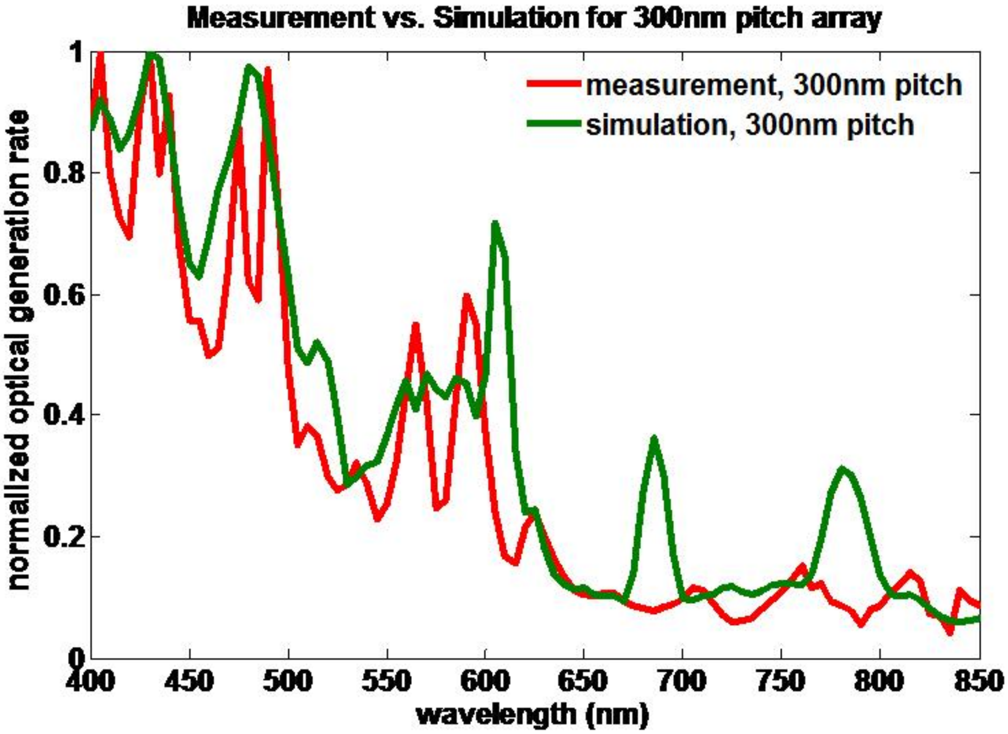

Figure 3.17. Comparison of simulated and measured spectral response for 300nm pitch Ag nanoparticle array.

3.14 Summary of light-trapping features with Ag nanoparticle arrays

The results of full-field electromagnetic simulations of regular arrays of Ag nanoparticles on a thin film silicon structure exhibit tunable enhancement peaks in optical generation rates that vary with pitch and particle diameter. The wavelength at which these enhancement peaks are centered is controlled by the array pitch, while the amplitude and bandwidth of this peak is dictated by the diameter of the Ag nanoparticles. These models demonstrate the ability to optimize array geometry to maximize light trapping in the underlying thin-film silicon layer. A method for fabricating regular arrays of metal nanoparticles is demonstrated using AAO membranes as templates for thermal evaporation, and this technique allows control of both the pitch and diameter of the particles. This templating technique is therefore a viable method for realizing a structure optimized for light trapping. Ag arrays were fabricated on SOI structures with 220nm-thick Si device layers, and spectral response measurements confirm the enhancement in photocurrent with metal nanoparticle arrays. The results of this study demonstrate the potential for increased light trapping in solar cells by incorporating metal nanoparticle arrays on the surface, and a viable method for fabricating such arrays in a post-processing step has been successfully demonstrated.

Chapter 4

Dielectric Surface Textures for Enhanced Light Trapping

4.1 Theoretical potential for light absorption in thin-film structures

Arrays of metal nanoparticles have demonstrated enhanced photocurrent generation due to their plasmonic properties and increased effective scattering cross section [7, 29]. However, the performance of these types of devices is restricted by the losses due to light absorption in the metal and increased reflection at the surface from metal coverage. An alternate technique for engineering structures that maximize light trapping in sub-micron silicon films is to exploit the scattering mechanisms of dielectric arrays on the surface of the absorbing material. The scattering properties of these arrays are determined by the geometry and material properties of the surface features, and by changing the size, pitch, and shape of these arrays, the light scattered into the film and absorbed can be maximized. In the ray optics limit, Yablonovitch, et al., assumed idealized scattering conditions and combined geometrical and statistical optics to calculate a maximum optical absorption enhancement in weakly absorbing thin films [90]. Assuming a perfect back reflector and isotropic scattering at the surface (Figure 4.1), these calculations find that incident light that is totally internally reflected will pass back and forth through a semiconductor layer, with index of refraction n, an average of $2n^2$ times. With each pass a distance of 2 times the layer thickness, this results in an effective optical path length of $4n^2$ times the thickness.

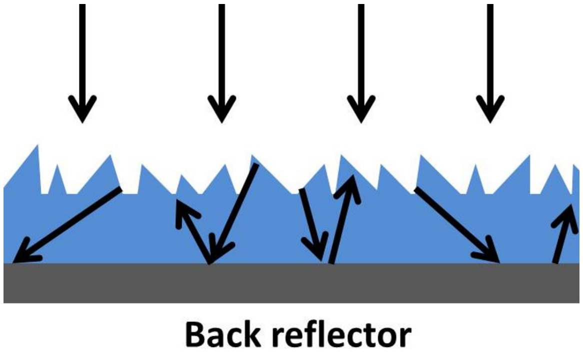

Figure 4.1. Structure illustrating Lambertian scattering of incident light by surface features.

Since the path length of light on a flat layer with no back reflector is simply the thickness of the semiconductor, the textured geometry offers an enhancement in the path length of light of $4n^2$. Due to the subwavelength dimensions of these structures, however, this ray optics approach does not sufficiently describe the characteristics of light propagation in these films, and a wave optics analysis must be utilized. One of the underlying assumptions utilized in this calculation is that light is fully randomized upon interaction with the surface and all the available photonic states are equally occupied. An important feature of a wave optics analysis of light trapping in these films is the potential ability to surpass the $4n^2$ limit in specific wavelength ranges by manipulating the density of photonic states as determined by the array geometry, and recent studies have illustrated the potential for periodic arrays to surpass this Lambertian limit, albeit for a limited angular range [71]. Additionally, recent studies have assessed the potential for increased light absorption for both random and ordered dielectric surface arrays, using a ray tracing approach to determine the dependence of light scattering with surface feature and array geometry [6]. While many of these studies report increased light absorption in silicon layers of 1μm thickness or greater, this study examines an ultrathin silicon layer, less than 220nm. This thickness regime allows for the existence of waveguiding modes that can be accessed by the obliquely scattered light, introducing an additional mechanism for light trapping. The scattering that occurs at these surface features can redirect light into thin film and periodic modes of the absorbing film, exploiting both the periodicity of the

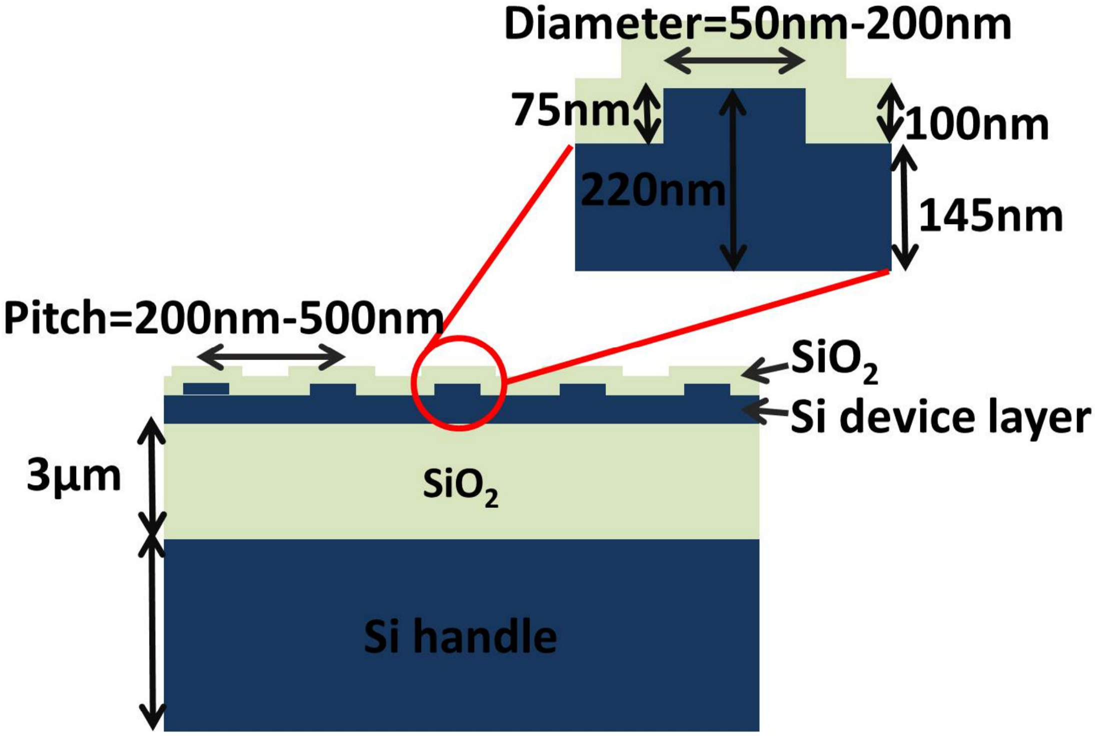

Figure 4.2. Device structure prototype.

surface texture and the waveguide structure of the device. This examination of the effect of dielectric surface textures is first focused on the analysis of scattering resulting from regular square arrays of silicon cylinders etched into 220nm-thick silicon device layer on oxide, and this prototypical structure is used for both simulation and experimental measurements as illustrated in Figure 4.2.

The incident and scattered light result in a regular interference pattern with characteristics determined by the thickness of the underlying silicon film and the periodicity, geometry, and dielectric function of the array material. The scattered light satisfies the Bragg condition for constructive interference in a periodic pattern, resulting in significant enhancement of light absorption centered at the corresponding resonant wavelengths. This chapter will focus on optimizing the incoupling and absorption of incident light by minimizing the reflectivity losses and exploiting the periodic and thin-film waveguiding modes of the silicon film. The potential for incorporating these design guidelines in a fabricated structure is demonstrated through the use of a novel fabrication technology and illustrates a significant step towards the development of an inexpensive and highly efficienct thin-film silicon solar cell.

4.2 FDTD simulations

Full-field FDTD simulations were employed to predict the light trapping characteristics of these dielectric arrays and to assist in the analysis of the scattering and confinement behavior in the absorbing silicon layer. An initial 220nm thick silicon layer is selectively etched in the simulation structure to produce a pattern of silicon cylinders on the surface, decreasing the overall volume of the absorbing layer from that of a flat 220nm silicon film. Using previous simulations of flat 220nm silicon layers, an optimum thickness of 100nm SiO_2 for use as an anti-reflection coating was added as a conformal layer on the surface of the silicon device layer. Periodic boundary conditions are used to simulate a square array of dielectric surface structures, and optical constants for Ag and Si are the same as those determined previously via ellipsometry. A 5nm mesh step is utilized in the area that includes the scattering figure. The wavelength ranges from 400nm to 900nm, where silicon exhibits the largest spectral response, and is simulated as a monochromatic source in 5nm increments. From these simulations, the correlation between light scattering and absorption in the thin-film device structure and the dielectric array geometry is examined and mechanisms for increased light confinement are elucidated.

4.3 Reflectivity and surface geometry

For either thick or thin solar cells, incoupling of light can be maximized by minimizing the reflective properties of the surface. A bare silicon surface loses close to 40% of incident light to reflection; for this reason anti-reflective coatings have long been utilized in the fabrication of solar cells. A SiN_x layer with thickness $\frac{\lambda}{4n(\lambda)}$ has been the manufacturing standard, decreasing the reflectivity to below 20% when averaged over the solar spectrum due to destructive interference between the incident and reflected light [27]. SiN_x has an index of refraction that provides good impedance matching between air and the underlying silicon, while the low extinction coefficient of this material prevents unintended absorption in this layer. This technique, however, is predominantly effective only over a narrow angular range. Various techniques have been studied to minimize reflectivity over a broader range of angles, including surface texturizing via anistropic chemical etching [30], and multilayer anti-reflective coatings using porous silicon or titianium dioxide to create a graded index of refraction [40, 59]. The anisotropic etch approach is a simple fabrication step, but due to the large dimensions of the surface features produced with this etch, this technique can only be applied to devices with films of thickness greater than 10μm. A multi-layered structure minimizes reflectivity by introducing a gradual change in the index of refraction at the reflection interface. This method is significantly more effective than a chemical etch but is much more complicated to fabricate. The use of subwavelength dielectric arrays is suitable for large-scale fabrication due to a recently developed nanoimprint lithography method, and the approach of this study is to evaluate the reflectivity properties from dielectric textures to determine the function of array geometry in determining light scattering behavior attributed to these structures.

4.4 Fabry-Perot modes in 220nm silicon layer

To provide context for the numerous scattering effects produced by this scattering geometry, this study begins with an initial examination of the modes of a flat film of silicon without any surface texture added. A flat silicon film will exhibit Fabry-Perot peaks as the reflected wave interferes with the incident plane wave. The location of these peaks can be predicted by calculating the wavelength at which the phase difference between these waves will yield destructive interference,

$$\Phi = \frac{2\pi}{\lambda} d sin \Theta \tag{4.1}$$

Here n is the index of refraction of the silicon layer, d is the thickness of the film, and Θ is the incident angle measured from normal incidence. The spectral features that result from the interference between the reflected and incident light are evident when comparing the absorption for a single pass through a silicon absorbing layer with the absorption for multiple passes, and Figure 4.3 plots the light absorption for light that passes through 220nm Si once only, compared with multiple passes through the layer upon reflection at the back interface. Figure 4.3 shows the absorption of a 220nm silicon layer on oxide when light is permitted only one pass through the silicon and when multiple passes are allowed. The peaks that occur with multiple passes (at λ=420nm,450nm,530nm, and 650nm) can be attributed to this Fabry-Perot effect in subsequent reflectivity studies.

4.5 Reflectivity with pitch variation for dielectric arrays

An important parameter in determining the potential for light trapping in thin films with dielectric surface arrays is the spacing of a periodic array. The variation of this pitch can not only change the incoupling efficiency of incident light and resonant modes of the structure, but can also have a significant effect on the anti-reflective properties of the surface. FDTD simulations were conducted that systematically varied the pitch of a square array of cylindrical dielectric structures to determine the effect of pitch on reflectivity. The simulated structure was a base layer of 145nm silicon on an oxide base, with 75nm height silicon cylinders, to represent a 220nm silicon layer etched to produce 75nm height cylinders, and the pitch was varied from 200nm to 600nm (See Figure 4.2). A power monitor was placed above the simulation structure, and the transmission through this monitor is normalized by the source power to yield the reflectivity at the surface of the silicon film.

The simulated reflectivity of the arrays with 200nm and 300nm pitch indicates a significant decrease in reflectivity losses over the majority of the visible spectrum when compared with an untextured silicon layer. Figure 4.4 plots the reflectivity of each of these array for comparison to a flat 220nm silicon layer and exhibits strong

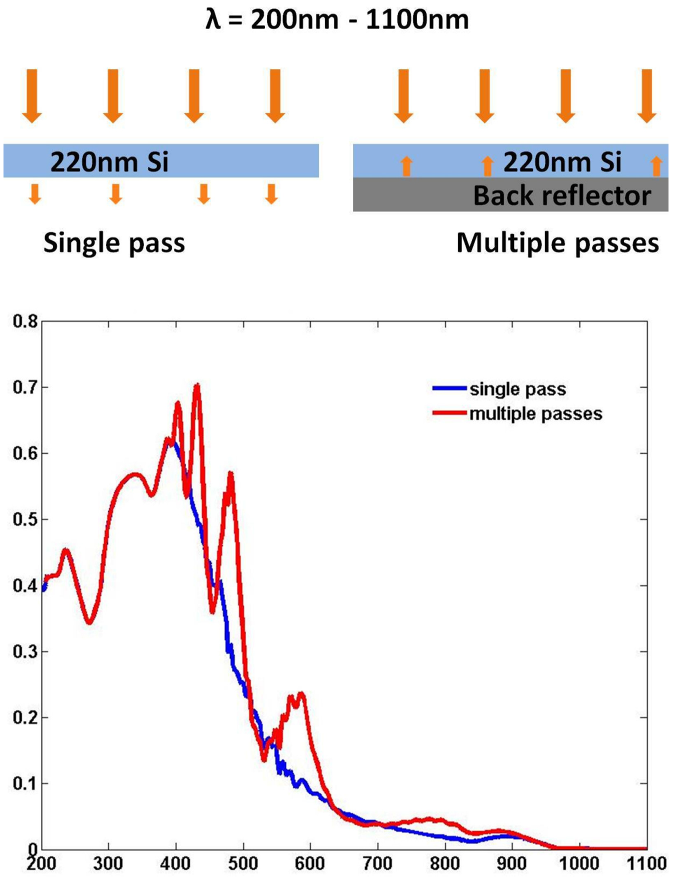

Figure 4.3. Comparison of calculated absorption from single vs. multiple passes through a 220nm silicon layer, demonstrating Fabry-Perot modes.

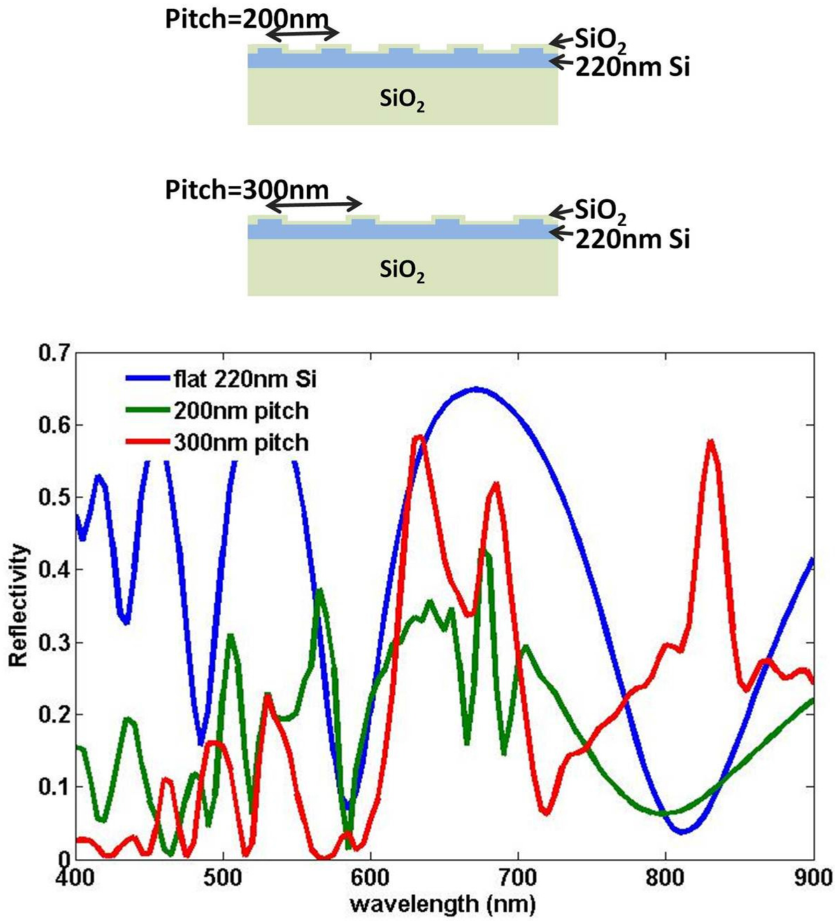

Figure 4.4. Comparison of calculated reflectivity for 200nm and 300nm pitch arrays.

suppression of reflectivity, especially in the shorter wavelength regime. Significant suppression of reflectivity is observed at wavelengths that exhibit Fabry-Perot resonances in a flat silicon layer, at λ=420,450,530, and 650nm. The scattering at the cylinders suppresses these resonances by perturbing the coherence of the incident light and the light reflected at the back interface, and consequently the suppression of reflectivity is most significant at these peaks. The decrease in reflectivity observed with a 200nm pitch array surpasses that of a 300nm pitch array for much of the visible wavelength range above λ=525nm. This effect can be attributed to the increased density of scattering cylinders for a smaller pitch, thereby increasing the redirection of incident light into angles subject to total internal reflection in the silicon film. To determine the pitch that results in the minimization of reflectivity, the fraction

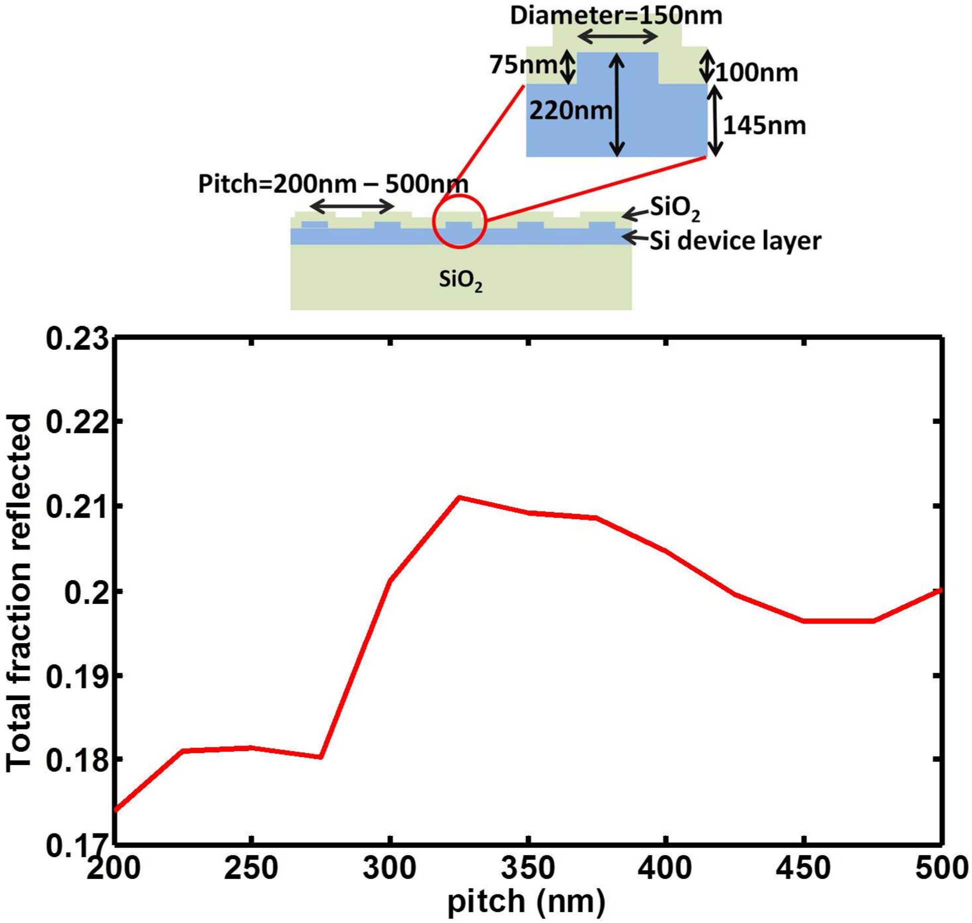

Figure 4.5. Calculated total fraction of photons reflected with array pitch.

of light reflected is weighted by the AM 1.5 solar spectrum to yield a total number of photons per wavelength reflected at the silicon layer interface. This is then integrated over the visible spectrum and normalized by the total incident light to yield a net fraction of photons reflected at each pitch. The results of this calculation are exhibited in Figure 4.5 and indicate that a smaller pitch is ideal for optimizing the anti-reflectivity properties of these surface arrays. A close-packed array of dielectric cylinders will allow the maximum transmission of incident photons into the underlying silicon absorbing layer. However, since the silicon layer is an inefficient absorber at longer wavelengths, incident photons in this range will not produce carriers even with effective transmission into the silicon film unless methods are employed to increase the path length of the light within this film. For this reason an optimal anti-reflective

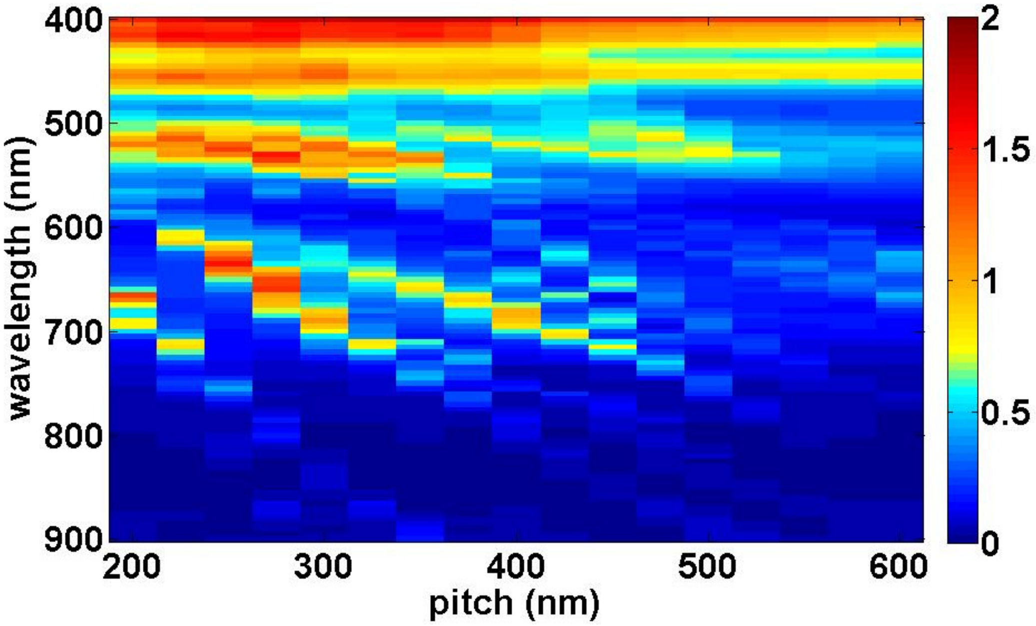

Figure 4.6. Simulated optical generation rate enhancement with array pitch exhibits evidence of periodic Bloch modes.

surface may not result in maximum light absorption in the film, and the overall light absorption with varying pitch therefore must be considered.

4.6 Pitch optimization with total absorption

The periodicity of the surface geometry in these structures is a significant parameter in determining the characteristics of light absorption in the underlying film. A regularly periodic dielectric array will produce periodic Bloch modes resulting from interaction between scattering structures and waveguiding modes of the film, resulting in light confinement patterns determined by the pitch of the array. By calculating the optical generation rate in these films using the results of FDTD simulations, the effect of varying pitch on light absorption over the visible spectrum can be evaluated. Shown here is the enhancement in optical generation rate of a patterned array over the optical generation rate in a flat 220nm silicon layer (Figure 4.6).

The influence of the periodicity of a dielectric array is demonstrated by the existence of several Bloch modes, indicated by light absorption peaks that change linearly with pitch. The increasing distance between features and a resulting red-shifting of the pitch-dependent resonance of the array is indicative of the dependence on distance between array features rather than the geometry of the individual surface structure. A decrease in the amplitude of the enhancement peaks is also observed with increasing pitch, indicative of a decrease in the interaction between particles. Both of these observations indicate strongly the importance of periodicity in the light trapping features of these structures. A smaller pitch demonstrates enhancement largely due to its increased efficiency as an antireflective layer, while for larger pitches a decrease in performance in the blue portion of the spectrum occurs due to increased reflectivity. Since the scattering efficiency of these features is higher for short wavelengths, scattering from an array with a smaller pitch will more significantly decrease the reflectivity as the density of the scattering structures increases. A smaller pitch will also result in an overall increase in scattering due to the higher density of scattering structures and increased absorbing volume, and broadband enhancement is exhibited for higher density arrays with pitches from 200nm to 300nm. The interaction between waves scattered at each Si cylinder results in the creation of resonant modes at wavelengths at which constructive interference occurs between these wavefronts. Referring to Figure 4.6, an arbitrary pitch exhibits several modes, indicated by the intersection of the pitch and the line of the optical generation enhancement peaks. Specifically, for a 400nm pitch array peaks are observed at λ=520nm, 650nm, 700nm, and 740nm. Each of these wavelengths accesses a different mode of the structure, and to examine this further a cross section of the optical generation rate through the structure is presented in Figure 5.8. For λ=520nm and 700nm, much of the absorption is taking place in the silicon cylinder rather than the silicon film, while for the mode occurring at λ=650nm, much of the absorption occurs at the high order mode within the film. For λ=520nm and 650nm, modes of a higher order are exhibited, while for the lower order mode at λ=740nm clear interference between the Fabry-Perot pattern and the Bloch mode is observed. To evaluate the net absorption with

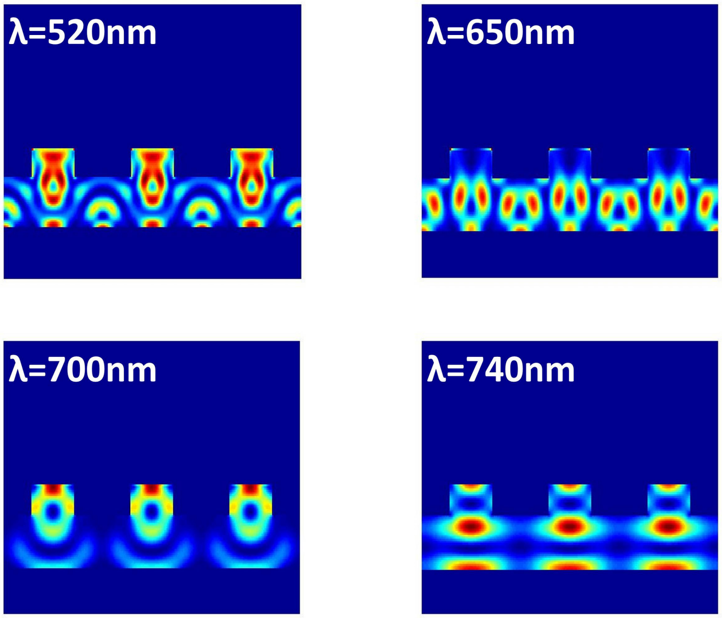

Figure 4.7. Comparison of simulated optical generation rate cross sections for multiple modes found in a 400nm pitch silicon array.

pitch, the optical generation rate in the silicon is calculated and weighted by the AM 1.5 spectrum. The resulting spectra are integrated to determine the total number of photons absorbed for each pitch and plotted in Figure 4.8. A maximum of absorbed photons occurs for a 325nm pitch array, despite the high reflection losses calculated for this pitch. This result illustrates that even though fewer photons are transmitted into the film for a 325nm pitch array, the modes present in this structure geometry result in higher absorption of the transmitted light and consequently higher overall carrier generation. This optimal pitch is dependent on film thickness as the periodic modes of the array interact with the thin-film waveguiding modes of the silicon film, and this optimal quantity determined here is applicable specifically to a patterned 220nm silicon film.

4.7 Dielectric arrays as photonic crystals

The periodic structure of these dielectric arrays suggests an additional analysis of this system in terms of a photonic crystal. Photonic crystals are an optical material

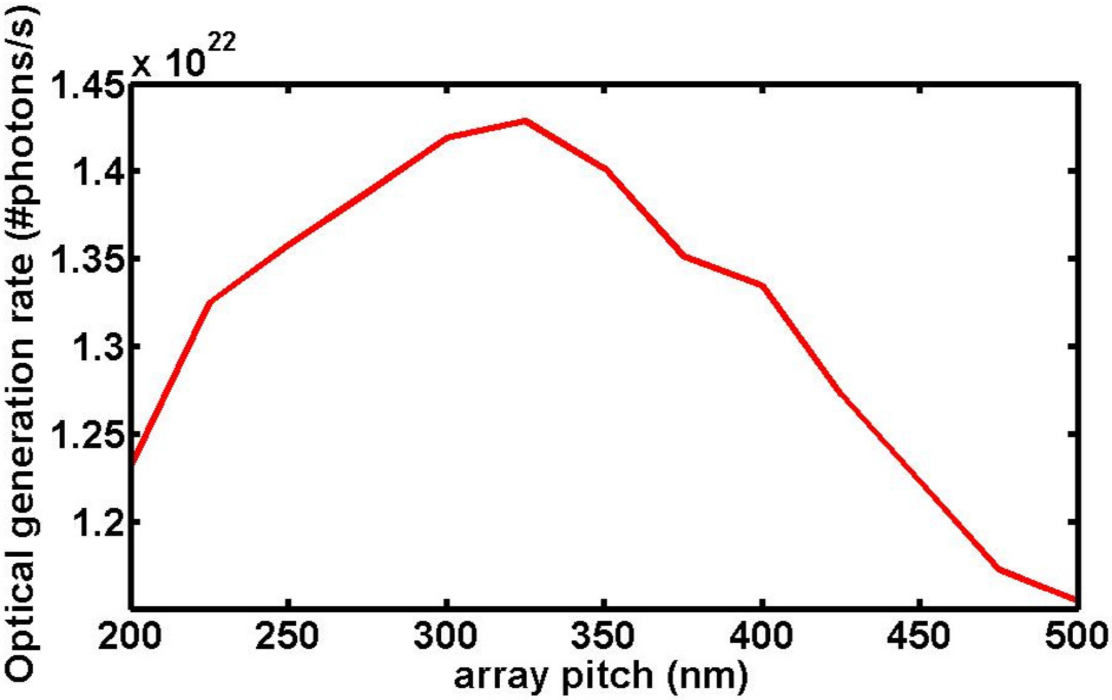

Figure 4.8. Calculated total photon absorption in silicon layer integrated over AM 1.5 spectrum with varying pitch shows optimal pitch at 325nm.

made by periodically modulating the dielectric constant on a scale comparable to the wavelength of the interacting light. In analogy to the behavior of electrons in semiconductors, light propagation in these crystals can be described by Bloch functions, with resulting modes producing photonic band gaps. In principle, this design has the potential to exceed the $4n^2$ limit previously determined by Yablonovitch for a randomly textured surface. With isotropic scattering at the surface, the incident photons are assumed to be redistributed evenly among all the photonic states, giving a mode density in k-space of $(\frac{1}{2\pi})^3$. The net intensity enhancement is given by:

$$\frac{\rho(\omega)}{(\frac{1}{2\pi})^3} * n^2 \tag{4.2}$$

[42]. For isotropic scattering, this calculation yields the predicted $4n^2$ enhancement. However, this equation illustrates the potential to exceed this limit by increasing the density of states in the spectral range of interest. In the same manner that a periodic distribution of electrons gives rise to an electron energy band gap, a periodic array of dielectric or metal structures results in a range of forbidden wavelengths at which light cannot propagate; this results in a peak in reflectivity in this band. The interaction between light and a photonic crystal can be predicted by examining the photonic density of states in this structure. Analogous to the band structure that results from the periodic potential of an atomic lattice in a semiconductor, a photonic crystal will have no available states within the photonic band gap, but a high density of states at the band edge. The potential for light absorption enhancement in a photonic crystal lies in the ability to engineer the band structure to optimize absorption in a high-power portion of the solar spectrum while shifting the photonic band gap outside of the spectral range of useful light. The location of the photonic band gap in a 2D photonic crystal structure can be determined using FDTD simulations. Each of the frequency-dependent modes of the structure can be written as the periodic function:

$$E(x) = exp(ika)u(x) \tag{4.3}$$

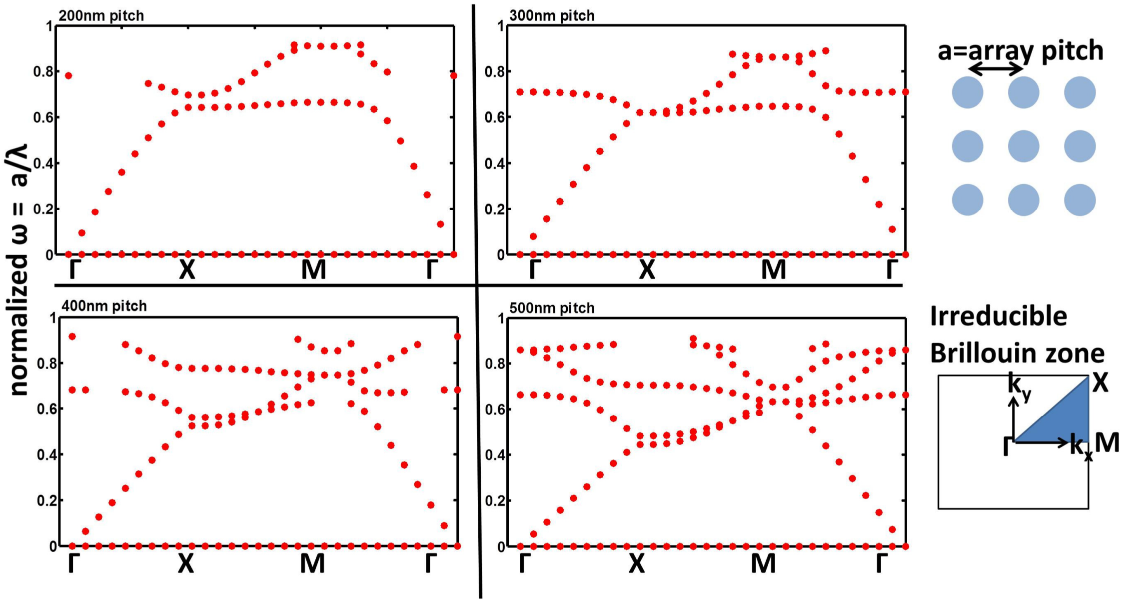

Figure 4.9. Photonic band structure for periodic Si array.

where u(x) is a periodic function of x. Randomly oriented dipole sources in this simulation excite these modes of the structure, and these modes can be identified by performing a fast Fourier transform (FFT) of the electromagnetic fields versus time. The dispersion of all the modes within the frequency range of interest, $w(k_{mode})$, is then plotted in Figure 4.9, resulting in a photonic band structure.

The bandstructure for the dielectric arrays based on the prototypical structure used in this study was calculated, and the resulting photonic band structure is presented for wavevector κ within the irreducible Brillouin zone of this periodic 2-dimensional crystal structure. Since additional values of κ outside of this zone are redundant, the entire dispersion can be represented by this reduced range. The resulting plots demonstrate that a photonic band gap does not exist for this structure geometry in the wavelength range of interest. A very narrow gap is observed for a 200nm pitch array, but the spectral location of this gap corresponds to a wavelength far below the spectral range of interest for photovoltaics. The lack of a photonic band gap in the visible spectral range is a fortuitous result since the overlap of a photonic band gap with the visible light spectrum would result in a peak in reflectivity due to the presence of forbidden modes within the gap. While further studies may yield techniques to exploit the photonic band gap effect by manipulating the geometry of a dielectric array, these results predict that this structure will not exhibit effects from this phenomenon.

4.8 Shape of scattering structures

The influence of the shape of the scattering object on the reflectivity at the surface was next examined. The textured portion of the silicon layer has an effective refractive index between that of air and the underlying solid layer of silicon due to its modulation between the refractive indices of the two materials, and consequently could be described as a graded index of refraction. Since such a graded index of refraction will suppress reflectivity at an interface, the surface geometry was examined in terms of the effective refractive indices gradient through the dielectric surface features. Both a pyramidal and cylindrical geometry were simulated in this study; since the pyramidal structure will provide a more gradual graded index, this geometry may be expected to exhibit a larger suppression of reflectivity compared with the cylindrical structure, especially at short wavelengths where reflective scattering is most pronounced. To determine the reflectivity, three varying scattering geometries were constructed in the FDTD simulation environment representing a close-packed pyramid surface with a pitch of 400nm and a height of 75nm, a pyramid structure with a pitch of 400nm, a 200nm base, and 75nm height, and a cylindrical structure with a 400nm pitch, 175nm diameter, and 75nm height. (Figure 4.10). The close-packed pyramid represents the most gradual change of refractive index from air to that of silicon, while the second pyramid geometry represents a more abrupt change in index. The cylinder represents the least gradual of the structures since it allows only one intermediate index between air and silicon for the entire thickness of the structured layer. A decrease in reflectivity at shorter wavelengths is observed for the 200nm pitch pyramid structure compared with the 400nm, close-packed pyramids,

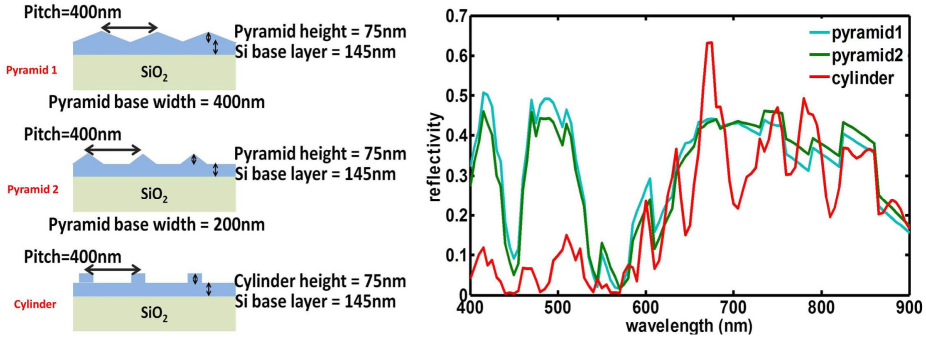

Figure 4.10. Calculated reflectivity spectrum with varying surface feature geometry.

indicating that the observed anti-reflective properties cannot solely be attributed to a graded index effect. Most notably, however, a significant decrease in reflectivity at smaller wavelengths is seen for the cylindrical structure, despite its discrete changes in index at the interfaces between the surface texture and both the air and the underlying substrate. This phenomenon clearly demonstrates the significant role of the periodicity of surface arrays in the collection of incident light in these structures. A reflectivity map over varying pitches reveals peaks in reflectivity for a 400nm pitch array of silicon cylinders are most pronounced at λ=675nm, 750nm, and 775nm and increase linearly with wavelength as the pitch increases. This corresponds to the three highest peaks seen for cylinder arrays in the reflectivity versus wavelength plot, and moreover confirms that this modulation of peaks is a result of periodic modes in the surface structure.

4.9 Thin-film waveguide modes

The scattering that occurs at the dielectric cylinders on the surface of this thin-film silicon structure facilitates light absorption by diffracting light into the resonant modes of the thin film. The periodicity of the scattering geometry, the thickness of the absorber layer, the dielectric function of the materials, and the wavelength and angle of the incident light determine the location and intensity of these modes. Due to the subwavelength thickness of the film, this geometry can support guided modes and can be studied in terms of a dielectric slab waveguide. A waveguide is a high-refractive index dielectric material embedded between two lower index materials, in our structure a silicon layer on an oxide substrate with a 100nm conformal surface layer as exhibited in Figure **??**. This structure supports both a finite number of modes guided parallel through the film, as well as an infinite number of evanescent modes decaying perpendicular to the film. A waveguiding mode must satisfy the condition:

$$k(2dcos\Theta) - 2\Phi = m(2\pi) \tag{4.4}$$

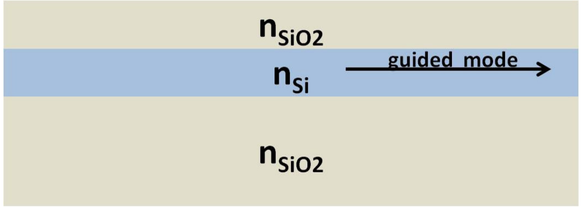

Figure 4.11. Geometry of dielectric slab waveguide.

Here k is the wavevector in free space, n is the wavelength-dependent index of refraction of silicon, m is a positive integer indicating the mode number, Θ is the angle of reflection in the film, and Φ is the phase change upon reflection at the boundary of the film. A propagation constant can be defined as:

$$\beta_m = ksin\Theta_m = \frac{n2\pi}{\lambda}sin\Theta_m \tag{4.5}$$

If this is described in terms of light travel in one dimension along the x-axis, the propagation of electromagnetic waves through this structure is described by the wave equation:

$$\bigtriangledown^2 E + k^2n^2E = 0 \tag{4.6}$$

Solutions must be continuous at each of the interfaces between silicon and the oxide layers and are of the form:

$$E(x,t) = E(x)exp(i(\omega t - \beta x)) \tag{4.7}$$

where β is the propagation constant that represents the phase and decay of the light as it travels through the film. In each dielectric layer, the propagation can be described by:

$$(\frac{\partial}{\partial x})^2E(x) + (k^2n^2 - \beta^2)E(x) = 0 \tag{4.8}$$

This equation shows that for $k\mathrm{n}_(SiO2)<\beta<\mathrm{kn}_{S}\mathrm{i}$, sinusoidal solutions exist in the silicon layer, since $\frac{\partial}{\partial x}^2 E(x) < 0$, whereas elsewhere the solutions are exponentially decaying, since $\frac{\partial}{\partial x}^2 E(x) > 0$. These sinusoidal solutions have a periodicity of $\frac{2\pi}{\beta}$ in the direction of propagation and are defined as the guided modes of the dielectric structure. Due to the momentum mismatch that exists between the wavevector of the light incident from free space and the waveguide mode of the silicon film, a means of providing this additional momentum is necessary for coupling to these modes. Surface scattering via dielectric cylinders is one means of overcoming this mismatch by providing the added momentum needed to couple to the waveguide mode from free space. From Snells Law, the in-plane component of the incident light is given by $\mathrm{k}_0\mathrm{sin}\Theta$ for angle of incidence Θ. Additionally, the momentum provided by the scatterers is equal to $\frac{2\pi n}{a}$ for a=pitch of the array and n=nonzero integer [93]. This equation can be used to determine the wavevector(s) of incident light that will couple into a dielectric slab waveguide for a given angle of incidence. For coupling to the waveguide modes to occur, this condition must be satisfied:

$$k_(waveguide) = k_0 sin\Theta + \frac{2\pi n}{pitch} \tag{4.9}$$

A method of incoupling must be employed to access these waveguiding modes, and this is accomplished in this structure through light scattering at the dielectric cylinders. Incident light is scattered anisotropically when it strikes these cylinders; this light can be expressed as a plane wave with wavevector k_0 and angle of incidence Θ_0. The angle of travel through the silicon film is determined by Snells law:

$$n_1 cos(\Theta_1) = n_2 cos(\Theta_2) \tag{4.10}$$

If the condition for total internal reflection is satisfied, that is if Θ_2 exceeds the critical angle for total internal reflection, the light will then be confined to the waveguide. Resonant coupling of light to the modes of the waveguide occurs when the wavevector of the light diffracted at the scattering structure matches that of the guided modes in the thin film. The number of guided modes that can be supported by this structure

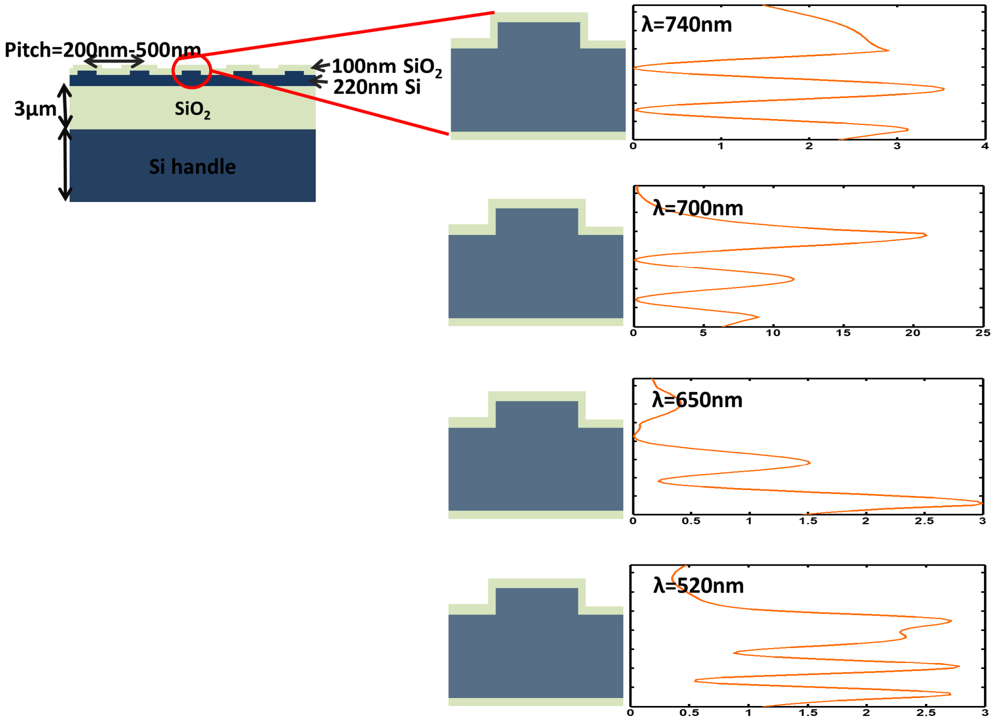

Figure 4.12. Calculated power density distribution in cross section for various modes of a 400nm pitch array.

is determined by the thickness of the waveguide, the indices of refraction, and the wavevector of the incident light. The calculated pattern of light intensity throughout the cross section of these films reveals the geometry of light trapping in relation to the dielectric surface features. To highlight the modal nature of this light trapping, the geometry of several mode orders is illustrated via a cross sectional view of the power density distribution through the structure (Figure 4.12). The wavelengths represented in Figure 4.12 reflect the wavelengths that yielded prominent enhancement peaks for a 400nm pitch array. The distribution at λ=740nm is illustrative of approximately a first-order waveguiding mode, with higher order modes evident at λ=650nm and λ=520nm, and offers a quantized view of previously observed mode profiles. The waveguide modes in this SOI structure were further determined by varying the thick-

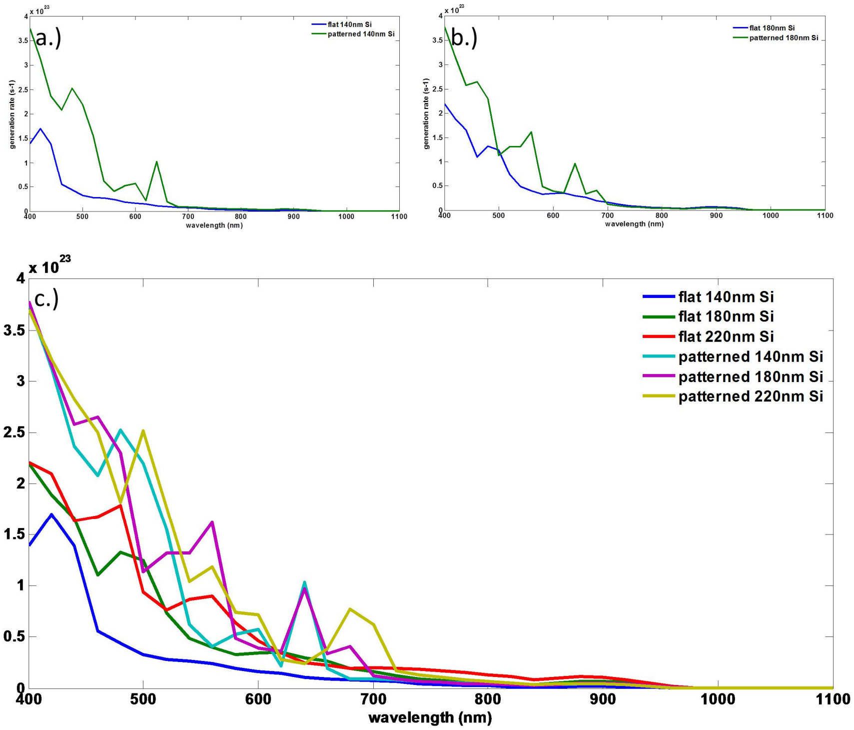

Figure 4.13. Simulated optical generation rate comparison for flat vs. patterned silicon for a.) 140nm total layer thickness b.) 180nm total layer thickness c.) Varying thickness to demonstrate shift with thin film waveguide mode coupling.

ness of the thin Si film in FDTD simulations. By applying perfectly matched layer (PML) boundary conditions in this model, any periodic effects are eliminated and any features that result from the systematic thickness variation can be attributed to waveguiding modes. As the thickness increases, the wavelength for which a particular mode order exists will red shift and additional modes are expected to emerge. To determine the role of these thin-film waveguide modes on light absorption, the resulting optical generation rate spectrum is calculated and plotted in Figure 4.13. In this plot of the generation rate, a thickness of 140nm Si results in peaks in light absorption at λ=500nm, 600nm, and 640nm. As the thickness is increased to 180nm Si, these peaks shift to λ=560nm, 640nm, and 680nm, respectively, with evidence of an additional mode emerging at λ=460nm. These peak locations can be extrapolated to align with the previously observed peaks in calculated optical generation rate for the prototypical structure with a base silicon thickness of 145nm, with peaks exhibited at λ=520nm, 650nm, and 700nm, and therefore offer evidence of the waveguiding nature of this geometry. This plot elucidates the role of a singular scatterer in providing the additional momentum needed to couple into these modes, apart from any consideration of array geometry. The scattering of a singular particle will be further examined by identifying the diameter-dependent spectral features of light absorption in these films.

4.10 Diameter variation

The use of a dielectric patterned surface allows access to the modes of the thin-film structure, but analysis of a single scattering object will allow the further examination of the influence of the geometry and size of a discrete scattering feature. The influence of the diameter of an individual scattering object is studied to determine the most effective geometry for light coupling into a thin absorber. When the size of the surface features is of the same order as the wavelength of light, the light may interact with the particle with an effective extinction cross section that exceeds its physical cross section due to the interaction of the light with the modes of the device structure. The light will either be absorbed or scattered by the surface feature, and by optimizing the scattering cross section the redirection of light into the absorbing substrate can be maximized. In contrast to a metal nanoparticle, photon absorption by a dielectric particle could potentially produce a carrier capable of being collected at the contacts. However, while some of the carriers generated in the silicon cylinders may be able to diffuse to the junction for collection, the increased surface and bulk combination associated with the increased distance to the junction may prevent efficient collection of carriers from the patterned surface features. Furthermore, efficient collection is less likely for materials with a lower diffusion length, and if multi-crystalline silicon thin films with a higher density of defects are used, the maximization of scattering will still result in the most effective light absorption. This increased scattering will lead to an enhancement of the optical path length both

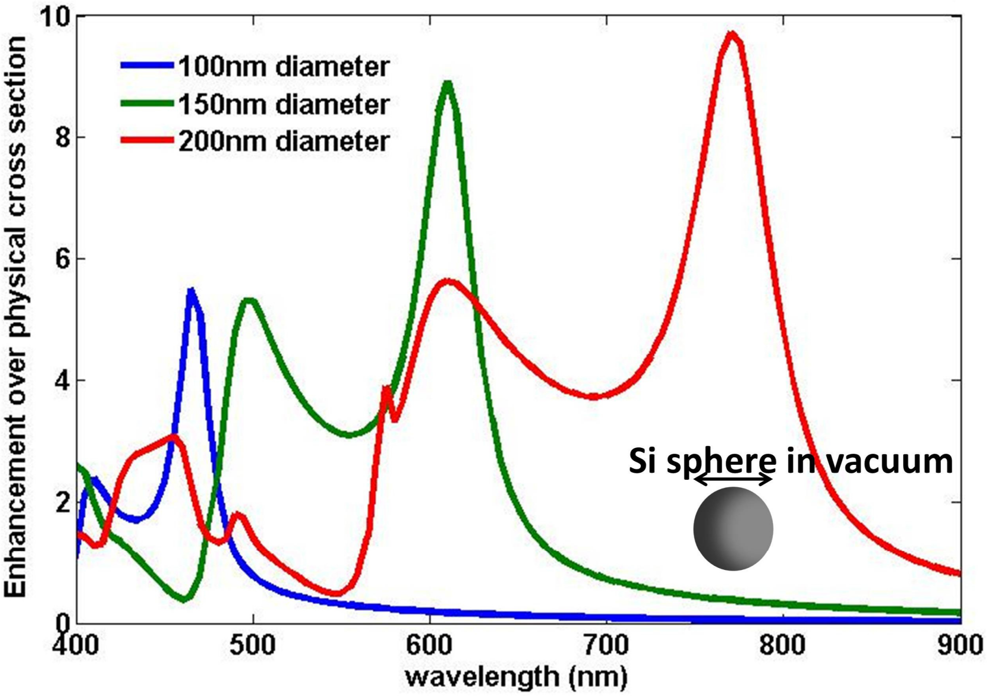

Figure 4.14. Calculated scattering cross section enhancement for silicon spheres in free space.

by obliquely redirecting incident light and by accessing the thin film modes of the underlying silicon layer. For these reasons a maximum scattering cross section with a minimum absorption cross section is desired. To optimize the diameter of these particles, the Mie approximation is used to calculate the scattering efficiency of a singular scattering in the same manner used to derive the effective scattering cross section for Ag nanoparticles in the previous chapter. For simplicity, a Si sphere is used as the scattering object, with the expectation that the results of this calculation will yield general insights into the scattering behavior with particle size, as the behavior of light extinction is expected to change systematically with particle geometry and dielectric environment. The wavelength-dependent scattering cross section of silicon spheres in a vacuum was calculated using the same dielectric functions used for FDTD simulations, and a general increase in scattering cross section with size is observed, as anticipated due to the increase in physical size of the scattering object. These calculations predict scattering that occurs at a single structure; the interaction

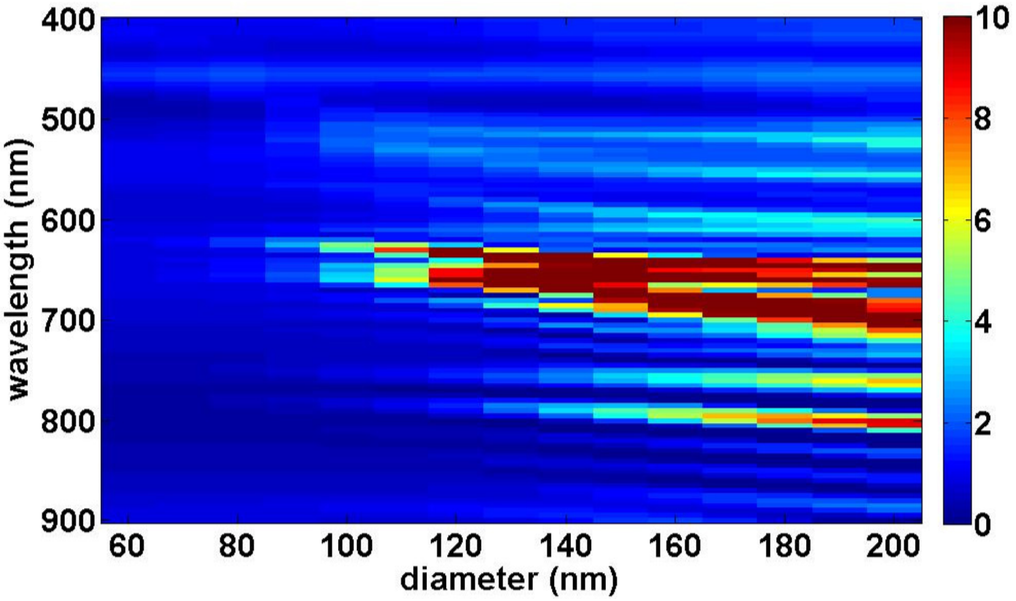

Figure 4.15. Simulated quantum efficiency enhancement with diameter variation for a 400nm pitch array, showing emergence of resonant modes with increasing diameter.

between these structures is expected to produce significant additional effects in light confinement in these films. To determine the collective effect of a scattering array, a 400nm pitch square array of silicon cylinders is studied by varying the diameter in the electromagnetic simulation environment and examining the resulting quantum efficiency with diameter. The results of these simulations are plotted as the calculated enhancement in quantum efficiency over a flat 220nm silicon film in Figure 4.15. The emergence of resonant modes is clearly exhibited with increasing diameter. A mode is identified at λ=590nm that increases in intensity with increasing diameter, with an additional mode appearing at λ=690nm when the diameter exceeds 100nm; both of these modes exhibit a constant spectral location and an increase in magnitude with increasing diameter. For cylinders with a small diameter placed far apart, they can be described as dipole scatterers, and the interaction between them is dominated by the interference of these scattered waves with the incident light. For larger diameter

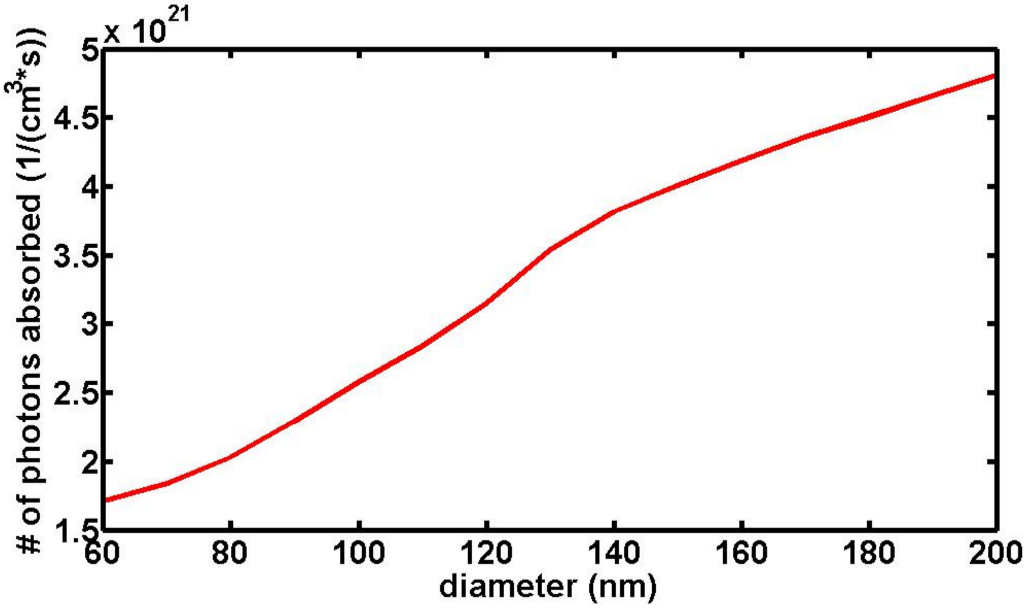

Figure 4.16. Total photons absorbed in AM 1.5 spectrum with surface cylinder diameter.

cylinders, these features can no longer sufficiently be described as point dipoles, and instead the shape of the cylinder plays a larger role in determining the scattering pattern. The relative invariance of the spectral locations of the generation rate peaks indicates that these modes are a characteristic of the array pitch and independent of particle diameter; referring to Figure 4.14, the existence of these resonant modes is confirmed at these wavelengths for a 400nm pitch array. The increase in quantum efficiency enhancement with increasing diameter is commensurate with the increased effective scattering cross section of the individual particle, resulting in an increase in the fraction of light scattered into the film. To optimize the diameter of these arrays, the calculated quantum efficiency is weighted by the AM 1.5 spectrum and integrated to yield a total number of photons absorbed for each diameter. The resulting plot exhibits a systematic increase in photons absorbed with increasing diameter, a result of the maximized scattering cross section as well as the maximized overall absorbing volume for larger diameter particles (Figure 4.16). As previously stated, however, photons absorbed in the scattering cylinders are less likely to be efficiently collected, and subsequent electrical simulations and measurements are required to determine the actual carrier collection to aid in further refinement and optimization of this device design.

4.11 Angle-resolved spectral response

Most practical installations of solar devices do not include a tracking system that keeps the incident angle of the sun constant with respect to the absorbing layer. For this reason, sufficient absorption over a broad range of angles is required for overall maximization of light absorption efficiency in thin-film cells. The practical application of dielectric surface arrays for solar cell devices therefore depends upon the efficiency of light capturing over a wide range of incident angles. The angle-dependent light absorption is evaluated using FDTD simulations. This plot shows the enhancement of the simulated optical generation rate over a flat 220nm silicon layer, with the presence of periodic modes clearly illustrated by the linearly varying peaks in intensity. Enhancement peaks are illustrated for all simulated angles and are further evidence of the existence of periodic Bloch modes in this structure. Although the reflectivity increases with increasing angle, the periodic array still exhibits an increase in overall light absorption over a flat silicon layer throughout the measured angular range.

4.12 Fabrication: nanoimprint lithography

A fabrication technique with high resolution is required to realize these periodic dielectric arrays. While AAO membranes can be used to manufacture relatively uniform arrays over areas up to 1cm^2, this fabrication method is not practical over larger areas. In addition, the resulting arrays are not perfectly periodic, and the perturbation of this periodicity is expected to have a significant effect on the light trapping behavior in the absorbing film. E-beam lithography can be used for high-resolution pattern

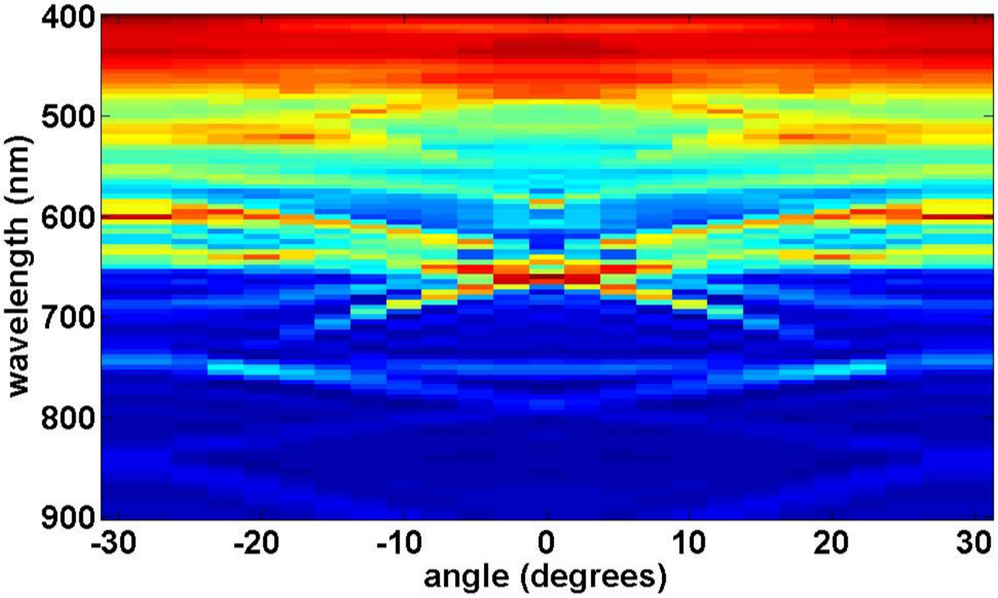

Figure 4.17. Calculated angle-resolved photocurrent enhancement for a 400nm pitch silicon array.

fabrication, but this technique is impractical for industrial-scale applications. Optical lithography can be used for high-fidelity pattern formation on an arbitrarily large scale, but since the resolution of this patterning technique is limited by the diffraction of light subwavelength features cannot be produced with this method. Nanoimprint lithography is a technique that has been explored to overcome the scalability and resolution restrictions presented by other fabrication methods. A method of nanoimprint lithography has been recently developed at Philips Research that allows for fully conformal coating of the resist-coated substrate, allowing high fidelity pattern transfer even for substrates that are not fully planar [86]. First a master pattern is fabricated on a Si wafer via any standard process, and for this study e-beam lithography is employed. A composite PDMS stamp is molded from the master and used to emboss a substrate coated with resist, allowing the pattern to be transferred and the master stamp to be reused thousands of times. The method used here, substrate conformal imprint lithography (SCIL) was developed to allow for high fidelity printing over wafer-scale areas, even for substrates that are not fully planar. In this method, the PDMS stamp is a composite of high-modulus PDMS, which defines the nanoscale features, and low-modulus PDMS, which provides flexibility. The silicone rubber is then glued to a flexible glass sheet, as illustrated in Figure 4.18. The silicone rubber is rigid enough that the pattern fidelity is maintained, and the glass is thin enough that the rubber stamp structure is sufficiently flexible to fully conform to the substrate geometry. The stamp can be used to pattern many different resists, such as UV-curable photoresists as shown in Figure 4.19, and a silica sol-gel is employed for the samples fabricated for this study. Substrates are first coated in the sol-gel resist, then step-wise contact between the rubber stamp and the resist is performed by the use of a series of pneumatic valves that release in series as the stamp contacts the substrate. The resist is then cured with the excess solvent diffusing into the stamp, and the stamp is removed from the hardened resist with the same step-wise motion. For the structures used in this study, SOI wafers were patterned using this SCIL method, resulting in an array of subwavelength features embedded in sol-gel pattern on the surface of the silicon device layer. This surface was then etched using reactive-

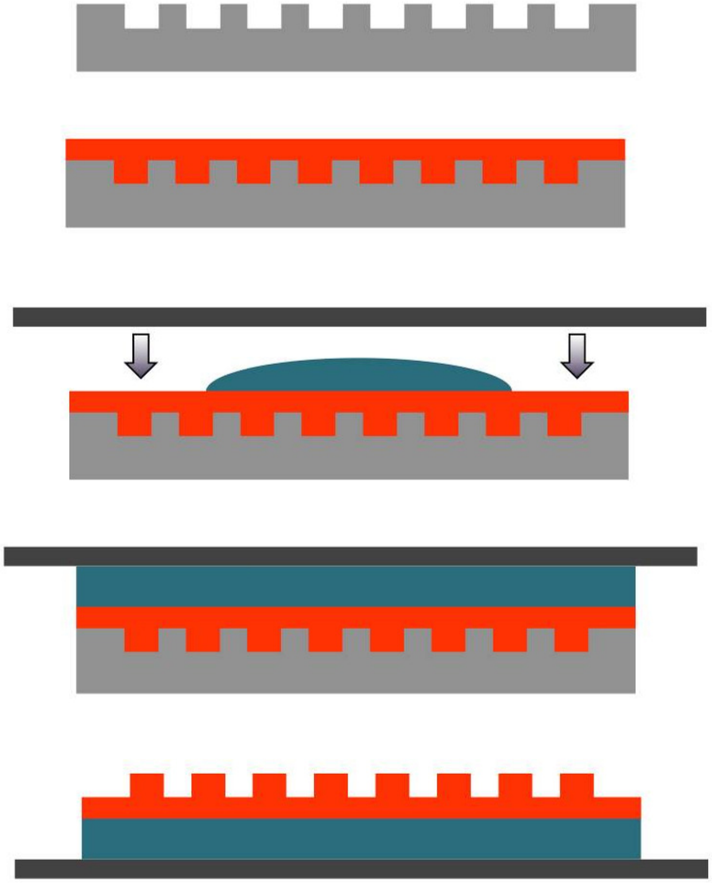

Figure 4.18. Master stamp fabrication: A composite PDMS stamp is molded from a silicon wafer patterned via e-beam lithography and used to emboss a resist-coated substrate. The master stamp can be reused thousands of times.

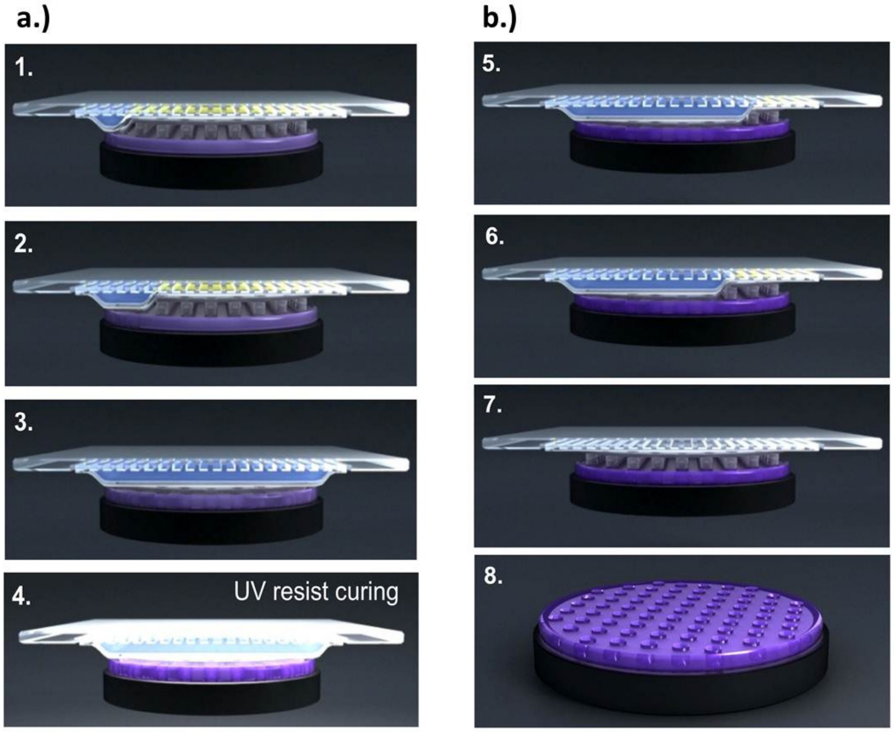

Figure 4.19. Fabrication steps performed in substrate conformal imprint lithography (SCIL): a.) Sequential low pressure imprint cycle and UV resist curing. b.) Sequential stamp release avoids high forces.

ion etching (RIE) to transfer the array pattern into the silicon device layer, and the remaining sol-gel layer is removed with an HF-dip (Figure 4.20).

4.13 Fabricated devices

Several different types of arrays were fabricated via SCIL on 150mm SOI wafers with 220nm silicon device layer thickness at Philips Research (Figure 4.21). To elucidate the role of periodicity in determining light trapping behavior, initial studies focused on regular square arrays with cylindrical geometry. Cylinder diameters ranging from 75nm to 175nm were patterned, and cylinder heights of 75nm were defined with RIE after SCIL patterning. Arrays with both 400nm and 500nm pitches were examined. These various arrays were patterned in 6mm by 6mm squares, and several examples of each pattern were fabricated to account for any non-uniformity across the wafer.

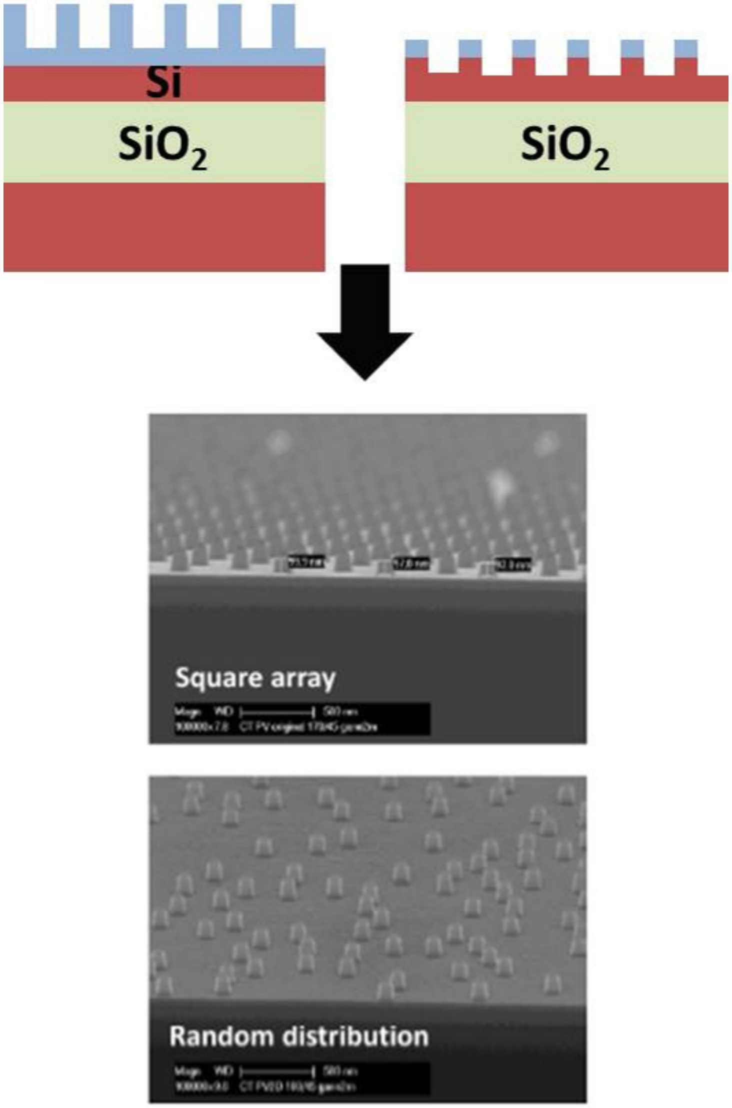

Figure 4.20. Schematic of cross section before and after RIE etch and sol-gel removal. SEM micrographs show representative arrays.

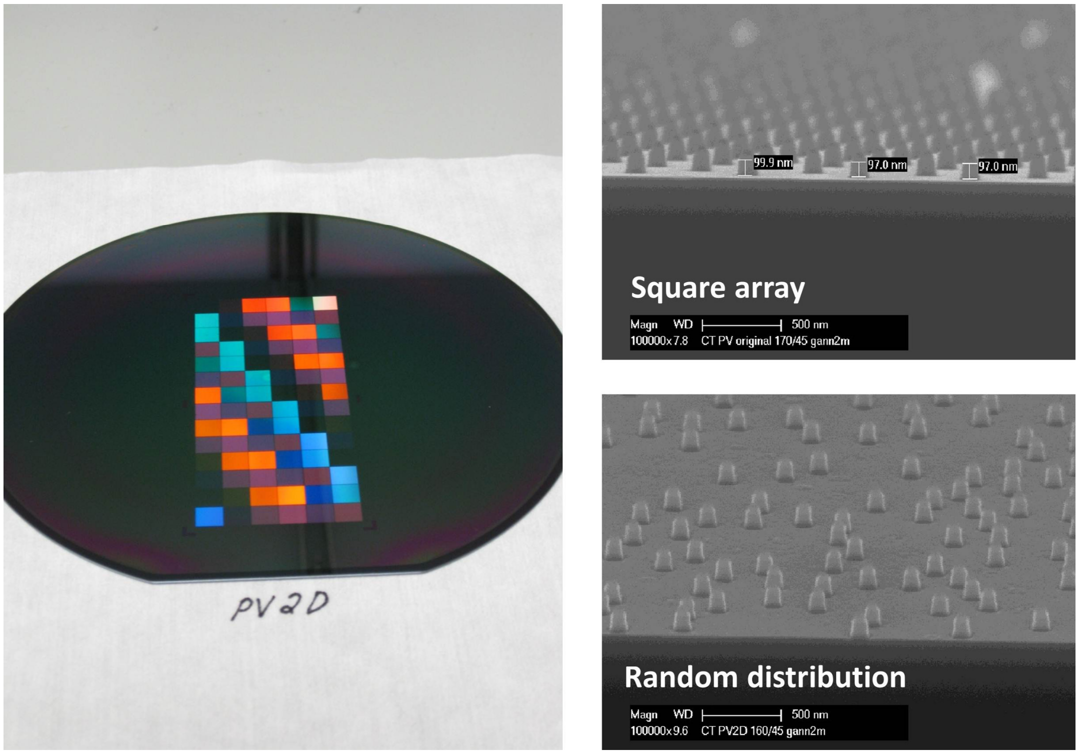

Figure 4.21. Silicon cylinder arrays fabricated on SOI wafer via SCIL. Each color represents a 6mm by 6mm array with varying surface geometry.

To enable electrical measurements, aluminum contacts with a width of 300μm were defined via photolithography and deposited using e-beam evaporation. Each device area was then defined with a mesa etch using 64HNO$_3$:3NH$_4$F:33H$_2$O, with an observed etch rate of 8nm/s. Several different device areas were fabricated to enable comparison between measurements across different areas to ensure consistency between measurements by accounting for the sheet resistance of the patterned silicon film.

4.14 Spectral response measurements

The photoconductivity of fabricated devices was determined by evaluating the change in sheet resistance resulting from illumination. Devices were inserted into a circuit board and mounted on a motorized post that allows the angle of incident light to be systematically varied. A supercontinuum laser was used as the light source to obtain a continuum of wavelengths from λ=400nm to 900nm. Signal-to-noise optimization was obtained through the use of an optical chopper wheel and lock-in amplifier, and a 5V bias was applied across the sample contacts to enable carrier collection. A fraction of the incident light is redirected via a half-mirror to a reference diode, allowing the measurements to be normalized to the input spectral power density. The photoconductivity measurement results are then normalized and compared to the simulated quantum efficiency calculations obtained through FDTD device modeling. Angle-resolved measurements were conducted by controllably tilting the sample through an angle range of 0° to 26°. First examining a regular, periodic array of 400nm pitch cylinders with a 175nm diameter, linearly varying peaks in photoconductivity are observed with angle variation. These peaks are evidence of the Bloch modes attributed to the periodicity of the array, and their location corresponds approximately to the modes predicted by FDTD simulations presented previously (Figure 4.22). However, while these measurements demonstrate distinct modes indicative of the effect of periodicity on light interference and trapping, the spectral location of these modes deviates slightly from those predicted by FDTD simulations. Additionally, the photoconductivity measurements exhibit several additional modes not predicted by simulation. The additional modes and spectral shifting may be a result of the variation in shape between simulated and fabricated structures; actual structures fabricated with SCIL are rounded squares, while the simulated structures are perfect cylinders. To test this assertion, an image obtained from a high-resolution SEM micrograph was imported into the simulation environment, and the resulting optical generation rate was compared with that of a perfectly cylindrical array (Figure 4.23). This plot of the normalized optical generation rate for both the realistic structure recreated from the SEM micrograph and the perfectly cylindrical structures exhibits general overall agreement, but shifts are evident for the peaks that emerge between λ=400nm to 500nm, and λ=700nm to 800nm. In addition, a more prominent peak is observed for the fabricated structure around λ=660nm, and this features corresponds to an additional mode observed at this wavelength in the angularly-resolved plot of the measured photoconductivity. Despite these discrepancies, however, the general behavior of light absorption is consistent between simulation and measurement. Most significantly, the evidence of resonant Bloch modes exhibited by the spectral response measurements confirms the light trapping behavior predicted by FDTD modeling and highlights the sizable influence of periodicity in determining light absorption characteristics from a dielectric array.

4.15 Comparison of Ag vs. Si arrays

The wavelength-dependence of scattering, reflection, and absorption enhancement for silicon thin films with subwavelength surface arrays differs dramatically with the material used for the scattering array. While metal nanoparticles produce a localized surface plasmon that results in significant near-field enhancement of light intensity in the thin film substrate, dielectric materials will not produce this effect. However, parasitic losses and the higher reflectivity that results from metal nanoparticles on the surface of the absorbing layer result in a decrease in light absorption. The scattering cross section, reflectivity, and optical generation rate enhancement of both

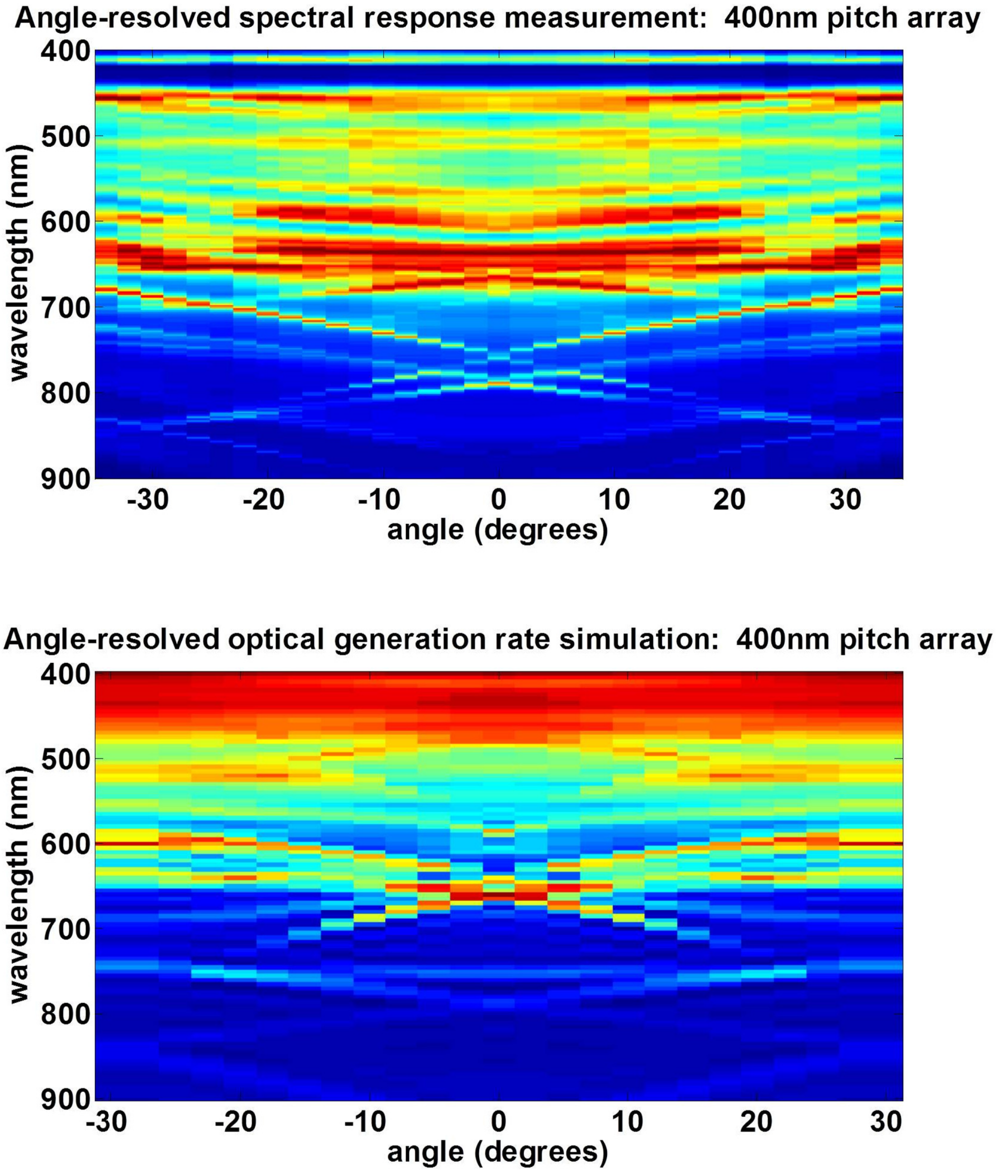
Angle-resolved spectral response measurement: 400nm pitch array

Angle-resolved optical generation rate simulation: 400nm pitch array

Figure 4.22. Comparison of measurement and simulation results for angle-resolved light absorption for a 400nm pitch silicon array.

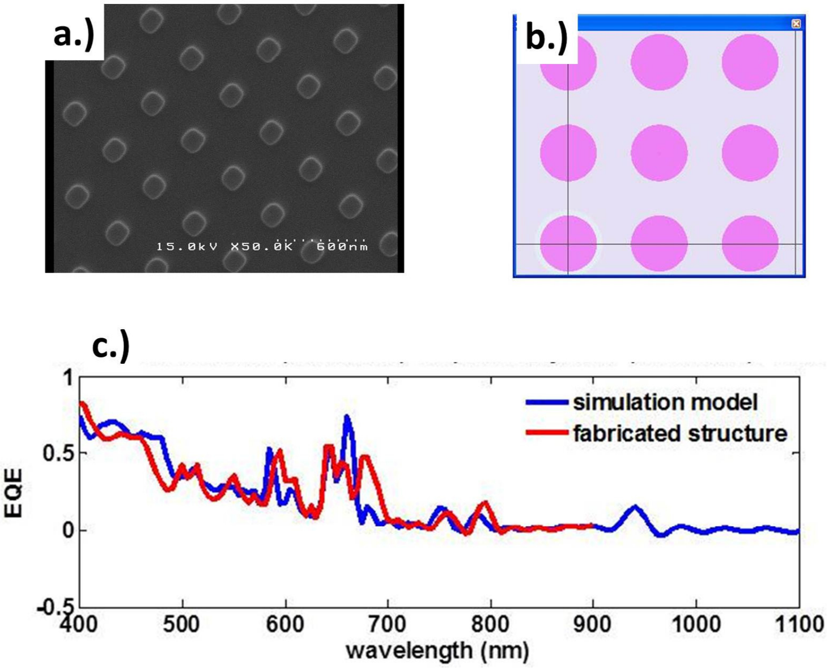

Figure 4.23. a.) SEM micrograph imported for FDTD simulation. b.) Idealized structure used for initial simulation. c.) Comparison of calculated EQE for realistic vs. ideal surface structures.

types of arrays are compared to determine which material offers the greatest potential enhancement in light absorption when used in conjunction with thin-film silicon absorbing layers. For similar geometries, the difference in effective scattering cross section relies on the dependence of the dielectric functions on the polarizability of the material used. Again assuming a point dipole geometry and utilizing the mathematical expressions derived from the Mie approximation, scattering efficiencies of Si and Ag spheres are compared. The enhancement of the effective scattering cross sections for 150nm diameter spheres throughout the spectral range of interest are calculated and presented in Figure 4.24. Prominent peaks in cross sectional area are exhibited for silicon spheres at λ=500nm and λ=620nm, while a general large enhancement exists for silver spheres at short wavelengths; these peaks predict the spectral location of increased scattering into the underlying silicon film and are expected to increase with increasing diameter. To further evaluate the influence of particle diameter on scattering from both of these materials, FDTD simulations were conducted for arrays with a constant 400nm pitch and diameters varying from 50nm to 200nm. The

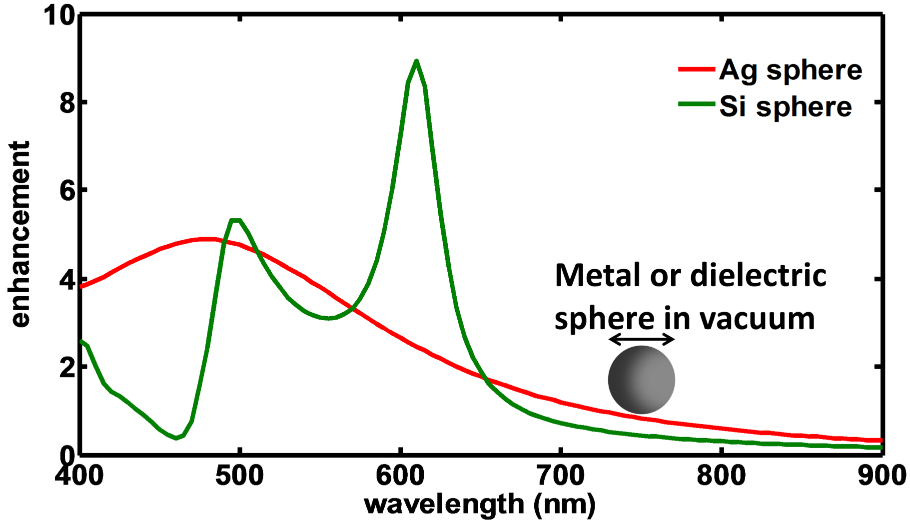

Figure 4.24. Comparison of calculated scattering cross section enhancement for Ag and Si spheres in free space.

enhancement in quantum efficiency was then plotted for all diameters and plotted in Figure 4.25. A general increase in light absorption is observed with increasing diameter for both materials, with wavelength-dependent peaks exhibiting a slight red-shift with increasing diameter. In addition, the Ag array exhibits an area of significant enhancement in the quadrant with the largest wavelength and smallest diameter particles due to the resonant plasmonic nature of these metal nanoparticles. Since a flat silicon film does not efficiently absorb light at longer wavelengths, a large potential for enhancement exists in this portion of the spectrum and is evident in the dramatic increase in quantum efficiency enhancement at longer wavelengths for both types of scattering material. In general, the increase in quantum efficiency enhancement with increasing diameter is indicative of the larger effective scattering cross section, and the peaks around λ=500nm and λ=620nm for a 150nm diameter silicon cylinder array correlate well with the peaks in effective scattering cross section for silicon spheres plotted in Figure 4.24. Despite a slight red-shifting with increasing diameter, the spectral location of resonant enhancement peaks remains relatively constant across the entire diameter, a signature of the presence of Bloch modes that shift only with

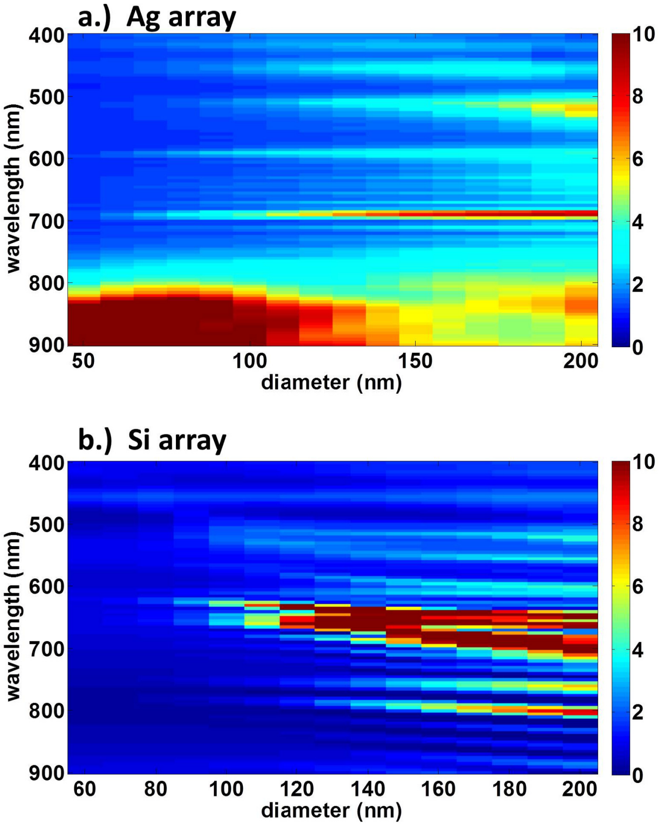

Figure 4.25. Comparison of calculated quantum efficiency with varying diameter for a.) Ag and b.) Si arrays.

pitch. To illustrate the dependence of light trapping characteristics on array periodicity for both metal and dielectric scattering arrays, the quantum efficiency with varying pitch is plotted for both materials in Figure 4.26. While both Ag and Si arrays exhibit linearly varying peaks in quantum efficiency with increasing pitch, Si arrays yield a higher intensity in these resonant modes. Ag arrays, conversely, show more invariance in the spectral location of absorption enhancement with pitch variation, an indication that enhancement from these structures can be attributed more to the diameter of the particles and the existence of resonant modes due to individual particle size and geometry rather than the periodicity of their distribution. In addition, as the pitch of a Si array increases, the intensity of light absorption decreases, while the Ag array exhibits a relative invariance in enhancement amplitude throughout the range of pitches considered in this study. As the diameter of the scattering object increases, more metal coverage from the Ag scattering array is expected to result in an increase in reflectivity from the surface. Consequently, a silicon array is predicted to yield greater enhancement than a silver nanoparticle array at these larger diameters. To test this prediction, the antireflective properties of both metal and dielectric arrays are calculated from FDTD simulation results. These calculations for a 400nm pitch array of 150nm diameter scattering objects are plotted in Figure 4.27. Evidence of Fabry-Perot resonances are evident for both a flat silicon layer and a thin film decorated with an Ag array, while the Si array exhibits a suppression in reflectivity over much of the measured spectral range. The overall integrated reflectivity is significantly reduced with periodic dielectric patterning of the surface, and the results of this study assert that appropriately textured silicon is an effective anti-reflective surface for this device structure.

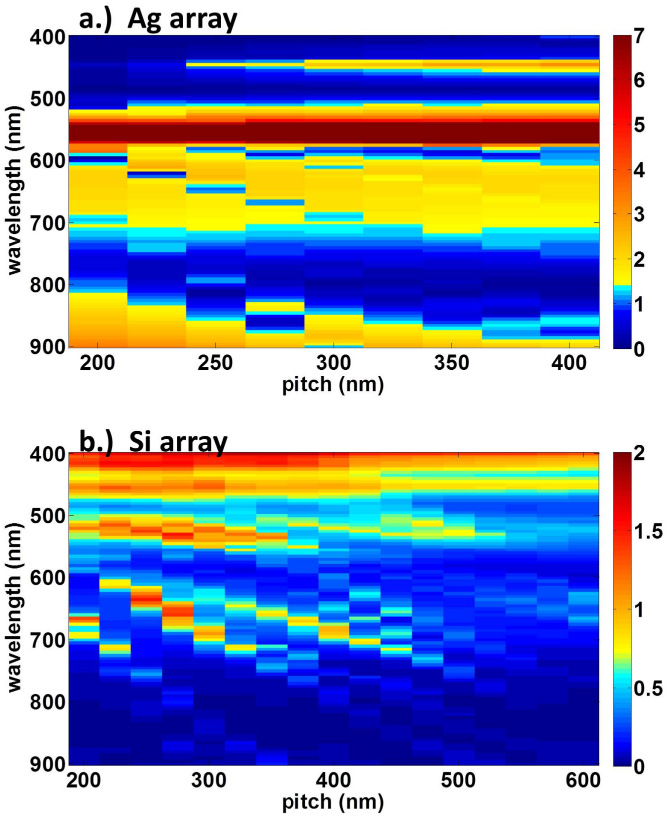

Figure 4.26. Comparison of calculated quantum efficiency with varying pitch for a.) Ag and b.) Si arrays.

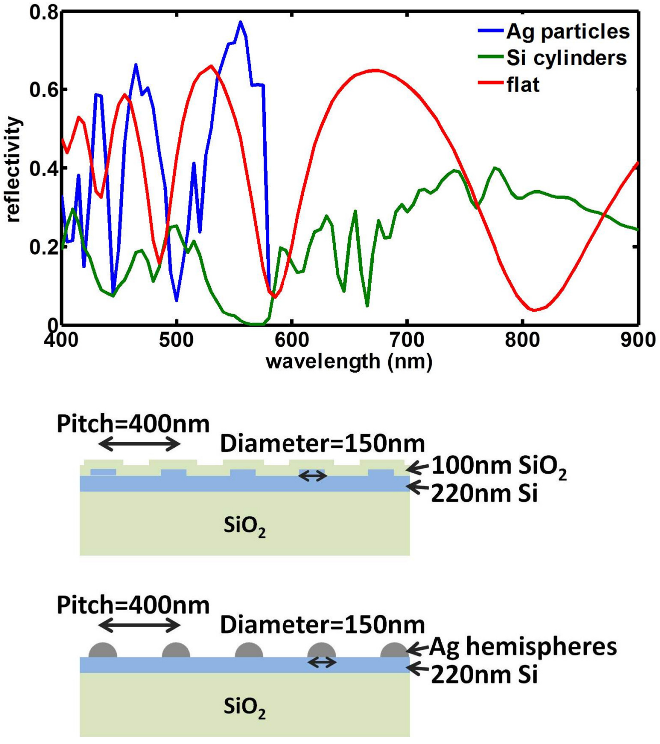

Figure 4.27. Comparison of calculated reflectivity spectra for 400nm pitch arrays of Ag and Si structures on Si substrate.

4.16 Summary of light-trapping characteristics of Si cylinder arrays

Periodic dielectric arrays patterned on silicon films have been evaluated with both simulations and measurements and have exhibited enhanced light absorption across the visible spectrum when compared with flat silicon films without patterning. The periodicity of the arrays produces resonant modes that result in enhanced light absorption in the underlying silicon by constructive interference patterns, and a large potential exists for manipulating the surface geometry to optimize these resonant modes. In addition to these periodic modes, the scattering from these dielectric surface features allows incident light to access waveguiding modes of the silicon film. The combination of both of these effects results in overall enhancement that is optimized for large diameter surface cylinders spaced at either very small or very large pitches, with the maximum overall enhancement for features impinging on one another due to the increased scattering as well as the maximized overall volume of absorbing material. In general, the dielectric arrays exhibit substantially larger enhancement over similar Ag arrays, and this phenomenon is attributed to an increase in reflectivity and parasitic absorption with metal arrays. Practical application of these observations is enabled by recent developments in large-scale nanoimprint lithography, and future work in this area should include large-scale device fabrication and further optimization of antireflective properties of periodic arrays by adding an additional dielectric coating, such as SiN or a-Si. In addition, the potential for using multi-crystalline silicon in this type of geometry should be evaluated and will be highly dependent on the diffusion length of carriers generated in the dielectric surface cylinders.

Chapter 5

Scattering and Light Confinement from Ordered vs. Random Dielectric Arrays

5.1 Manipulation of light absorption enhancement with aperiodic structures

In the previous chapter the resonant modes of a periodic dielectric array and the effect of such arrays on patterns of light confinement in the thin film substrate were examined. The peaks in light absorption enhancement were observed to be highly angle-dependent and span a relatively narrow spectral rang, and an increase in the distribution of these peaks over a higher portion of the solar spectrum is desirable for further optimization of light trapping over the entire spectral range. One means of accomplishing this is by perturbing the periodicity of the dielectric patterning, thus widening the peaks of light absorption enhancement that result from the resonant Bloch modes of the surface geometry. Experimental comparison of random and periodic arrays previously conducted with arrays of metal nanoparticles exhibit this broadening with disorder, but this effect coincides with a significant decrease in enhancement peak intensity [11]. Additional materials and surface geometries have also been studied to determine the light trapping potential for these constructs and confirm the significant angle-dependence observed in this study. Zhou, et al., examined 2-dimensional periodic structures on a-Si:H and demonstrated a theoretical enhancement in photocurrent beyond the Lambertian limit for a restricted wavelength range [39]. Using a 1-dimensional grating structure, Lee, et al., also observed enhancement in light absorption over a narrow wavelength range in the infrared [24]. Sheng, et al., studied the light trapping characteristics of pyramid structures and again observed enhancement in the infrared that is heavily dependent upon the angle of incidence [37]. A perturbation of the periodicity of grating structure is necessary for achieving angle invariance, and an isotropic angular response was achieved experimentally by Ferry, et al., for a-Si:H thin film solar cells with conformal deposited layers over a pseudo-random patterned metal back structure [36]. The issue of random versus periodic structures was addressed also by Lim, et al., in a study of metal nanoparticles on the surface of the absorbing layer, with the observation that random arrays exhibit photocurrent enhancement over a broader wavelength range [11]. Often this observed peak-broadening is accompanied by a decrease in peak intensity, however. The goal of this study is to determine the overall potential for enhancement in light absorption using periodic and aperiodic dielectric structures by evaluating the photocurrent over the entire spectrum of interest, with the goal of developing more general design guidelines for optimizing the light trapping in thin-film silicon solar cells.

5.2 Incremental increase in disorder

To systematically determine the effect of lattice perturbation in these dielectric arrays, an initial array of 9 cylinders is constructed as a base structure for FDTD modeling. The degree of disorder is increased first by perturbing one silicon cylinder, then the cylinders are perturbed by a randomly generated amount between 0 and 50nm. The regular array represents a 400nm pitch arrangement of silicon cylinders of 75nm height and 175nm diameter, and all the following perturbed arrays represent the same cylinder geometry and density over a 3 cylinder by 3 cylinder area. The surface geometry used for FDTD simulations is depicted in Figure 5.1. In this manner the degree of perturbation is increased while maintaining a constant density of scatterering structures on the surface. All arrays are simulated with periodic boundary conditions with the same power monitor locations used previously to determine the absorption and reflectivity in the silicon film.

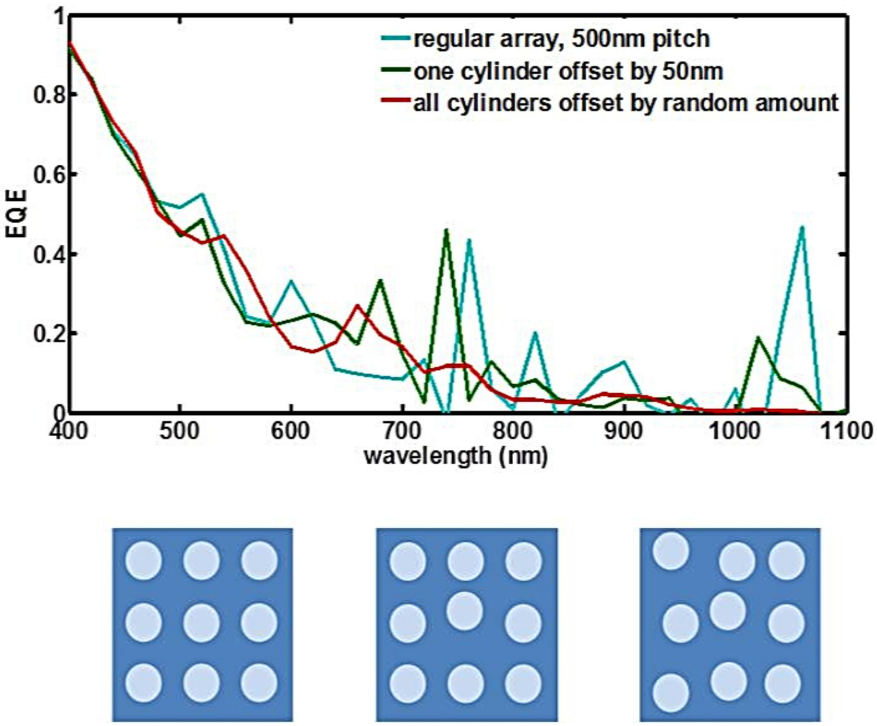

Figure 5.1. Incremental variation of nine-cylinder pattern. Quantum efficiency is calculated from simulation results and demonstrates peak shifting and suppression with increasing degrees of disorder.

Peaks in quantum efficiency characteristic of periodic Bloch modes are evident in the plot for the 500nm pitch array, for example at λ=520nm, 600nm, 760nm, 820nm, 900nm, and 1060nm. When one cylinder is shifted, a decrease and broadening in amplitude is seen for several of the peaks, while a shift in location is seen for others. Namely, a decrease and broadening for the peaks at λ=600nm, 820nm, 900nm, and 1060nm is observed, with a blue-shifting of the resonance peak at λ=760nm. The shift is due to a deviation in the spectral location of the modal resonance, while the decrease and broadening is due to a perturbation of the coupling to these modes. As the disorder is further increased by perturbing all of the cylinders by 50nm, these peaks are further suppressed and broadened. While peak broadening is desirable to access a greater fraction of the spectral range, the accompanying decrease in enhancement peak magnitude detracts from the overall total light absorption, necessitating further evaluation of the total integrated carrier generation with varying degrees of disorder in the arrays of surface features. Therefore an examination of the integrated carrier generation is necessary to determine the relative performance of each of these distributions. To evaluate the overall effectiveness of each of these surface arrays, the net photon absorption is calculated by weighting the quantum efficiency by the AM 1.5 spectrum and integrating over the spectral range to yield a net number of absorbed photons.

5.3 Long-range disorder

To further probe the effect of array distribution on overall light intensity enhancement a pattern with an intermediate level of disorder was simulated and fabricated for measurement. Using a penrose pattern, the effect of long-range disorder in comparison with the short-range disorder of a truly random array can be investigated. A penrose pattern is characterized by a lack of translational symmetry and a long-range correlation length; a simulation area of 2 μm by 2μm is used to ensure a sufficiently large field to avoid significant effects from periodicity resulting from the use of periodic boundary conditions. The array is generated such that the overall density of scatters remains consistent between the arrays being compared, and the results presented here represent the density equivalent of a 500nm pitch array. The quantum efficiency was calculated from these simulation results and is presented with the calculated quantum efficiencies of both a flat 220nm silicon layer and a periodic 500nm pitch array for comparison in Figure 5.2.

While the flat layer and the penrose surface track very closely, some peak shifting is observed (λ=440nm-450nm), a peak emerges for the penrose array around λ=460, and general perturbation due to surface scattering is evident between λ=500nm and λ=600nm. By weighting the quantum efficiency by the AM 1.5 spectrum and integrating, a total number of absorbed photons can be calculated. This total is divided by the net total of incident photons to yield an overall quantum efficiency of 10.35% for a flat silicon layer and 10.55% for the penrose patterned surface. This increase in quantum efficiency with patterning is accompanied by a decrease in overall absorber

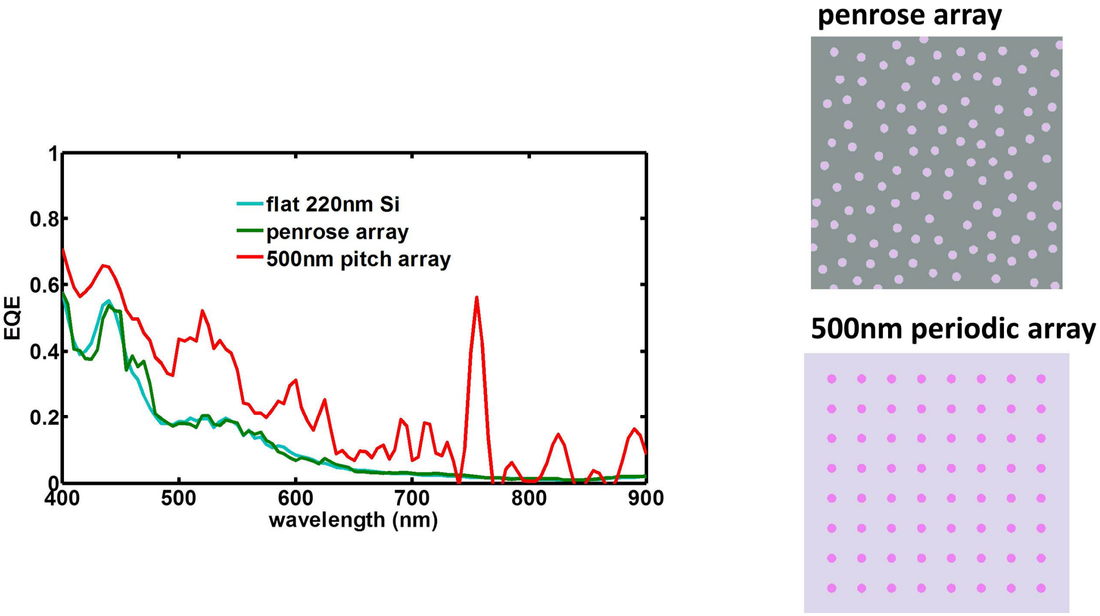

Figure 5.2. Calculated quantum efficiency comparison of long-range disorder (penrose) with periodic dielectric arrays.

volume, highlighting again the significant role of surface geometry in light absorption. Most notable in this plot, however, is the increase in quantum efficiency with a periodic surface array, which results in an overall integrated quantum efficiency of 21.48%, a large increase over both the flat layer and penrose arrays over the majority of the spectral range of interest. This plot exhibits both evidence of periodic modes, indicated by several sharp peaks, and broad enhancement in the short wavelength range, where the increased scattering at these wavelengths works in tandem with coupling to the thin film modes of the structure. The previous chapter demonstrated the dependence of light trapping enhancement on the angle of incident light for a periodic array, as exhibited by distinct Bloch modes. One of the potential advantages of a random array of scattering structures is the expected angle-invariance of light trapping, avoiding a decrease in light absorption at oblique angles and ensuring more consistently performing devices. To evaluate the angle-dependence of light trapping with a penrose array, the quantum efficiency of the penrose array structures was calculated for Θ=0 ° to 25 ° (Figure 5.3). The density of scatterers used in this FDTD simulation is identical to the density used for the calculations presented for periodic arrays, allowing a reasonable comparison between varying degrees of disorder without altering the volume of scattering material. The largest quantity of light absorption is observed at very short wavelengths, and this absorption is relatively angle-invariant (Figure 5.4). These short wavelengths are more sensitive to the scattering cross section of the individual surface structures rather than the periodic modes of the overall array; the density of the scattering structures in this range is a more significant factor in determining light trapping characteristics than the geometry of the array. No distinctive modes are evident as the angle is varied, in contrast to the angle-dependent light absorption for a periodic array (Figure 5.4). In addition, this array geometry shows relative angle-invariance in this range, with less than a 25nm blue shifting in the spectral location of features as the angle increases from 0 ° to 25 °.

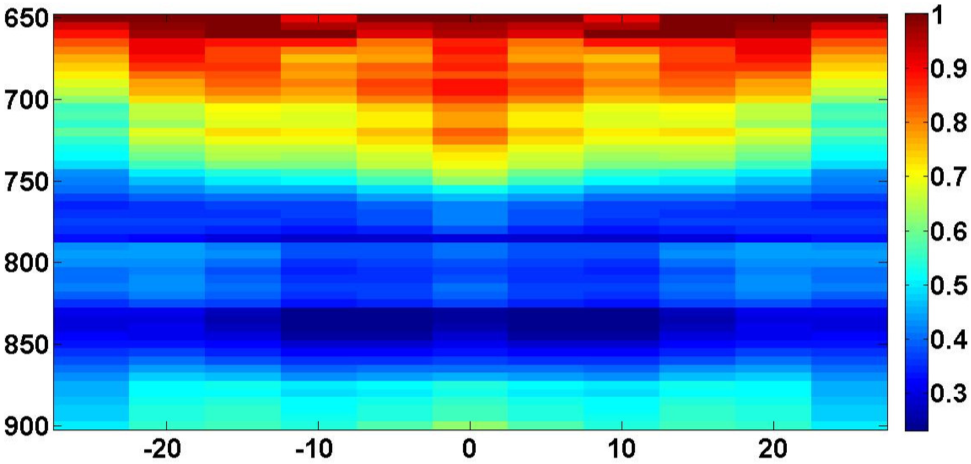

Figure 5.3. Calculated angle-resolved quantum efficiency for penrose array.

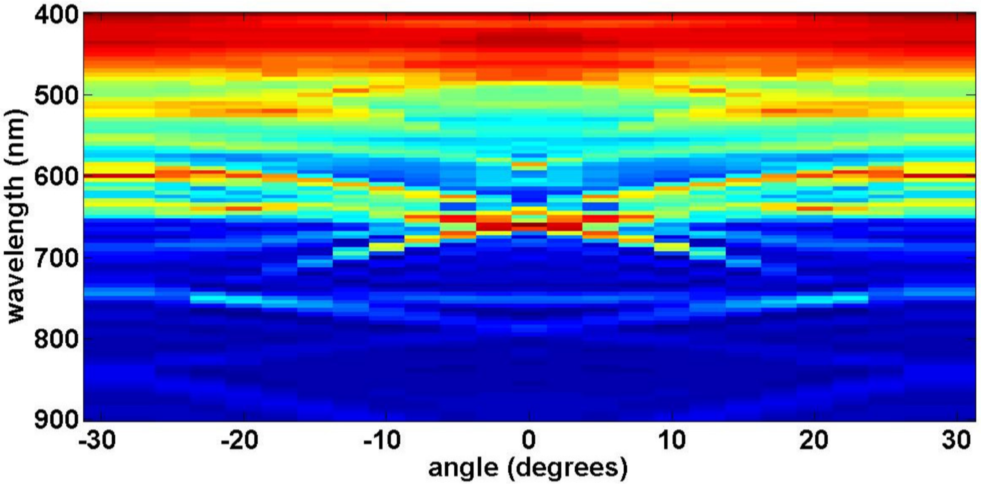

Figure 5.4. Calculated angle-resolved quantum efficiency for periodic array.

5.4 Penrose array: angle-resolved spectral response measurement and simulation comparison

To verify these simulation results, a penrose patterned surface was fabricated via SCIL on an SOI structure for photocurrent measurements using the method outlined in Chapter 4, with the resulting structure illustrated in Figure 5.5, accompanied by that of a regular periodic array in profile. Each of these patterns depicts one 6mm square of the patterned SOI wafer in this image. The calculated reflectivity of both a penrose and a periodic array are depicted in this plot, with significantly lower reflectivity exhibited by a periodic array over the majority of the spectrum. Photocurrent measurements were conducted on the fabricated devices, and Figure 5.6 depicts the results of both spectral response calculations and measurements for a penrose array. Both measurement and simulation results exhibit modulation with changing angle. Since the simulation has a periodicity of 2μm due to the boundary conditions placed

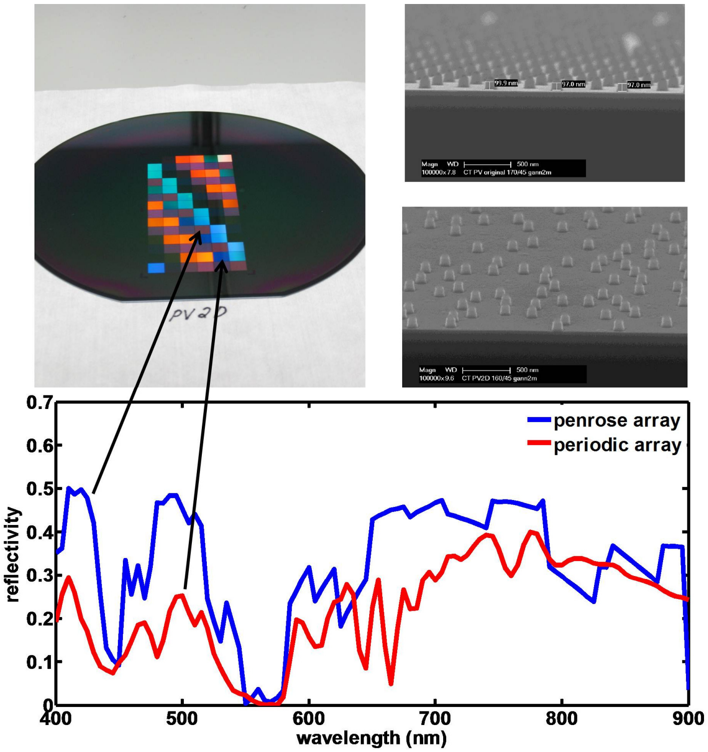

Figure 5.5. Fabricated periodic and penrose arrays on SOI wafer via SCIL.

on the structure model, and the measured penrose array has longer range disorder, these modulation effects are attributed to the influence of feature diameter. Resonant modes and increased effective scattering cross section in an individual structure causes a systematic change in light absorption with changing angle in both measurement and simulation. In addition, both of these plots exhibit enhancement at short wavelengths across all angles, a result of the significant increase in scattering efficiency in this range. The slight suppression seen at short wavelengths in the photocurrent measurement is attributed to inefficient collection of carriers generated in the scattering features due to the increased path length to the device contacts; the quantum efficiency for the simulated structure represents a maximum in that it assumes total collection of generated carriers, and as such does not reflect this suppression in carrier collection. Another inconsistency is observed for normally incident light for long wavelengths (λ>650nm). This could be a result of a decrease in scattering efficiency for the imperfect fabricated structure due to a loss in feature definition, and this effect

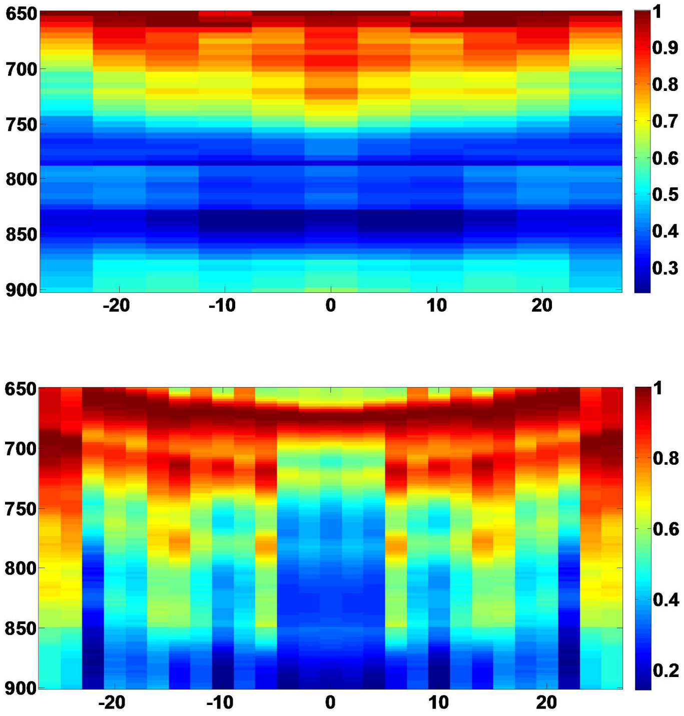

Figure 5.6. Comparison of simulation and measurement of spectral response for penrose array.

would be most significant at longer wavelengths where oblique scattering is required to achieve photon absorption.

5.5 Random dielectric arrays

To test this assumption, an array with a pseudo-random distribution is simulated to determine the effect of the net density of scattering features on light trapping in these structures. In this case any periodic effects will be obscured by a randomly generated distribution and by simulating over a sufficiently large area (2μm by 2μm). The resulting simulation configuration reproduces the same net density of surface features as the simulation areas used for the periodic and penrose structures. The plot of light trapping with randomly distributed structures demonstrates significantly less reliance on incident angle when compared with the penrose array. The same peak in enhancement is observed around λ=450nm over all angles, and this is attributed to the resonant scattering related to the diameter of an individual particle and is therefore angle invariant.

5.6 Random distribution and size

To further highlight the effects of increasing disorder, a randomly generated distribution of silicon cylinders with varying diameters of 75nm, 100nm, and 125nm was simulated and fabricated via SCIL. The calculated reflectivity of this array is compared with that of a flat silicon layer and a periodic array in Figure 5.7. The reflectivity of both the periodic and the random array is less than that of a flat silicon layer over the majority of the spectrum of interest. The periodic array suppresses reflectivity more effectively than a random array between λ=400nm and 550nm but surpasses that of a random array for a range centered around λ=600nm. To determine the net anti-reflection performance of these arrays when implemented in solar cell devices, the

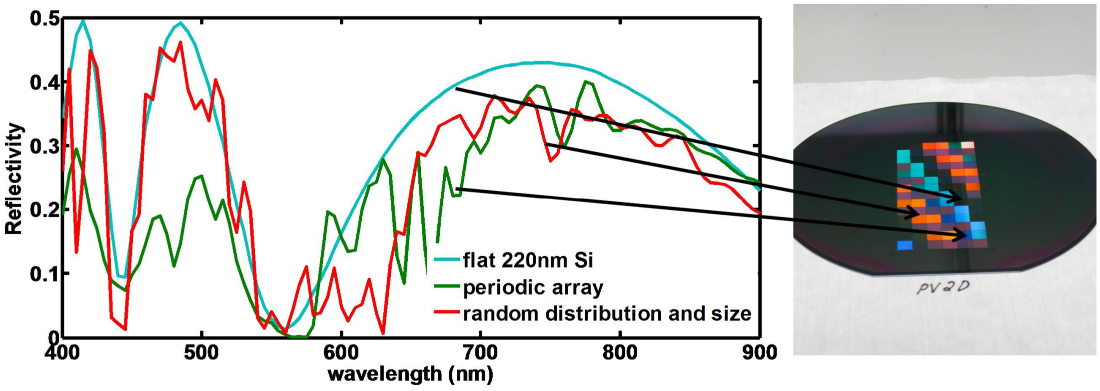

Total integrated reflectivity

flat 220nm Si	**0.3104**
periodic array	**0.2250**
random distribution and size	**0.2482**

Figure 5.7. Reflectivity spectrum for flat 220nm Si, periodic array, and array with random size and distribution.

calculated reflectivity was integrated over the solar spectrum. The resulting calculation yields a net number of photons reflected, which is divided by the total spectrum to give a percentage reflection. The results of this calculation are noted on the reflectivity plot in Figure 5.7. The behavior of this array with an additional degree of disorder is evaluated over a range of angles calculating the quantum efficiency with incident angle. The results of this calculation are presented in Figure 5.8. In contrast to the angle-resolved spectral response of periodic or quasi-periodic arrays, a random distribution exhibits relative angle-invariance across the visible spectrum.

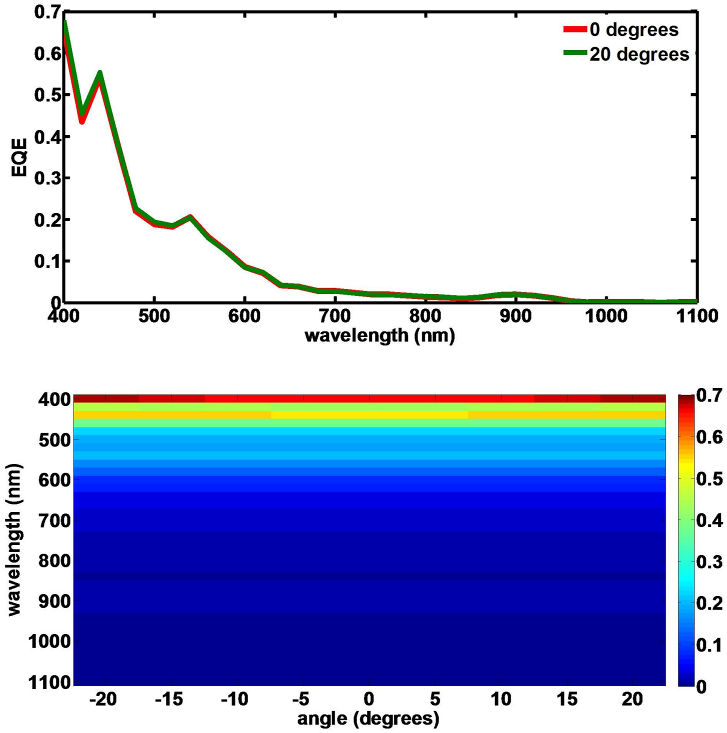

Figure 5.8. Calculated angle-resolved quantum efficiency for array with random size and distribution.

As angle-resolved EQE results demonstrate, the calculated quantum efficiency of this device structure is highly wavelength-dependent. To maximize overall light trapping, the calculations must also account for the spectrum of incident light. The total integrated quantum efficiency was calculated for a range of incident angles by weighting the calculated EQE by the AM 1.5 spectrum and normalizing the result:

$$netEQE = \frac{\int EQE * P_{AM1.5} d\lambda}{\int P_{AM1.5} d\lambda} \tag{5.1}$$

The results of these calculations are plotted in Figure 5.9 for a 400nm pitch periodic array and a penrose array.

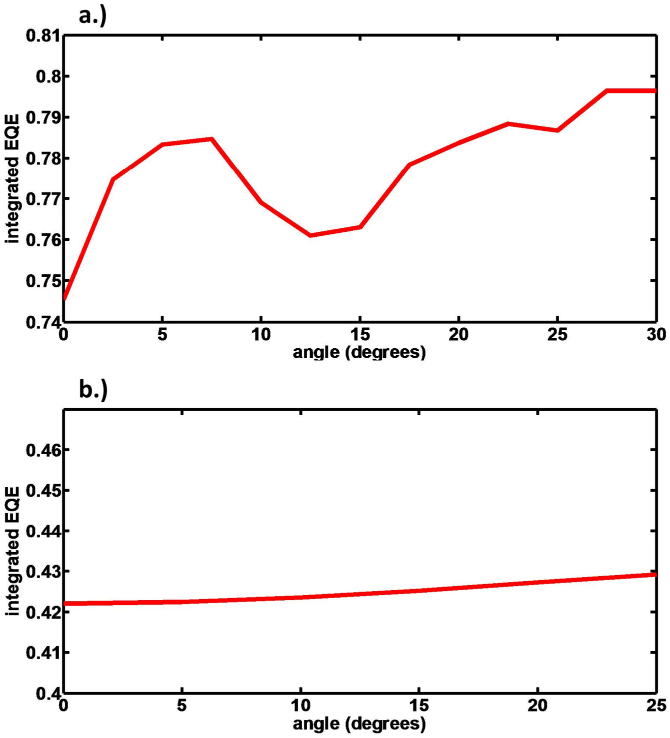

Figure 5.9. Comparison of total integrated EQE with varying angle of incidence for penrose and periodic arrays.

The shape of these plots differs significantly, with the periodic array exhibiting an integrated quantum efficiency that is highly dependent on the angle of incidence, while the penrose array is relatively flat across the range of angles calculated. This demonstrated angle-invariance of the penrose array helps to ensure consistent device behavior through a range of incident light angles, but the total light trapping that results from scattering from this array is significantly less than the light trapping from a periodic array. The overall calculated and integrated EQE is almost twice as large for a periodic array; a periodic array exhibits a quantum efficiency larger than 0.74

throughout the angular range of interest, while the penrose array does not exceed 0.44 quantum efficiency in this same range. Also notable is the overall increase in quantum efficiency for both arrays as the incident angle is increased, indicating that more light is scattered at an angle sufficient for total internal reflection within the silicon thin film. Additionally, the periodic array shows a minimum in integrated EQE around an incident angle of 12 ° while the penrose array shows linear angle dependence. In the previous chapter a similar dependence on pitch was noted for a periodic array, with a clear minimum in quantum efficiency evident for a 325nm pitch array; as the angle of incident light increases the effective pitch of the array will concurrently increase, and the minimum in integrated EQE exhibited here correlates well with the minimum in EQE with pitch previously observed.

5.7 Summary of light-trapping characteristics of pseudo-random arrays

The objective behind increasing the degree of disorder in a scattering array is to increase the overall integrated light absorption across the entire solar spectrum, broadening peaks caused by light trapping from periodic and waveguiding modes of the thin-film structure. Additionally, the performance of these devices is ideally angle-independent to ensure consistent performance. Random arrays have demonstrated these achievements both in simulation and measurement. However, the magnitude of light trapping is severely diminished as a result of this perturbation and dilution of the resonant periodic modes. Calculations that total the net number of photons absorbed over the AM 1.5 spectrum reveal a significantly larger enhancement for regular, periodic dielectric array, with steadily decreasing light absorption concurrent with increasing degrees of disorder. Despite the spectrally narrow enhancement peaks exhibited by periodic arrays, their performance dramatically exceeds that of perturbed arrays when incorporated on the surface of thin-film silicon.

Chapter 6

Conclusions and Future Work

Inexpensive fabrication methods and effective light trapping are requisite for thin-film silicon solar cells to attain cost-competitiveness in the global energy market. To realize highly efficient cells at minimal cost, HWCVD has been examined as a scalable and inexpensive deposition method of fabricating high quality thin-film silicon layers. Highly crystalline films have been grown on soda lime glass substrates by introducing additional hydrogen during growth, despite the absence of an epitaxial template. P-n junctions have been realized at the interface between two HWCVD layers; however, the doping level achieved for n-type films is insufficient for optimal solar device performance, indicating the need for alternative deposition methods for emitter layer fabrication. In addition, crystalline thin-film silicon devices have been fabricated using SOI templates and electrically characterized to determine a realistic optimal performance expected from HWCVD silicon devices. Due to complications with contact formation, accurate characterization of these devices was inhibited, and detailed insight into the photovoltaic properties of these films was not possible. To isolate the optical and electrical properties of the silicon film from the added convolution of device fabrication, FDTD simulations were employed to determine the optimal expected optical characteristics of a thin-film device structure and to examine the potential of surface structures for increasing light absorption in these films. The results of these simulations were used to guide the design of surface arrays.

Various surface structures were examined by modeling SOI structures with 220nm-thick silicon device layers and decorating the surface with nanoparticle arrays of both metal and dielectric material. The goal of these calculations was to gain insight into the potential for scattering structures on the surface of a thin-film silicon solar cell to increase the fraction of incident light redirected laterally into the film, thus increasing path length and absorption. Through examining the scattering cross section, Bloch modes, thin-film waveguiding modes, and plasmonic near-field enhancement resulting from these surface arrays, this study finds significant enhancement in light capturing with these structures.

The reflectivity and quantum efficiency were calculated using electromagnetic modeling results for both Ag and Si nanoparticle arrays. For metal nanoparticles, large enhancement in light intensity in the film is observed even with a close-packed array; this enhancement occurs despite the increase in reflectivity that accompanies an increase in metal coverage and clearly demonstrates the large enhancement in effective cross-section with these particles. This effect is observed primarily for particles with diameters greater than 150nm due to the increased light interaction from a larger effective scattering cross section. A systematic varying of the pitch of regular Ag arrays reveals Bloch modes that shift linearly with pitch size, and these results illustrate the potential for maximizing light absorption by shifting the spectral location of enhancement maxima to higher-power portions of the solar spectrum. The realization of Ag nanoparticles is enabled by a scalable fabrication technique using anodized aluminum oxide membranes as a porous template for through-hole deposition. By adjusting the fabrication parameters, these templates can be produced with a wide range of pitches and particle size to satisfy the optimal device surface geometry. The spectral response of fabricated devices is measured and exhibits a 10-fold increase in carrier generation over devices measured without metal surface arrays.

Since a solar device with metal nanoparticles on the surface is subject to increased losses from reflectivity and parasitic absorption in the metal, dielectric arrays were explored to circumvent these issues and evaluate their potential for producing similar periodic and waveguiding modes in thin-film silicon. Silicon structures on the surface of a thin-film silicon layer were both modeled and measured and show a large enhancement in light absorption when compared with absorption in a flat silicon layer. Structures were fabricated with SCIL, a scalable method of producing arrays with high fidelity, and angle-resolved spectral response measurements show good agreement with simulation results. The pattern of enhancement peaks is attributed to Bloch modes, indicating a significant dependence of the light trapping characteristics on the periodic nature of the dielectric array. The pitch of a dielectric array was optimized for this device structure at 325nm for an array of 150nm diameter cylinders by weighting by the AM 1.5 solar spectrum, a result that is highly dependent upon the thickness of the silicon absorbing layer due the interaction between Fabry-Perot modes, thin-film waveguiding modes, and periodic Bloch modes. Additionally, suppression of reflectivity over both that of a metal array and a flat silicon layer is illustrated by these simulations. Light absorption is also observed to increase with increasing diameter, an effect that is attributed to an increase in overall absorbing volume since carriers generated in the scattering structures of a silicon array may contribute to the overall photocurrent of the device. To examine the potential for aperiodic arrays to broaden absorption peaks, systematically increasing degrees of disorder were introduced to the dielectric arrays. Both spectral response measurements of fabricated structures and FDTD modeling calculations reveal a decrease in light absorption with increasing disorder, reinforcing the conclusion that periodic arrays of dielectric materials have the greatest potential among the surface structures examined in this study for maximizing light trapping in thin-film silicon solar cell devices. These results outline the design parameters necessary for optimizing regular arrays, with the performance shown to be highly dependent upon array pitch for a given absorber thickness. The spectral location of light absorption enhancement is determined by the interaction between periodic scattering modes and thin-film waveguiding modes, and the results presented in these chapters outline a method for optimizing the light absorption spectrum by varying these parameters.

In summary, the incorporation of sub-micron surface structures on thin-film silicon has resulted in a dramatic increase in light absorption due to decreased reflectivity and increased light trapping enabled by the scattering characteristics of these surface structures. While both metal and dielectric arrays demonstrate this result, the use of periodic dielectric cylinders yielded significantly more enhancement in light absorption in the silicon film. Recently developed fabrication techniques provide an opportunity for incorporating these structures on a large scale, and the utilization of such structures on thin-film silicon grown via chemical vapor deposition is a promising method for achieving inexpensive and highly efficient solar cells.

6.1 Future Work

6.1.1 Exploration of parameter space for design optimization

This thesis has demonstrated the existence of an optimal pitch for a given silicon thickness, feature height, and feature diameter. However, the SCIL method allows for full control of device geometry, permitting a much larger parameter space for optimization. Future work with this approach should therefore employ methods of exploring this parameter space. Based on the results presented in this thesis, the pitch of a scattering dielectric array is expected to have a more significant influence on light trapping characteristics than the diameter. However, the resonant Bloch modes may be shifted by the particle size

The significant role of the pitch of a scattering array has been demonstrated with enhancement peaks that systematically vary with varying pitch or angle of incident light. However, a dependence on diameter has also been observed, and the presence of individual resonant modes in each scattering structure is predicted to play a cooperative role with the array geometry in determining the overall light scattering behavior. The resonant behavior of light interaction with a sub-wavelength sphere has previously been studied and described in terms of whispering gallery modes, where the light waves are totally internally reflected and focused by the surface of the sphere [19, 38]. These studies exhibit the potential for tunable light absorption enhancement in a silicon substrate using resonant dielectric surface structures, and this optimization of this effect could greatly increase the potential for increased light trapping. In addition, the description of a periodic array of dielectric scatterers can be described as a two-dimensional photonic crystal (see Chapter 4), and further studies of pitch and scattering geometry could reveal an optimized design for tailoring the photonic band structure, thereby increasing the available photonic states in optimal ranges of the solar spectrum [3, 53]. While this large parameter space illustrates an immense potential for optimization of scattering structures, the exploration of this parameter space presents a computational challenge and will require significant computing power to predict the optical behavior with each of these parameters.

6.1.2 Alternative methods for fabricating planar device-quality thin-film silicon

While the study of dielectric scattering structures presented in this thesis addresses their use on single-crystalline silicon layers, the useful application of this light trapping method lies in its incorporation in cheaply fabricated thin-film silicon layers. We have presented such a method, HWCVD, as a potential technique for depositing device-quality layers. However, this method can result in a pore-permeated structure along with a high degree of surface roughness. While the SCIL method of nanostructure fabrication can be applied to non-planar surfaces, the resonant modes would likely be dramatically suppressed without a sufficiently ordered base surface structure. For this reason future work on the incorporation of dielectric structures on thin-film silicon solar cells should investigate the use of alternative fabrication methods to produce silicon thin films with a more highly planar surface. Previous research has investigated the use of an epitaxial lift-off technique to manufacture thin-film silicon layers [4, 70, 91]. This method induces thermal stress in a bulk silicon structure by applying a material with a different thermal expansion coefficient to the surface of a silicon substrate and subsequently cooling the structure. This thermal stress results in a propagating crack, and by carefully controlling the temperature, this crack can be propagated laterally through the film, resulting in a separated thin layer that can then be removed by the use of a selective wet chemical or vapor etch. The stress-damaged layer of the separated film is then removed, resulting in a silicon film that is fully planar and ideal for patterning with SCIL to produce dielectric surface structures. The remaining silicon substrate can be reused, resulting in very high materials utilization, and the efficacy of this method has been demonstrated on films with surface areas up to 50 cm^2 [4, 70, 91]. By exploiting this epitaxial lift-off method with the SCIL technique, devices that are closely similar to the simulation structures used in this thesis can be fully realized. By further optimization of the scattering array geometry, an enhancement in light trapping efficiency can be expected to exceed those predicted and measured for the specific geometries explored in this thesis, demonstrating the significant potential for carefully structured thin-film silicon photovoltaic devices to offer dramatic increases in light absorption and current generation.

Bibliography

[1] U.S. Energy Information Association. Statistical review of world energy. Technical report, BP, 2011. 1

[2] H.A. Atwater and A. Polman. Plasmonics for improved photovoltaic devices. *Nature Materials*, 9:205–213, 2010. 45

[3] D. Zhou; R. Biswas. Photonic crystal enhanced light-trapping in thin film solar cells. *Journal of Applied Physics*, 103:093102, 2008. 133

[4] K. J. Weber; K. Catchpole; M. Stocks; A. W. Blakers. Lift-off of silicon epitaxial layers for solar cell applications. *Conference Record of the Twenty-Sixth IEEE Photovoltaics Specialists Conference*, pages 107–110, 1997. 133, 134

[5] C.F. Bohren and D.R. Huffman. *Absorption and scattering of light by small particles*. Wiley-Interscience, 1983. 46

[6] P. Campbell. Light trapping in textured solar cells. *Solar Energy Materials*, 21:165–172, 1990. 72

[7] K.R. Catchpole and A. Polman. Plasmonic solar cells. *Optics Express*, 16:21793, 2008. 46, 58, 63, 71

[8] L. Chamness and D. Tracy. Polysilicon manufacturing trends. *Photovoltaics World*, 4, 2011. 4

[9] C.Meehan. Alta devices' new thin-film pv reaching 28.2 percent efficiency. Technical report, CleanEnergyAuthority.com, 2011. 12

[10] C. S. Fuller D. M. Chapin and G. L. Pearson. A new silicon p-n junction photocell for converting solar radiation into electrical power. *Journal of Applied Physics*, 25:676–677, 1954. 9

[11] S.H.Lim; D.Derkas; and E.T.Yu. Light scattering into silicon-on-insulator waveguide modes by random and periodic gold nanodot arrays. *Journal of Applied Physics*, 105:073101, 2009. 115, 116

[12] J. Edwards and F. Keller. Formation of anodic coatings on aluminum. *Journal of the Electrochemical Society*, 79:135, 1941. 49

[13] A. P. Li; et al. Hexagonal pore arrays with a 50-420 nm interpore distance formed by self-organization in anodic alumina. *Journal of Applied Physics*, 84:6023–6026, 1998. 49

[14] B. Lamprecht; G. Schider; et al. Metal nanoparticle gratings: Influence of dipolar particle interaction on the plasmon resonance. *Physical Review Letters*, 84:4721–4724, 2000. 58

[15] B.M.Kayes; H.Nie; et al. 27.6cells under 1-sun illumination. In *37th IEEE Photovoltaic Specialists Conference*, 2011. 12

[16] H. Mahan; et al. Deposition of device quality, low h content amorphous silicon. *Journal of Applied Physics*, 69:6728 – 6730, 1991. 17

[17] Ina T. Martin; et al. Physics and chemistry of hot-wire chemical vapor deposition from silane: Measuring and modeling the silicon epitaxy deposition rate. *Journal of Applied Physics*, 107:054906, 2010. 16

[18] J. Doyle; et al. Production of high quality amorphous silicon films by evaporative silane surface decomposition. *Journal of Applied Physics*, 64:3215–3223, 1988. 19

[19] J. Grandidier; D. M. Callahan; J. N. Munday; et al. Light absorption enhancement in thin-film solar cells using whispering gallery modes in dielectric nanospheres. *Advanced Materials*, 23:1272, 2011. 132

[20] J. J. Mock; et al. Shape effects in plasmon resonance of individual colloidal silver nanoparticles. *Journal of Chemical Physics*, 116:6755–6759, 2002. 46

[21] J. K. Rath; et al. Gas phase conditions for obtaining device quality amorphous silicon at low temperature and high deposition rate. *Materials Research Society Symposium Proceedings*, 1153, 2009. 23

[22] J.K. Holt; et al. Gas phase and surface kinetic processes in polycrystalline silicon hot-wire chemical vapor deposition. *Thin Solid Films*, 395:29–35, 2001. 20

[23] K. Alberi; et al. Epitaxial film silicon solar cells fabricated by hot wire chemical vapor deposition below 750c. *34th IEEE Photovoltaic Specialists Conference*, pages 001355–001357, 2009. 17

[24] Lee Yun-Chih; et al. Enhanced light trapping based on guided mode resonance effect for thin-film silicon solar cells with two filling-factor gratings. *Optics Express*, 16:7969–7975, 2008. 116

[25] M. A. Green; et al. Solar cell efficiency tables. *Progress in Photovoltaics: Research and Applications*, 19:84–92, 2011. 9, 12, 17

[26] M. Weinstein; et al. Pt-h complexes in si:?complementary studies by vibrational and capacitance spectroscopies. *Physical Review B*, 65:0352061, 2001. 19

[27] M.F.Saenger; et al. Infrared ellipsometric characterization of silicon nitride films on textured si photovoltaic cells. *Materials Research Society Symposium Proceedings*, 1123:P02–02, 2009. 74

[28] P. Broguiera; et al. Doping of amorphous and microcrystalline silicon films deposited by hot-wire chemical vapor deposition using phosphine and trimethylboron. *Journal of Vacuum Science Technology*, 15:2968, 1997. 35

[29] P. Matheu; et al. Metal and dielectric nanoparticle scattering for improved optical absorption in photovoltaic devices. *Applied Physics Letters*, 93, 2008. 71

[30] P. Papet; et al. Pyramidal texturing of silicon solar cell with tmah chemical anisotropic etching. *Solar Energy Materials and Solar Cells*, 90:2319–2328, 2006. 75

[31] P. Sinha; et al. Regulatory policy governing cadmium-telluride photovoltaics: A case study contrasting life cycle management with the precautionary principle. *Energy Policy*, 36:381, 2008. 12

[32] R.Morimoto; et al. Low-resistivity phosphorus-doped polycrystalline silicon thin films formed by catalytic chemical vapor deposition and successive rapid thermal annealing. *Japan Journal of Applied Physics*, 41:501–506, 2002. 36

[33] S. Pillai; et al. Surface plasmon enhanced silicon solar cells. *Journal of Applied Physics*, 101:093105, 2007. 48

[34] T. L. Chu; et al. 13.4% efficient thin-film cds/cdte solar cells. *Journal of Applied Physics*, 70:7608–7612, 2009. 12

[35] T. Soederstroem; et al. Flexible micromorph tandem a-si/c-si solar cells. *Journal of Applied Physics*, 107:014507, 2010. 12

[36] Vivian E. Ferry; et al. Light trapping in ultrathin plasmonic solar cells. *Optics Express*, 18:A239, 2010. 116

[37] Xing Sheng; et al. Optimization-based design of surface textures for thin-film si solar cells. *Optics Express*, 19:A841–A850, 2011. 116

[38] Y. N Xia; B. Gates; Y. D. Yin; et al. Monodispersed colloidal spheres: Old materials with new applications. *Advanced Materials*, 12:693–713, 2000. 132

[39] Y. Zhou; et al. Comparison of growth mechanisms of silicon thin films prepared by hwcvd with pecvd. *Thin Solid Films*, 516:564–567, 2008. 15, 115

[40] J. H. Selj; A. Thgersen; S. E. Foss; and E. S. Marstein. Optimization of multilayer porous silicon antireflection coatings for silicon solar cells. *Journal of Applied Physics*, 107:074904, 2008. 75

[41] A. Gallagher. Some physics and chemistry of hot-wire deposition. *Thin Solid Films*, 395:25–28, 2001. 19

[42] J. Gee. Optically enhanced absorption in thin silicon layers using photonic crystals. *29th IEEE Photovoltaics Specialist Conference, New Orleans, LA*, 2002. 84

[43] G.Ehrlich. An atomic view of crystal growth. *Applied Physics A: Materials Science & Processing*, 55:403–410, 1992. 20

[44] BP Solar Global. Statistical review of world energy. Technical report, BP, 2011. 1

[45] O. Jessensky; F. Muller; U. Gosele. Self-organized formation of hexagonal pore arrays in anodic alumina. *Applied Physics Letters*, 72:1173–1175, 1998. 49

[46] M. A. Green. Crystalline and thin-film silicon solar cells: State of the art and future potential. *Solar Energy*, 74:181–192, 2003. 9

[47] T.Minemoto; S. Harada; and H. Takakura. Cu(in,ga)se(2) superstrate-type solar cells with zn(1-x)mg(x)o buffer layers. *Current Applied Physics*, 12:171–173, 2012. 12

[48] Arnim Henglein. Colloidal silver nanoparticles: Photochemical preparation and interaction with o2, ccl4, and some metal ions. *Chemical Materials*, 10:444–450, 1998. 47, 48

[49] H.Matsumura and H. Tachibana. Amorphous silicon produced by a new thermal chemical vapor deposition method using intermediate species sif2. *Applied Physics Letters*, 47:833–835, 1985. 17

[50] F. Keller; M. S. Hunter; and D. L. Robinson . Structural features of oxide coatings on aluminum. *Journal of the Electrochemical Society*, 100:411, 1953. 50, 55

[51] Melbourne Energy Institute. Renewable energy technology cost review. Technical report, University of Melbourne, 2011. 1, 2, 3

[52] iSuppli. Photovoltaic market in north america to surge 200 percent in 2011. Technical report, iSuppli.com, 2011. 2, 3

[53] P. Bermel; C. Luo; L. Zeng; L. C. Kimmerling; J. D. Joannopoulos. Improving thin-film crystalline silicon solar cell efficiencies with photonic crystals. *Optics Express*, 15:16986–17000, 2007. 133

[54] U. Kreibig and M. Vollmer. *Optical Properties of Metal Clusters*. Springer, 1994. 45

[55] P. Kumar and B. Schroeder. Electrical properties/doping efficiency of doped microcrystalline silicon layers prepared by hot-wire chemical vapor deposition. *Thin Solid Films*, 516:580–583, 2008. 35

[56] J. Woo-Seok; J.-W. Lee; and J. Soonil. Evaluation of external quantum efficiency of a 12.35cell comprising dye-sensitized and cigs solar cells. *Solar Energy Materials and Solar Cells*, 95:3419–3423, 2011. 12

[57] S.-Y. Lien and D.-S. Wuu. Simulation and fabrication of heterojunction silicon solar cells from numerical computer and hot-wire cvd. *Thin Solid Films*, 516:765–769, 2008. 25

[58] E.J. Tarbuck Lutgens, K. Frederick. *Essentials of Geology, 7th edition*. Prentice Hall, 2000. 9

[59] A. Mahdjoub. Graded refraction index antireflection coatings based on silicon and titanium oxides. *Semiconductor Physics, Quantum Electronics & Optoelectronics*, 10:60–66, 2007. 75

[60] Stefan A. Maier and Harry A. Atwater. Plasmonics: Localization and guiding of electromagnetic energy in metal/dielectric structures. *Journal of Applied Physics*, 98:011101, 2005. 58

[61] M. Mason. *Synthesis of Large-Grained Polycrystalline Silicon by Hot-Wire Chemical Vapor Deposition for Thin Film Photovoltaic Applications*. PhD thesis, California Institute of Technology, 2004. 20

[62] H. Masuda and K. Fukuda. Ordered metal nanohole arrays made by a two-step replication of honeycomb structures of anodic alumina. *Science*, 268:1466–1468, 1995. 49, 50

[63] H. Masuda and M. Satoh. Fabrication of gold nanodot array using anodic porous alumina as an evaporation mask. *Japan Journal of Applied Physics*, 35:L126–L129, 1996. 49

[64] H. Wiesmann; A.K. Ghosh; T. McMahon; and M. Strongin. a-si: H produced by high-temperature thermal decomposition of silane. *Journal of Applied Physics*, 50:3752–3754, 1979. 17

[65] Gustav Mie. Contributions on the optics of turbid media, particularly colloidal metal solutions. *Annalen Der Physik*, 25:377–445, 1908. 46

[66] M. Fecioru-Morariu P.A. Losio J. Htzel O. Kluth, J. Kalas. The way to 11tandem. In *EUPVSEC*, 2011. 13

[67] J.P. O'Sullivan and G.C. Wood. The morphology and mechanism of formation of porous anodic films on aluminium. *Proceedings of the Royal Society of London*, A317:511, 1970. 49

[68] F. J. Beck; A. Polman; and K. R. Catchpole. Tunable light trapping for solar cells using localized surface plasmons. *Journal of Applied Physics*, 105:114310, 2009. 47

[69] F. J. Beck; E. Verhagen; S. Mokkapati; A. Polman; and K. R. Catchpole. Resonant spp modes supported by discrete metal nanoparticles on high-index substrates. *Optics Express*, 19:146–156, 2011. 45

[70] V. Depauw; Y. Qiu; K. Van Nieuwenhuysen; I. Gordon; J. Poortmans. Epitaxy-free monocrystalline silicon thin film: first steps beyond proof-of-concept solar cells. *Progress in Photovoltaics*, 19:844–850, 2011. 133, 134

[71] Z. Yu; A. Raman; and S. Fan. Fundamental limit of light trapping in grating structures. *Optics Express*, 18:A366–A380, 2010. 72

[72] Solar Market Research and Analysis. Solar energy market growth. Technical report, Solarbuzz.com, 2010. 1, 2

[73] Solar Market Research and Analysis. Technologies. Technical report, solarbuzz.com, 2011. 9

[74] C. E. Richardson. *Low-Temperature Hot-Wire Chemical Vapor Deposition of Epitaxial Films for Large- Grained Polycrystalline Photovoltaic Devices.* PhD thesis, California Institute of Technology, 2006. 21, 23, 36

[75] R. Sheasby, P. G.; Pinner. *The Surface Treatment and Finishing of Aluminum and its Alloys, 6th edition.* ASM International & Finishing Publications, 2001. 49

[76] R. A. Sinton and A. Cuevas. A quasi-steady-state open-circuit voltage method for solar cell characterization. *16th European Photovoltaic Solar Energy Conference*, 2000. 27

[77] First Solar. First solar sets world record for cdte solar pv efficiency. Technical report, http://investor.firstsolar.com, 2011. 12

[78] SolarTechnologies. Solar generation v: Costs and competitiveness. Technical report, solartechnologies.net, 2008. 3

[79] B.J. Soller and D. Hall. Energy transfer at optical frequencies to silicon-on-insulator structures. *Optics Letters*, 26:1421, 2001. 45

[80] H.R. Stuart and D.G. Hall. Island size effects in nanoparticle-enhanced photodetectors. *Applied Physics Letters*, 73:122903, 1998. 47

[81] Z. Su and W. Zhou. Formation mechanism of porous anodic aluminum and titanium oxides. *Advanced Materials*, 20:3663–3667, 2008. 49

[82] L. Zaraska; G. D. Sulka; and M. Jaskula. Anodic alumina membranes with defined pore diameters and thicknesses obtained by adjusting the anodizing duration and pore opening/widening time. *Published Online at Springerlink.com*, 2011. 49

[83] SustainableBusiness.com. Japan delivers breakthrough renewable energy feed-in law. Technical report, sustainablebusiness.com, 2011. 3

[84] K. Nakayama; K. Tanabe; and H. A. Atwater. Plasmonic nanoparticle enhanced light absorption in gaas solar cells. *Applied Physics Letters*, 93:121904, 2008. 12, 49, 50, 51, 52, 55

[85] M. Tao and L. P. Hunt. Crystal growth in silicon chemical vapor deposition from silane. *J. Electrochem. Soc.*, 144:2221–2225, 1997. 20

[86] Marc Verschuuren and Ron Ji. Scil (substrate conformal imprint lithography): A new method for large area nanoimprint lithography. Technical report, MiPlaza: a division of Philips Research, 2007. 99

[87] Vivian E. Ferry; Marc A. Verschuuren; and B.T. Li Hongbo. Improved red-response in thin film a-si:h solar cells with soft-imprinted plasmonic back reflectors. *Applied Physics Letters*, 95:183503, 2009. 12, 46

[88] M. Meier; A. Wokaun; and P. F. Liao. Enhanced fields on rough surfaces: dipolar interactions among particles of sizes exceeding the rayleigh limit. *Journal of the Optical Society of America B*, 2:931–949, 1985. 58

[89] A. Shah; P. Torres; R. Tscharner; N. Wyrsch; and H. Keppner. Photovoltaic technology: the case for thin-film solar cells. *Science*, 285:692–698, 1999. 9, 12

[90] E. Yablonovitch. Photonic band-gap structures. *Journal of the Optical Society of America B*, 10:283–295, 1993. 71

[91] W. Chang; C. P. Kao; G. A. Pike; J. A. Slone; E. Yabonovitch. Vapor phase epitaxial liftoff of gaas and silicon single crystal films. *Solar Energy Materials and Solar Cells*, 58:41, 1999. 133, 134

[92] T. Yang and A.B. Crozier. Surface plasmon coupling in periodic metallic nanoparticle structures: a semi-analytical model. *Optics Express*, 16:13070, 2008. 48

[93] H. Zappe. *Fundamentals of Micro-Optics*. Cambridge University Press, 2010. 90